

IMAGING MASS SPECTROMETRY FOR THE ELUCIDATION OF LIPID AND
PROTEIN CHANGES IN DIABETIC NEPHROPATHY
AND ASSESSMENT OF DRUG EFFICACY

By

Kerri Jaye Grove

Dissertation

Submitted to the Faculty of the
Graduate School of Vanderbilt University
in partial fulfillment of the requirements

for the degree of

DOCTOR OF PHILOSOPHY

in

Chemistry

August, 2014

Nashville, Tennessee

Approved:

Richard M. Caprioli, Ph.D.

David E. Cliffel, Ph.D.

Billy G. Hudson, Ph.D.

John A. McLean, Ph.D.

This work is dedicated to my uncle, whose kidneys shut down after years of diabetes but was lucky enough to receive a new one, and to my dad, who has lived most of his life managing his diabetic condition

ACKNOWLEDGEMENTS

I have many to thank for the support and encouragement that I have received during my Ph.D. research. First of all I would like to thank my advisor, Richard Caprioli, for providing me the opportunity to train in his lab. I truly appreciate his support, encouragement, and excitement for my research along with the freedom and resources he gives to explore ideas and develop as a scientist. Thanks also to my Ph.D. committee, Billy Hudson, John McLean, and David Cliffel, for your guidance and support.

In particular I need to acknowledge Billy Hudson, for the collaboration that became my thesis project. Thank you for your encouragement, guidance, and openness to new paths as my project developed. Your passion for science and people is inspiring. A special thanks to Paul Voziyan, who provided kidney samples and mouse data and was always willing and available to answer questions, give feedback, discuss data and provide an encouraging word. Additional thanks to Ray Harris and his lab for providing the mice used in this study, Suwan Wang for her work with the mice, Paisit Paueksakon for providing the pathology work in Chapter III, and Fenghua Zeng for providing the immunofluorescence in chapter IV. This work would not have been possible without them.

I am also thankful for past and current members of the Mass Spectrometry Research Center. It has been a pleasure to work in such a good environment and with so many colleagues that are great both scientifically and personally. Thanks to the many who have contributed help or insight into my work: Jeff Spraggins, Kristie Rose, Raf Van de Plas, Peggi Angel, Andre Zavalin, Junhai Yang, Erin Seeley, Lisa Manier, Mitch Reyzer, Kevin Schey, Jeremy Norris, and many more. I am especially grateful to Jeff for

taking the time to teach and train me on everything I now know about the FTICR. And of course, I must acknowledge funding support provided by NIH 5P41 GM103391-03.

And finally, I must thank my husband, Peter Frick, for always loving me, supporting me, believing in me and challenging me. You make me a better person.

TABLE OF CONTENTS

	Page
DEDICATION	ii
ACKNOWLEDGEMENTS	iii
LIST OF TABLES	vii
LIST OF FIGURES	viii
TECHNOLOGICAL ABBREVIATIONS.....	xi
BIOLOGICAL ABBREVIATIONS.....	xii
Chapter	
I. INTRODUCTION	1
Overview.....	1
Diabetic Nephropathy	2
MALDI Mass Spectrometry	10
Summary and Research Objectives	20
II. METHODS FOR HIGH SPATIAL RESOLUTION IMAGING AND TARGETING OF MICROSTRUCTURES IN THE KIDNEY WITH MASS SPECTROMETRY	22
Overview.....	22
MALDI IMS as a Tool to Study Kidney Disease.....	22
MALDI IMS Overview.....	23
Fresh Frozen Tissue Preparation.....	27
Matrix Application for Micro-Structure Analysis	30
MALDI MS Instrumental Considerations for Direct Kidney Analysis	42
Data Processing, Image Co-registration, and Image Analysis.....	47
Conclusions.....	49
III. DIABETIC NEPHROPATHY INDUCES ALTERATIONS IN THE GLOMERULAR AND TUBULE LIPID PROFILES.....	51
Overview.....	51
Introduction.....	52
Results.....	53
Renal pathology in the eNOS ^{-/-} C57BLKS db/db mouse model of Type 2 DN.	53

	Composition of mouse renal glomerular and tubular phospho- and glycolipids.....	55
	Glomerular levels of major ganglioside NeuGc-GM3 are increased in DN.....	55
	Levels of long-chain series sulfoglycolipids are increased within renal tubules in DN.....	60
	Major bioactive lysophospholipids are elevated in renal glomeruli in DN.....	68
	Non-enzymatic modification of phosphatidylethanolamine by glucose is increased in the cortex of the DN kidney.....	68
	Discussion.....	77
	Methods.....	81
IV.	HIGH SPATIAL RESOLUTION IMAGING MASS SPECTROMETRY FOR DETECTING SPATIAL DISTRIBUTIONS OF PROTEINS IN HEALTHY, DIABETIC AND DIABETIC TREATED KIDNEYS.....	86
	Overview.....	86
	Introduction.....	87
	Results.....	88
	Histology-directed profiling for protein expression in glomerular lesions.....	88
	High spatial resolution MALDI IMS reveals protein differences in specific regions of DN kidney cortex.....	93
	Identification of peaks from IMS.....	99
	Identification and localization of alpha-1-antitrypsin.....	99
	Albumin fragments in the DN kidney.....	102
	Immunofluorescence staining shows tubular localization of albumin fragments.....	106
	Discussion.....	106
	Methods.....	111
V.	CONCLUSION AND PERSPECTIVES.....	116
	High Spatial Resolution Imaging for Elucidating Markers of Kidney Disease.....	116
	Future Research Directions.....	119
	Conclusions.....	124
	REFERENCES.....	127

LIST OF TABLES

Table	Page
2.1. Matrices and sublimation conditions used for high spatial resolution IMS.	35
3.1. Composition of mouse renal glomerular and tubular lipids determined by direct tissue MALDI MS analysis.....	57
3.2. Relative quantitation of Amadori-PE levels within renal cortex	74
4.1. Table of identified proteins.....	100
4.2. Albumin fragments detected in diabetic kidneys.....	104

LIST OF FIGURES

Figure	Page
1.1. Structure of pyridoxamine (PM).....	5
1.2. Kidney structure.....	7
1.3. Schematic of a mature glomerulus in cross section.....	8
1.4. Schematic of MALDI process.....	12
1.5. TOF schematic.....	13
1.6. FTICR schematic.....	17
2.1. Schematic representation of IMS analysis of kidney sections.....	24
2.2. Schematic representation of histology directed profiling.....	26
2.3. Optical and SEM analysis after MALDI matrix deposition.....	31
2.4. Protein IMS at high spatial resolution.....	33
2.5. Comparison of DAN and DHB as a matrix for kidney lipid analysis.....	36
2.6. 10 μm resolution lipid imaging with DAN.....	37
2.7. 25 μm resolution protein imaging with sublimated/rehydrated CHCA.....	39
2.8 Glomerulus analysis with histology-directed profiling.....	41
2.9. Spatial resolution considerations for IMS of glomeruli.....	44
2.10. Sensitivity increase using CASI.....	46
2.11. Co-registration with histology.....	48
2.12. Workflow of ion image analysis with ImageJ.....	50
3.1. Urinary albumin-to-creatinine ratio (ACR) in diabetic mice and effect of PM treatment.....	54
3.2. Renal injury and effect of PM treatment in kidneys.....	56
3.3. Gangliosides NeuAc-GM3 and NeuGc-GM3 show distinct changes in diabetic glomeruli.....	61

3.4. Gangliosides NeuAc-GM3 and NeuGc-GM3 in different mouse models.....	62
3.5. Structures of sulfoglycolipids.	64
3.6. Levels of long-chain series sulfoglycolipids are increased within diabetic renal tubules.....	65
3.7. Long-chain series sulfoglycolipids in kidneys of different mouse models.....	66
3.8. Tubular localizations patterns of sulfoglycolipids SM3 and SM4s.....	67
3.9. Levels of lysophosphatidic acid (LPA) and lysophosphatidylcholine (LPC) increase in the glomeruli of diabetic kidneys.	69
3.10. Comparison between the levels of LPC and degree of fibrosis within individual renal glomeruli.....	70
3.11. MALDI IMS of lysophosphatidylcholine (LPC) in kidneys of different mouse models.	71
3.12. Analysis of glucose-modified (Amadori) phosphatidylethanolamine (PEs) species in non-diabetic, diabetic, and diabetic + PM mouse kidneys.....	73
3.13. Analysis of glucose-modified (Amadori) phosphatidylethanolamine (PE) species in kidneys of different mouse models	75
3.14. High spatial resolution (10 μ m) MALDI FTICR IMS of glycosylated phosphatidylethanolamines (PEs).....	76
4.1. Identification of fibronectin deposition in individual glomeruli.....	89
4.2. Treatment of eNOS ^{-/-} <i>db/db</i> mice with PM inhibited glomerular fibronectin deposition.....	91
4.3. Increase in glomerular fibronectin deposition in eNOS ^{-/-} <i>db/db</i> mice by MALDI MS and validation by IHC	92
4.4. Average spectra from glomeruli in non-diabetic and diabetic mouse kidneys.....	94
4.5. High spatial resolution IMS shows protein changes in glomeruli of diabetic kidneys	95
4.6 Low molecular weight species increased in diabetic kidney cortex	97
4.7. PCA based differentiation of spectra from IMS	98
4.8. MALDI and ESI analysis of C-terminal fragments of A1AT.....	101

4.9. Localization and relative abundance of A1AT C-terminal fragment	103
4.10. IMS and relative quantitation of albumin fragments	105
4.11. Albumin fragments localize in tubules of diabetic kidney	107
5.1. Glucose modified PE's are increased in the cortex region of the diabetic kidneys	118
5.2. Markers of diseased glomeruli.....	120
5.3. Modified lipids in diabetic livers	122
5.4. Lipid IMS of human kidney section	1223
5.5. Protein IMS of human kidney	126

TECHNOLOGICAL ABBREVIATIONS

9-AA, 9-aminoacridine

ACN, Acetonitrile

CHCA, α -cyano-4-hydroxycinnamic acid

CASI, Continuous accumulation of selected ions

Da, Dalton

DAN, 1,5-Diaminonaphthalene

DHB, 2,5-dihydroxybenzoic acid

ESI, Electrospray ionization

FTICR, Fourier transform ion cyclotron resonance

HPLC, High performance liquid chromatography

IHC, Immunohistochemistry

IMS, Imaging mass spectrometry

LC, Liquid chromatographic

MALDI, Matrix-assisted laser desorption/ionization

MS, Mass spectrometry

MS/MS, Tandem MS

m/z , Mass-to-charge

OCT, Optimum cutting temperature

SA, Sinapinic acid

SEM, Scanning electron microscope

SORI-CID, Sustained off-resonance irradiation collision-induced dissociation

TIC, Total ion current

TOF, Time-of-flight

BIOLOGICAL ABBREVIATIONS

ACEI, Angiotensin-converting enzyme inhibitor

ACR, Albumin-to-creatinine ratio

AGE, Advanced glycation end-product

CST, cerebroside sulfotransferase

DN, Diabetic nephropathy

ECM, Extracellular matrix

ESRD, End stage renal disease

GBM, glomerular basement membrane

GM3, monosialodihexosylganglioside

H&E, Hematoxylin and eosin

LPA, Lysophosphatidic acid

LPC, Lysophosphatidylcholine

LPL, Lysophospholipid

NeuAc, N-acetylneuraminic acid

NeuGc, N-glycolylneuraminic acid

PA, Phosphatidic acid

PAS, Periodic acid Schiff

PC, Phosphatidylcholine

PE, Phosphatidylethanolamine

PG, Phosphatidylglycerol

PI, Phosphatidylinositol

PM, Pyridoxamine

PS, Phosphatidylserine

ROS, Reactive oxygen species

SB1a, gangliotetraosylceramide-bis-sulfate

SM, Sphingomyelin

SM2a, gangliotriosylceramide sulfate

SM3, sulfolactoceramide

SM4s, sulfogalactoceramide

TBM, tubular basement membrane

CHAPTER I

INTRODUCTION

Overview

Diabetes is a growing pandemic both in the United States and around the world. In the last decade the number of cases of diabetes has risen steadily with the current approximation being 26 million people affected in the United States alone.¹ Much of this rise is due to the increase in prevalence of type 2 diabetes. While type 1 and type 2 diabetes have different etiologies, the symptoms and complications of each are similar. Diabetes starts with dysfunction in the pancreas, but it has many systemic effects that contribute to serious health problems. It is the currently leading cause of kidney failure, new cases of blindness, and non-traumatic lower limb amputations. Other major complications of diabetes include heart disease, stroke, hypertension, periodontal disease and nerve damage. The main focus of this work is to study the molecular changes associated with kidney damage due to diabetes.

Approximately one-third of all diabetic patients will develop diabetic nephropathy (DN) and many will go on to develop end stage renal disease (ESRD) requiring continual renal dialysis or kidney transplant.² Much still remains unknown about the pathogenesis of this disease and insight for prevention and better treatment options of DN can lower the incidence of ESRD. This project will investigate the molecular changes that take place in glomeruli and tubules to explore the pathogenic mechanisms of this disease by

use of mass spectrometry. Specifically, matrix assisted laser desorption/ionization (MALDI) imaging mass spectrometry (IMS) will be used to determine the spatial distribution of different molecules within the kidney. The goal of this research project is to develop MALDI MS methods for direct tissue analysis of individual glomeruli and tubules within the kidney cortex by imaging mass spectrometry and histology directed profiling techniques. These methods will then be applied to study an experimental model of diabetic nephropathy. Determining biomolecules that undergo change in disease conditions and evaluating response to treatment may lead to new molecular markers of disease, provide insight into disease pathogenesis, and characterize treatment response.

Diabetic Nephropathy

Diabetic nephropathy (DN) is a major health complication for diabetic patients and is the leading cause of end stage renal disease (ESRD).² Diabetic patients with ESRD are more difficult to manage and experience an increased death rate.¹ The incidence of diabetes has increased rapidly over the past decade and thus the number of cases of DN is rising as well. DN develops in 30 to 40% of type 1 and type 2 diabetic patients. Poor treatment and/or genetic disposition in diabetic individuals lead to increased severity of complications. DN is a progressive disease and is classified into stages: microalbuminuria and macroalbuminuria.³ Pathologic and morphologic changes that are characteristic of late stage diabetic nephropathy include albuminuria, increased glomerular basement membrane thickness, mesangial expansion, focal segmental and early nodular glomerulosclerosis, and markedly decreased glomerular filtration rate. Although there is not a clear understanding of the molecular basis of the pathology of DN, it is known that early detection and maintenance are critical in delaying the progress of the disease.

Molecular Mechanisms of Disease

Diabetic nephropathy is a complex disease that involves many factors. It is characterized by the accumulation of extracellular matrix (ECM) in the glomerular and tubular basement membranes and expansion of the glomerular mesangial matrix decreasing the kidney's function to filter the body's blood. While DN develops in some patients with diabetes, it does not develop in others, even with persistent hyperglycemia. This observation has led to the idea that a subset of patients have an increased susceptibility to DN³ likely based on both genetic and environmental factors. While much remains unknown about the pathogenesis of DN, sustained hyperglycemia and hypertension are important in both initiation and progression of this kidney disease. These metabolic and hemodynamic factors are the main focus of both research and treatment efforts.³⁻⁷ There are several pathways that have been found to contribute to pathogenic mechanisms in diabetic kidney disease. These pathways include increased generation of advanced glycation end products (AGEs), activation of protein kinase C, and increased flux through the hexosamine and polyol pathways.^{5, 8-10} There is cross-talk among these pathways but all have been shown to contribute to ECM accumulation and renal injury. Protein kinase C, hexosamines, and AGEs have been shown to activate transforming growth factor- β (TGF- β) signaling. TGF- β is a major molecule responsible for increased synthesis of collagen type I and IV, fibronectin, laminin and other ECM proteins.^{11 12} AGEs are a group of molecules formed by the non-enzymatic reaction of a sugar with free amino groups on proteins, lipids, and nucleic acids and can form both intracellularly and extracellularly. AGEs are produced in small amounts under normal conditions of aging; however their formation increases under high glucose conditions. In

the extracellular environment, AGEs can accumulate in long-lived ECM proteins which have been shown to alter the ECM composition and effect glomerular cell-matrix interactions and thus may cause cellular dysfunction.¹³⁻¹⁵ All of these pathways have been found to have high glucose and reactive oxygen species (ROS) as common denominators. This has led to the proposition of a unifying mechanism by Brownlee *et al* whereby hyperglycemia induces overproduction of mitochondrial ROS^{8, 16} leading to pathogenesis of diabetic complications.

Diagnosis, Prevention, and Current Treatment Options

The most accurate diagnosis of DN in the clinic is kidney biopsy revealing arteriolar hyalinosis, increased GBM thickness, mesangial expansion, mesangiolysis, focal segmental and early nodular glomerulosclerosis.¹⁷ However, due the invasive nature of biopsy, DN is most often diagnosed with positive proteinuria.³ Currently there is no way to reverse the damage in kidneys of DN patients, and as damage accumulates over time these patients will progress to ESRD. Prevention is the first line of defense. Tightly controlled blood glucose has been found to be the best prevention of DN.

Current treatment options are limited and include tighter control of glucose levels for better maintenance along with drugs to control blood pressure. These therapies will only slow, and not prevent, progression to ESRD. Once kidney damage has begun, maintenance becomes very important. Pharmaceuticals that target the rennin-angiotensin pathway and control renal hemodynamics are currently the only approved drugs for DN¹⁸ as it has been found that in conjunction with blood glucose control, blood pressure control also becomes paramount in maintaining kidney function. Angiotensin-converting

enzyme inhibitors (ACEIs) and angiotensin II receptor blockers (ARBs) are the most commonly prescribed drugs.

A new drug, pyridoxamine (PM) (Figure 1.1), currently in phase II clinical trials, has a different mechanism of action than the currently approved DN drugs by targeting molecules directly involved in the disease mechanism. Prolonged hyperglycemia disrupts many metabolic pathways by production of reactive oxygen species (ROS), reactive carbonyl intermediates, and AGEs. Mechanisms whereby PM protects renal function include inhibition of toxic oxidative and glycoxidative reactions via scavenging of reactive oxygen and carbonyl species and via sequestration of catalytically active transition metal ions.¹⁹⁻²³ A number of preclinical and phase II trials have shown that pyridoxamine preserves kidney function,²⁴⁻²⁸ particularly at the early stages of the disease.²⁹

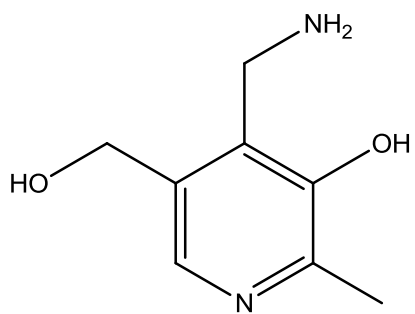
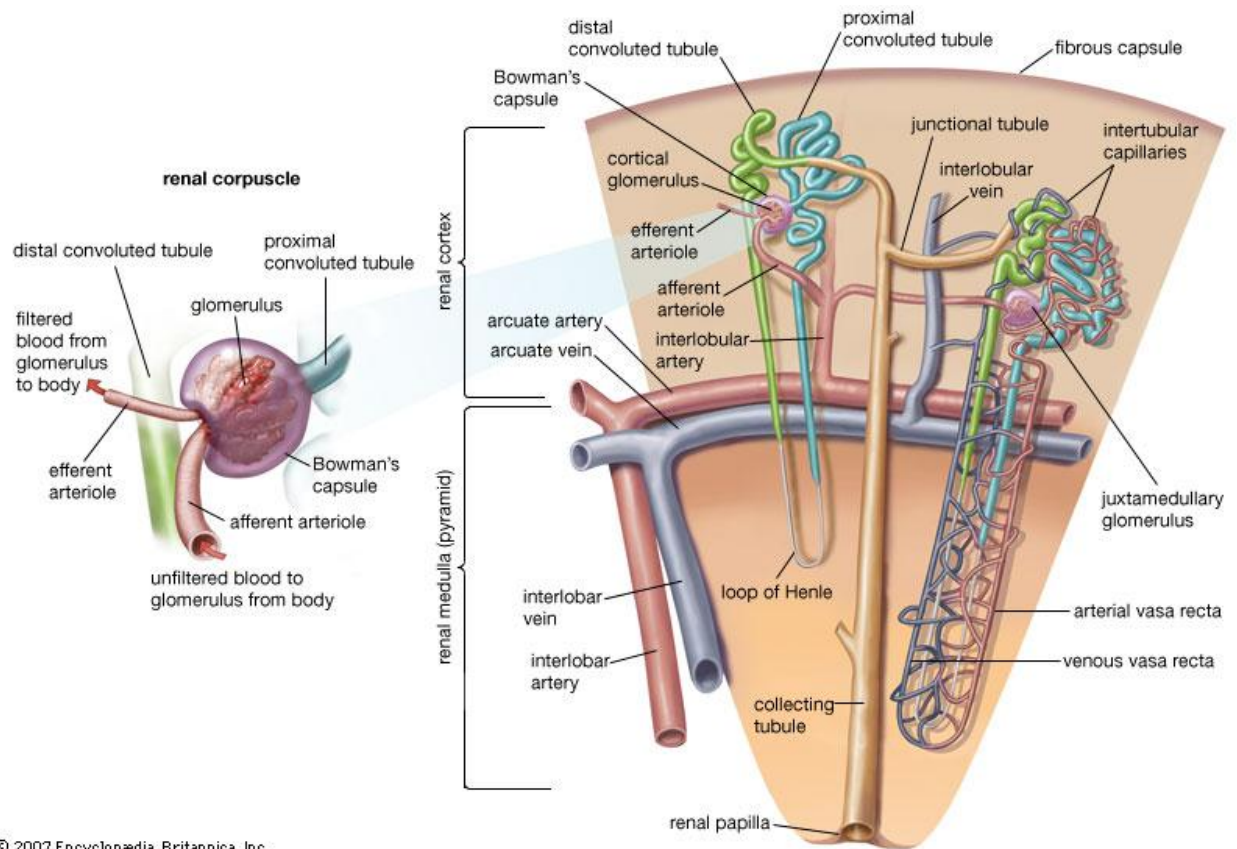


Figure 1.1. Structure of pyridoxamine (PM).

Structure and Function of the Kidney

The kidney's primary function is to remove waste from the bloodstream and to maintain proper electrolyte and fluid balance for the body. Filtration is achieved through the nephron which is the main structural and functional unit of the kidney. Humans have about one million of these functional nephron units per kidney. A single nephron is composed of a glomerulus enclosed by the Bowman's capsule, a proximal tubule, loop of Henle, distal tubule and a collecting duct (Figure 1.2). Filtration begins at the glomerulus which is a small spherical structure consisting of mesangial cells, capillary endothelial cells, podocytes, and extracellular matrix (see Figure 1.3). The glomerular filtration membrane functions as both a size and charge barrier³⁰ where water, small molecules, and small proteins can pass through while large proteins and red blood cells do not pass through the capillary walls. Unfiltered blood enters into the glomerulus through the afferent arteriole and travels through the densely packed capillaries. The water and soluble waste that pass through the fenestrated endothelial cells of the capillaries leaves the glomerulus and continues to the proximal tubule to be excreted as urine. Filtered blood exits the glomerulus through the efferent arteriole to return to the body. About 150 liters of blood are filtered through the glomeruli per day. Most of this fluid is reabsorbed along the tubule concentrating to produce about 1 liter of urine per day. In humans the glomerulus is about 150 μm in diameter and in mice it is approximately 80 μm in diameter. Diseases of the kidney, such as diabetic nephropathy, disrupt the filtering process and reduce the function of the kidney.



© 2007 Encyclopædia Britannica, Inc.

Figure 1.2. Kidney structure. The nephron is the basic structural and functional unit of the kidney. Each nephron of the kidney contains a renal corpuscle and tubule. The corpuscle consists of the glomerulus and the Bowman's capsule and is shown on the left. The tubular portion of the nephron consists of the proximal convoluted tubule, the loop of Henle, and the distal convoluted tubule. As the filtrate flows through the tubule of the nephron, it becomes increasingly concentrated into urine. Waste products are transferred from the blood into the filtrate, while nutrients are absorbed from the filtrate into the blood.

* Reproduced with permission of Encyclopædia Britannica® Online from: renal corpuscle, in *Encyclopædia Britannica Online* [Online] 2014. <http://www.britannica.com/EBchecked/media/107139/Each-nephron-of-the-kidney-contains-blood-vessels-and-a>.

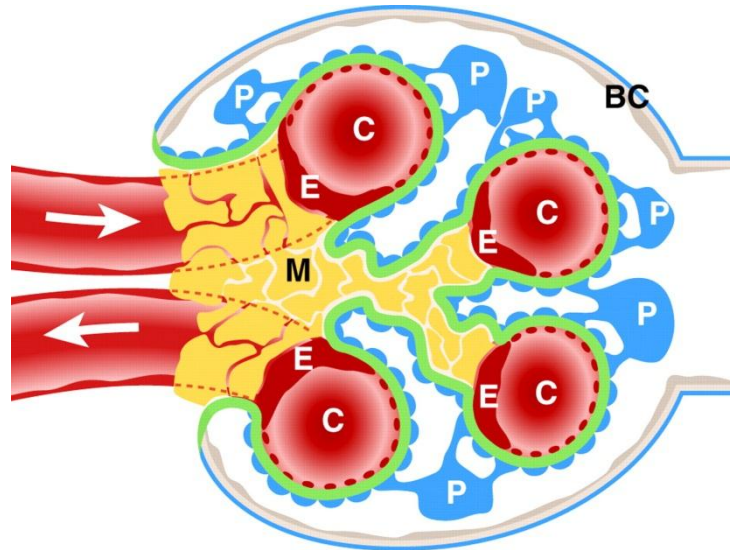


Figure 1.3. Schematic of a mature glomerulus in cross section. Fewer capillary loops are shown than normal for clarity, and the size of cells are exaggerated in proportion to the overall size of the glomerulus. The four major cell types of the glomerulus are the Bowman's capsule (BC) or parietal epithelium (grey), podocytes (P, blue) or visceral epithelium, mesangial cells (M, orange) and endothelial cells (E, red). The mature glomerulus is encompassed by the Bowman's capsule. The glomerulus comprises a self-contained network of capillary loops (C, red), with mesangial cells forming a nexus at the base of the capillary network. The glomerular basement membrane (GBM, green) divides the glomerulus into two compartments, an inner one containing the capillaries and the mesangial cells, and an outer one containing podocytes and the space into which the filtrate passes. The glomerulus remains connected to the remainder of the nephron through an opening in the Bowman's capsule that connects the glomerulus to the proximal tubule, shown on the right. The arrows in the capillaries indicate the flow of blood in and out of the glomerulus. Also omitted for clarity is the branching of the single capillary loop into the multiple loops within each glomerulus.

* Reproduced with permission of COMPANY OF BIOLOGISTS from: Quaggin S E, and Kreidberg J A Development 2008; 135:609-620.

Current Research in DN

Current DN research involves studies using both humans and animal models of the disease. Research with human subjects is usually in the form of clinical trials³¹⁻³³ or cohort studies.³⁴ These often look at end-points in accessible material such as blood or urine. Kidney biopsy is not standard procedure for diagnosis due to its invasiveness. As such, research directly with human renal tissue is less common but include proteomic studies of human glomeruli³⁵ and histopathology studies from biopsies that have established structural and functional relationships between biopsies and clinical manifestations.³⁶

Animal models are important in clinical research. These give investigators more control over the experimental system and allow for more in-depth investigation directly at the site of disease with access to organs. Animal models allow for a variety of experimental designs including controlled studies of experimental therapies, investigations into disease progression, specific molecular pathways or proteins and full scale proteomics studies. Specific to DN, a number of rodent models have been employed.³⁷ In this present study the double mutant $eNOS^{-/-} db/db$ mouse was utilized. The db/db mouse is a common strain used as a Type II diabetes model and has a mutation in the leptin receptor leading to obesity and hyperglycemia. Mice with a mutation targeting endothelial nitric oxide synthase ($eNOS^{-/-}$) have a deficiency in eNOS which leads to hypertension. Crossing these two mouse strains leads to double mutant mice that exhibit hyperglycemia and hypertension and also develop significant albuminuria, basement membrane thickness, mesangial expansion and decreased glomerular filtration

rate. This is the most robust DN model available and closely mimics the human disease.^{38, 39}

Along with this mouse model, a new technology to DN research being utilized in this work is imaging mass spectrometry (IMS). This technology has specific advantages in that it provides native molecular distributions while maintaining the spatial integrity of the tissue, can be interfaced directly with histology, is inherently multiplexed, and suitable for investigations of a wide variety of biomolecules including metabolites, lipids, peptides, and proteins. Additionally, IMS is a good discovery tool as no target specific reagents are required. This is an intriguing application of IMS as much remains unknown about the molecular pathways involved in the pathogenesis of DN.

MALDI Mass Spectrometry

Mass spectrometry (MS) allows for simultaneous detection of multiple analytes without the need for labeling or *a priori* knowledge of the system under investigation. A mass spectrum is a graph of ion intensity plotted as a function of the mass-to-charge (m/z) ratio of ions detected in the gas phase. Two common sources of these gas phase ions are matrix-assisted laser desorption/ionization (MALDI) and electrospray ionization (ESI). MALDI was developed in the 1980's through the pioneering work in the lab of Tanaka⁴⁰ and the lab of Karas and Hillenkamp.^{41, 42} Around this same time John Fenn developed ESI.⁴³ The development of these two soft ionization techniques revolutionized the analysis of large biomolecules. Fenn and Tanaka earned a share of the 2002 Nobel Prize in chemistry for their respective developments of ESI and MALDI. As MALDI MS is the focus of this present work, a brief description of the process and instrumentation used will be described below.

In a typical MALDI experiment, a sample is mixed and co-crystallized with a suitable matrix (Figure 1.4). The matrix is usually a small organic compound that functions to absorb the energy of the laser light and assist in desorption and ionization of a sample. As most commercial MALDI instruments are equipped with UV lasers of nitrogen (337 nm), or solid state frequency tripled Nd:YAG (355 nm) or Nd:YLF (349 nm), matrix compounds that strongly absorb the wavelength of the UV laser are generally required. Common matrices that have been used successfully for a variety of biomolecules include 2,5-dihydroxybenzoic acid (DHB), sinapinic acid (SA) and α -cyano-4-hydroxycinnamic acid (CHCA). The MALDI process generally produces singly charged ions and usually does not induce fragmentation allowing for easy spectral interpretation.

TOF Analyzers

MALDI sources are commonly interfaced with time of flight (TOF) mass analyzers. TOF analyzers determine the mass-to-charge of an ion based on the time it takes an ion to traverse a field free region following acceleration and subsequently hit a detector. These are some of the simplest mass analyzers containing the basic components of an accelerating electrode, a field free drift region, and a detector (Figure 1.5). The detector in TOF instruments is often a multi-channel plate detector. The basis of TOF mass analyzers is that when ions are given the same kinetic energy through acceleration, ions with different masses will have different velocities and therefore will be separated in time. The pulsed nature of a laser provides an inherent ‘start’ time that makes TOF analyzers a perfect match with a MALDI source. When ions are created in the source region after the laser pulse, they are accelerated and enter a field-free drift region where

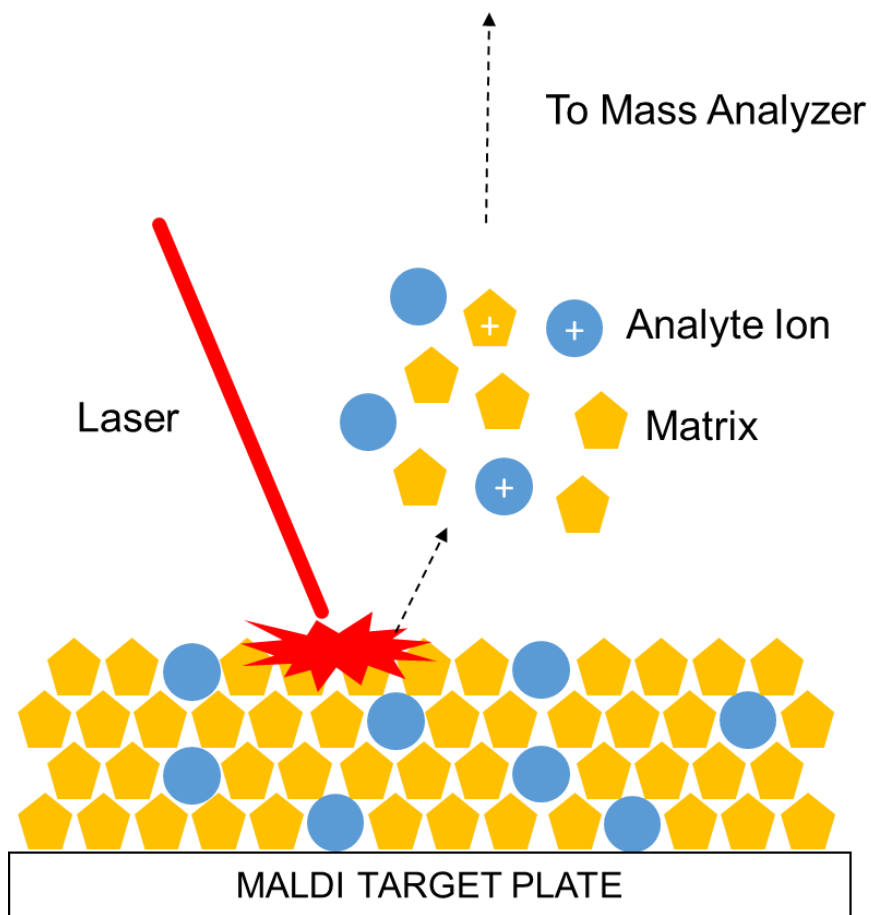


Figure 1.4. Schematic of MALDI process. A laser pulse irradiates a sample-matrix surface. The matrix absorbs the laser energy to assist in desorption and ionization of sample analytes.

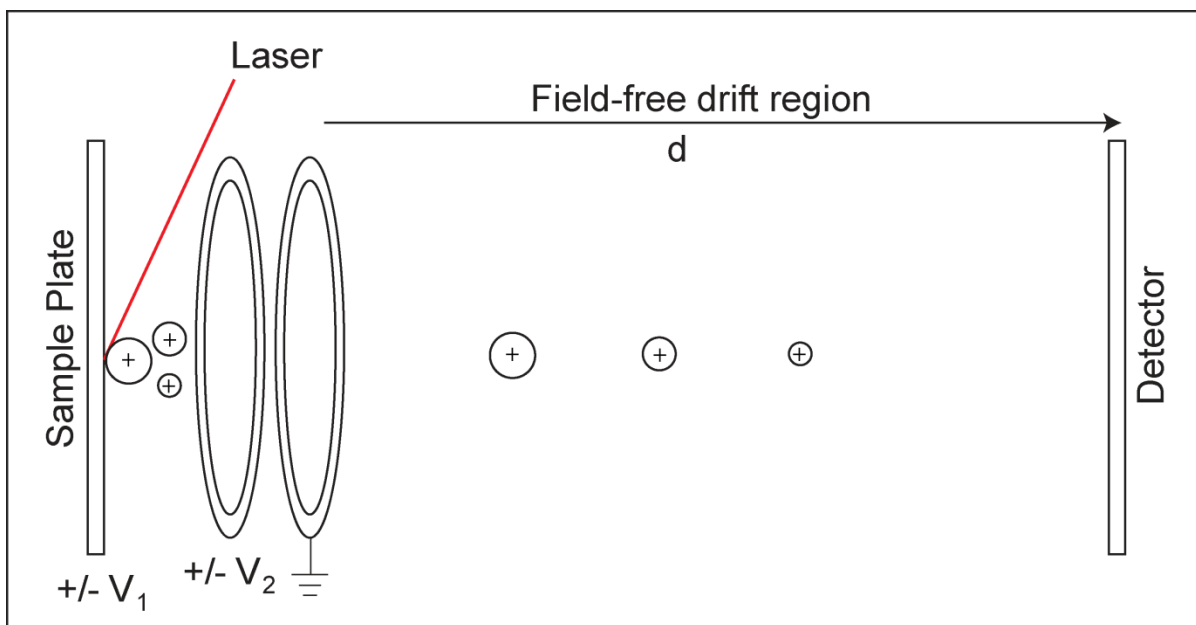


Figure 1.5. TOF schematic. A simplified linear mode MALDI TOF schematic where ions generated from the sample by the laser are accelerated and traverse a field-free drift region of length d and hit a detector. The time of flight is measured and converted to a mass-to-charge ratio (m/z).

they are separated based on their velocity. The kinetic energy of an ion is described by the following equation:

$$KE = zV = \frac{mv^2}{2}$$

where z is the charge of the ion, V is the ion acceleration voltage, m is the mass of the ion, and v is the velocity of the ion. All ions are given the same kinetic energy based on the voltage applied in the source; therefore, the time it takes for an ion to reach the detector is given by the equation:

$$t = d \sqrt{\frac{m}{2zV}}$$

where t is time and d is the distance the ion travels (i.e., the length of the flight tube). Based on the equation above, an ion's mass is proportional to the time that it travels; therefore ions with higher m/z will reach the detector at a later time than smaller m/z ions.

A major limitation of the basic TOF analyzer is mass resolution. Two key instrumental advancements, the reflectron configuration and delayed extraction,^{44, 45} have greatly improved the practical mass resolution achieved with MALDI TOF mass spectrometers. Both the reflectron analyzer and delayed extraction can correct for the broad initial velocity distribution of ions in the plume after a laser pulse. Reflectron instruments use an electrostatic field to reflect the ions toward the detector. Ions with higher initial velocities will penetrate deeper into the field and therefore travel a longer distance than an ion of the same mass-to-charge but a lower initial velocity. This focuses the ions of the same mass-to-charge and allows them to reach the detector at the same time. Reflectron instruments also have a longer flight path further improving resolution. Delayed extraction is used on both linear and reflectron TOF analyzers to improve

resolution. When instruments are operated under constant electric fields, ions of the same mass but different initial velocities will arrive at the detector at different times. The spread of initial velocities can be corrected by pulsing the acceleration field after a given delay, typically one to several hundred nanoseconds. In this manner, ions with higher initial velocities towards the extraction region will be accelerated slower to reach the potential and ions with lower initial velocities will be accelerated faster to reach this same potential. With the correct parameters for delay time and pulsed field strength, ions with different initial velocities but the same mass should arrive at the detector at the same time.

MALDI TOF instruments have a very high duty cycle with some instruments equipped with 5 kHz lasers. This high duty cycle along with the theoretically unlimited mass range of TOF analyzers make these instruments well-matched for bimolecular imaging as they are fast and suitable for detection of a wide range of biomolecules from small molecules to large proteins.

FTICR Mass Analyzers

Fourier transform ion cyclotron resonance (FTICR) mass spectrometers are another type of mass analyzer that can be interfaced with MALDI. Reviews and fundamentals are covered extensively elsewhere⁴⁶⁻⁴⁸ and only the basics will be covered here. FTICR mass spectrometers consist of an ICR cell located in the center of a super-conducting magnet which provides a uniform magnetic field. The basis for FTICR mass analyzers is that ions will undergo cyclotron motion in a magnetic field. This cyclotron motion causes ions to travel in a circular orbit with a frequency that is dependent on its mass. A typical ICR cell consists of three sets of plates: two trapping plates, two excitation plates, and two

detection plates (Figure 1.6). The trapping plates are perpendicular to the magnetic field and after ions are transferred into the ICR cell a small voltage is applied to each end creating a potential well that traps the ions in the cell. Ions typically have very small initial orbits inside the cell. For detection, a radio frequency (RF) potential is applied to the excitation plates. When the RF frequency corresponds to the cyclotron frequency of an ion it will spiral outward with increasing orbit radius (see Figure 1.6). The RF is then turned off and the ion undergoes cyclotron motion with a radius large enough for an image current to be produced at the detection plates. If applied continuously, the ions will spiral outward until they hit one of the plates and are neutralized.

The force on an ion as it enters a magnetic field is described by the following equation:

$$F = zv \times B$$

where B is the strength of the magnetic field and z and v are the charge and velocity of the ion, respectively. This force is called the Lorentz force and causes the ion to have circular motion that is perpendicular to the magnetic field. The centripetal force must equal the magnetic force therefore the following equation is true:

$$F = zvB = \frac{mv^2}{r}$$

Since the distance an ion travels in one rotation is $2\pi r$, the above equation can be rearranged to describe the frequency as:

$$f = \frac{zB}{2\pi m}$$

As seen in the above equation, the ion's cyclotron frequency is only dependent on the strength of the magnetic field and its mass-to-charge ratio and is independent of its

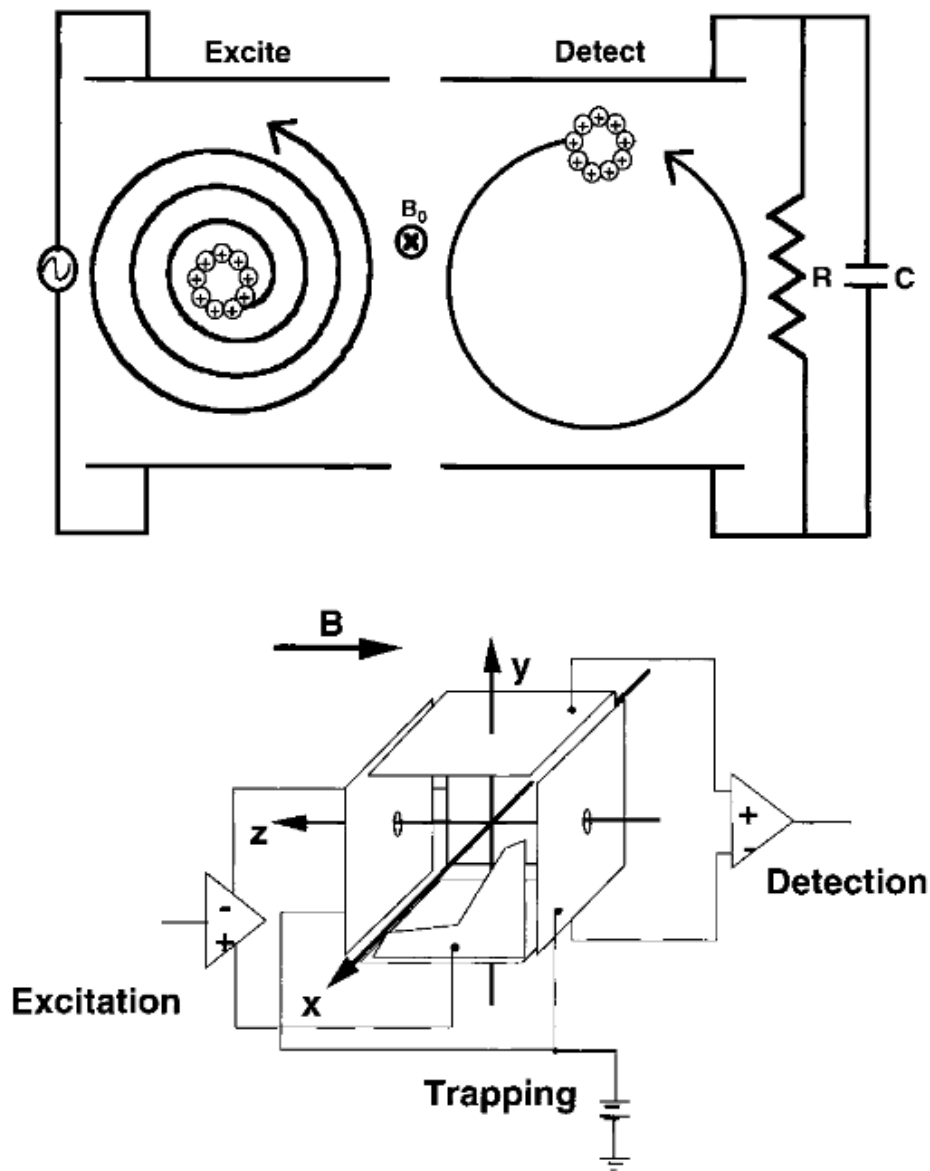


Figure 1.6. FTICR schematic. Incoherent ion cyclotron orbital motion (top left) is converted to coherent (and, therefore, detectable) motion (top right) by the application of a rotating electric field, which rotates in the same sense and at the ICR frequency of the ions of a given m/z value. The electronic circuitry is shown in the bottom diagram.

* Reproduced with permission from: Marshall, A. G.; Hendrickson, C. L.; Jackson, G. S., Fourier transform ion cyclotron resonance mass spectrometry: A primer. *Mass Spectrometry Reviews* **1998**, *17* (1), 1-35.

velocity and kinetic energy. Therefore, constant, homogenous, and unidirectional magnetic fields allow for high mass accuracy and high mass resolving power.

FTICR instruments are the highest performance mass spectrometers available. They achieve both high resolving power (routinely >100,000) and high mass accuracy (sub ppm) lending great value in the analysis of biomolecules. Unlike MALDI TOF instruments where every laser shot results in a detection event, MALDI FTICR instruments can accumulate ions from multiple laser shots before the detection event leading to increased sensitivity for detection of low abundant molecules. However, the detection event is much longer in an FTICR compared to a TOF (typically seconds vs. microseconds) leading to longer analysis times, particularly in an imaging experiment.

Imaging Mass Spectrometry

Combining mass spectrometry with an imaging approach adds yet another layer to the dataset providing the spatial distribution of each detected ion within an analysis area. Current imaging MS technologies include secondary ion mass spectrometry (SIMS), laser desorption ionization (LDI), desorption electrospray ionization (DESI), and MALDI. SIMS is one of the earliest platforms used for imaging and provides the highest spatial resolution by using a focused primary ion beam incident on the surface of a sample. Resolution of 50 nm can be achieved but this technique has a limited mass range of $\sim m/z$ 1000, often producing elemental ions or fragments of surface molecules.^{49, 50} Applications with LDI have reported spatial resolutions of <1 μm but again, has been limited in mass range due to fragmentation of molecules.⁵¹⁻⁵³ MALDI IMS is probably the most widely used MS imaging platform due to the extended mass range and low fragmentation of ionized molecules. Conventional MALDI MS can detect masses that

span several orders of magnitude, extending beyond m/z 300,000. However, the spatial resolution is lower than that of SIMS and LDI imaging where typical MALDI laser spot sizes are 30-200 μm , although spot sizes of 1 μm have been reported.⁵⁴

MALDI IMS is the focus of this work and has been described extensively elsewhere,⁵⁵⁻⁵⁸ but advancements and applications will be briefly outlined here. Since MALDI IMS was first described in 1997 where it was applied to map peptides and proteins in a thin tissue section,⁵⁹ this technology has been used in many other studies to map a wide range of biomolecules including proteins, peptides,⁶⁰ lipids,^{61, 62} pharmaceuticals and metabolites.⁶³ The diversity of molecules suitable for detection with this technology has lent itself to use in a broad range of applications, most notably, in the arenas of biology and medicine. With respect to these areas, MALDI IMS has been instrumental in classifying tumor types in studies including lung, melanoma, and breast cancers,⁶⁴⁻⁶⁶ determining proteomic patterns of specific cell types in autoimmune liver diseases,⁶⁷ determining tissue drug distributions,^{63, 68} and identifying candidate markers of disease.^{69, 70}

The value of MALDI IMS has increased as the technology has developed. Progress in the areas of spatial resolution,⁷¹⁻⁷⁴ sensitivity,^{75, 76} speed,⁷⁷ and sample preparation^{61, 78-81} have opened the doors for this technology to have an impact in ever expanding biological applications. With particular interest for this present work, spatial resolution advancements have been necessary for imaging of small tissue structures such as the glomerulus. Resolution of most reported MALDI imaging experiments is in the range to 30-200 μm . A push to higher resolution has involved development of both the instrument laser technology and sample preparation techniques. One of the major

challenges for achieving high resolution images of biological tissue sections is sample preparation in terms of matrix deposition methods, matrix crystal size, and sensitivity. For example, use of a solvent to aid in the deposition of the MALDI matrix onto a tissue section may contribute to analyte delocalization and formation of crystals $>20\ \mu\text{m}$ limiting the usefulness of a $<10\ \mu\text{m}$ beam.

Summary and Research Objectives

DN leads to progressive decline in renal function and is the leading cause of end-stage renal disease. Much still remains unknown about the pathogenesis of this complex disease. This project investigates the molecular changes that take place in kidney glomeruli and tubules to explore the pathogenic mechanisms of this disease by use of MALDI IMS. The first goal of this research project was to develop MALDI MS methods for direct tissue analysis of glomeruli within a kidney cortex by imaging mass spectrometry and histology directed profiling techniques. The small size of the glomerulus had previously made MALDI IMS of this tissue structure a challenge; however, advances in imaging resolution and sample preparation have made this accessible. These methods have now been applied to study an experimental mouse model ($\text{eNOS}^{-/-}\ \text{db/db}$) of diabetic nephropathy. This is one of the most robust models; mimicking the progressive functional and structural damage documented in human DN. Kidneys from three experimental groups have been studied: wild type (non-diabetic), $\text{eNOS}^{-/-}\ \text{db/db}$ (diabetic), and pyridoxamine (PM) treated $\text{eNOS}^{-/-}\ \text{db/db}$ mice. PM, a promising drug candidate for the treatment of DN and an inhibitor of AGE pathways, has been shown to have a renal protective effect in Phase II clinical trials. In this work, changes in different classes of biomolecules including proteins and lipids have been

investigated with specific signatures found in diseased and healthy kidneys. Determining biomolecules that undergo change in disease conditions and evaluating response to treatment may lead to new molecular markers of disease, provide insight into disease pathogenesis, and characterize treatment response.

The purpose of this work was to achieve the following goals:

Objective 1: Develop methods for direct tissue analysis of kidney micro-structures including the glomerulus and tubules.

Objective 2: Assess the biological significance of *lipid* changes and their spatial distributions in healthy and diabetic kidneys and evaluate the response of lipid signatures in disease after treatment with PM, an inhibitor of oxidative and glycoxidative reactions.

Objective 3: Assess the biological significance of *protein* changes and their spatial distributions in healthy and diabetic kidneys and evaluate the response of protein signatures in disease after treatment with PM.

CHAPTER II

METHODS FOR HIGH SPATIAL RESOLUTION IMAGING AND TARGETING OF MICROSTRUCTURES IN THE KIDNEY WITH MASS SPECTROMETRY

Overview

This chapter will describe the application and use of MALDI IMS with specific considerations and procedures required for kidney analysis. Two common workflows of MALDI IMS will be described: the histology directed workflow and the imaging workflow. These general workflows have been described previously^{56, 66, 82, 83} but presented here are specific considerations for sample preparation and instrumentation for high spatial resolution imaging to target microstructures of the kidney including specific tubular and glomerular structures. In this work high spatial resolution is defined by imaging at ≤ 25 μm . Specific procedures for both lipid and protein analysis will be presented.

MALDI IMS as a Tool to Study Kidney Disease

Innovation and new technology enable advancements in medical and biological research. Despite the significance of glomerular diseases, there is still incomplete understanding of the underlying pathogenic mechanisms. Uncovering molecular events that define mechanisms of susceptibility and progression in glomerular pathology such as

DN will require novel research technologies. MALDI IMS is one such technology that is being utilized in kidney research.

Direct kidney tissue analysis by MALDI MS has been used in previous studies of kidney diseases in both humans and animal models of disease.^{84, 85} MALDI IMS of human kidney biopsies from renal cell carcinoma patients has shown molecular margins between tumor and normal kidney that differ from histological margins.⁸⁶ Groups have used this technology in animal models to study polycystic kidney disease,⁶⁹ glycosphingolipid storage disease,⁸⁷ immunoglobulin A nephropathy,⁸⁸ and drug distribution within a kidney section after dosing.^{68, 70} Specific to the glomerulus, laser capture microdissection has been used to isolate glomeruli from kidney sections and profile pooled glomeruli with MALDI MS in a rat model of focal segmental glomerulosclerosis.⁸⁹ None of these studies however has shown molecular changes at the level of single glomerulus within a kidney section. In this chapter, we demonstrate the use of MALDI IMS to analyze the molecular composition of single glomeruli and tubules within the kidney cortex.

MALDI IMS Overview

MALDI IMS acquires molecular information in a spatially defined manner. There are two general workflows that can be followed in a MALDI IMS experiment: the traditional imaging workflow and the histology directed workflow. Each has utility in analysis of kidney glomeruli and involves careful tissue preparation and matrix application steps before analysis in the mass spectrometer. Each aspect will be described in more detail later in this chapter but the general steps of the two workflows are as follows. In *the imaging mode* (Figure 2.1), a chemical matrix to aid in the absorption of

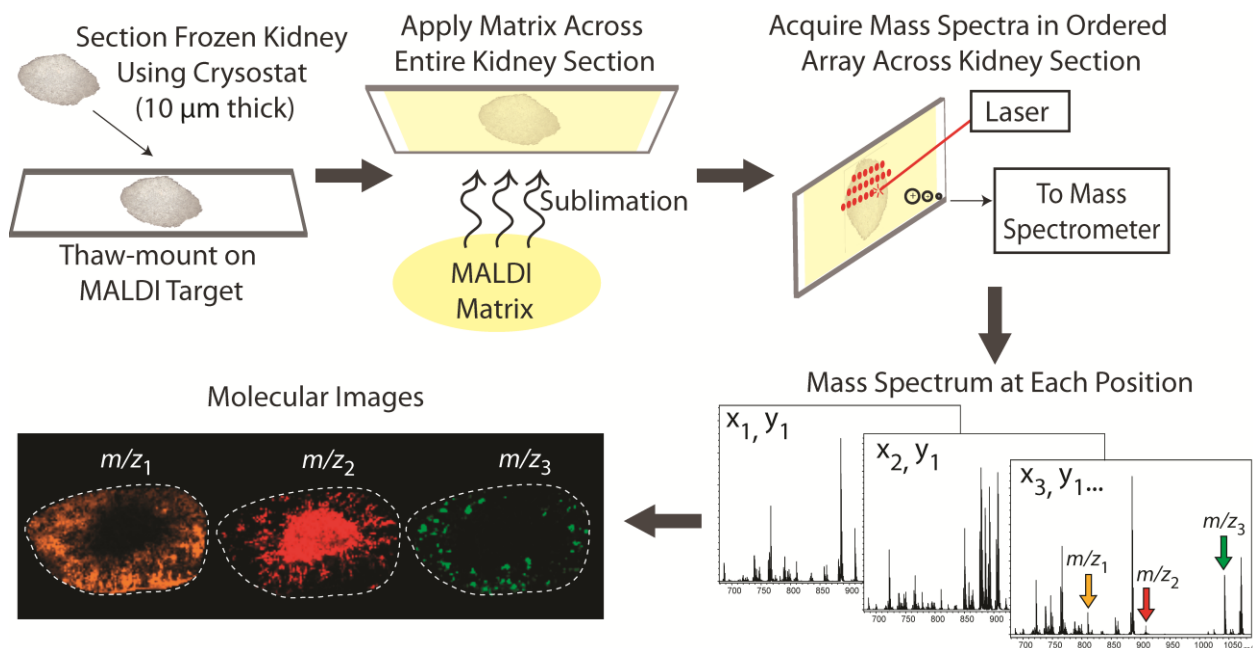


Figure 2.1. Schematic representation of IMS analysis of kidney sections. Frozen kidneys are cryo-sectioned at 10 μm and thaw-mounted on a glass slide. A thin coating of the MALDI matrix is applied across the entire tissue section by sublimation. An ordered array is set up across the kidney section and the MALDI laser is directed at each pixel to acquire a mass spectrum at every point. Molecular images are then constructed by selecting m/z values in the spectra to determine where different molecules are localized throughout the kidney section. Artificial color scale is used to indicate differences in signal intensity for each m/z value.

laser energy is applied uniformly over the sample. The laser is moved in a raster pattern and a spectrum is collected at every pixel in an ordered array across the tissue. Data can then be displayed as molecular maps of the spatial localization of given m/z values throughout the tissue. If required, molecular identification can be performed directly on the tissue section by MS/MS analysis. In *the histology-directed mode* (Figure 2.2), classical histology guides the analysis of specific regions of the tissue. First, a chemical matrix is applied in the discrete areas of interest within the tissue section. A laser beam is used to irradiate the matrix and ionize tissue molecules. As the result, the mass-to-charge ratio of each detected molecule is assigned to a corresponding spatial location within the tissue section. Each workflow requires the basic steps of tissue sectioning, matrix application and mass spectrometry analysis.

As with any methodology, MALDI IMS also has specific limitations. Analysis comes directly from a tissue section where a high concentration of salts and major plasma proteins may interfere with detection of other molecules of interest. Tissue washing can often be successfully used to reduce this interference.^{75, 90} Also, with MALDI IMS there are no upstream separation steps which could help increase the depth of coverage. Other MS techniques such as ion mobility MS or LC/MS can be used in conjunction with IMS to address these shortcomings. It is important to note that up-stream pre-separation procedures may also introduce artifacts thus complicating sample analysis. Further, MALDI IMS involves the addition of a chemical matrix to the tissue section. The choice of MALDI matrix influences what is detected, with certain matrices favoring certain

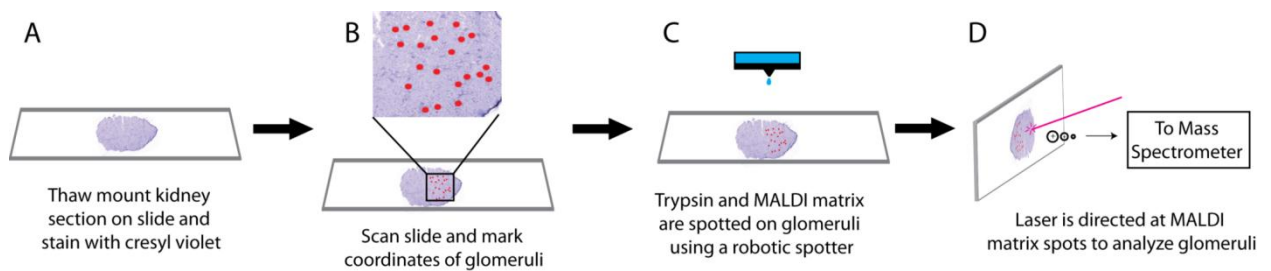


Figure 2.2. Schematic representation of histology directed profiling. (A) A fresh frozen kidney is cryo-sectioned at 10 μm and thaw-mounted on an ITO glass slide. The kidney section is stained with cresyl violet (a MALDI MS compatible stain) for visualization of the glomeruli. (B) Position of glomeruli is determined using MIRAX Viewer, indicated by red dots. The coordinates are exported to the robotic spotter. (C) The robotic spotter deposits trypsin at selected glomeruli for *in situ* digestion followed by the MALDI matrix at the same locations. (D) The sample is inserted in to the mass spectrometer and the laser fires at the matrix covered glomeruli producing ions from individual glomeruli.

classes of molecules. On the other hand, careful matrix choice or use of different matrices in parallel sample analyses can enhance detection of analytes of interest.

Given the limitations, there are also many advantages with this technology. MALDI IMS involves minimal tissue processing, and there is little dilution effect, when compared with other proteomic technologies such as laser capture microdissection or whole tissue homogenization followed by LC/MS. Unlike immunohistochemical analysis, the knowledge of protein identities prior to the analysis is not required, there is no need for any target-specific reagents, and there are no issues with hidden epitopes for antibody binding. In a single experiment, potentially hundreds of molecules can be analyzed from spatially discrete regions of a single tissue section, making MALDI IMS technology an invaluable discovery tool.

There are many aspects to consider in a MALDI imaging experiment including tissue preparation, matrix application, image size and resolution, instrumentation and data analysis. The following will discuss each of these aspects.

Fresh Frozen Tissue Preparation

Sample collection, freezing, and sectioning

MALDI IMS can be applied to fresh frozen tissue as well as FFPE tissue. Use of fresh frozen tissue allows for robust analysis of a variety of molecules including drugs, metabolites, lipids, and proteins. However, FFPE tissue comprises a large portion of what is stored in tissue banks which can be a valuable source of samples. As such, methods have been developed for MALDI IMS of FFPE tissue^{64, 91} but studies are generally limited to enzymatically digested peptides. Fresh frozen tissue was used for all analyses in this study and will be the focus of the methods described in this chapter.

At the time of procurement, organs should be removed and immediately flash frozen in liquid nitrogen to limit degradation of tissue molecules. When doing animal studies, this can and should be controlled; however for samples such as human biopsy or tissue resection the researcher may not be able to control the procurement conditions as tightly. It is best to freeze organs in a way that will best maintain the original shape. This can be done by placing the organ on aluminum foil shaped as a boat and slowly lowering it into the liquid nitrogen. The tissue should completely freeze in a few minutes and can then be transferred to a -80°C freezer for storage. Organs stored at -80°C can be preserved for analysis for several years with minimal degradation.

Tissues stored at -80°C are warmed to -20°C for sectioning on a cryostat. Frozen tissues are usually sectioned between 8 and 20 μm thickness. After a section is cut it should be manipulated carefully with a fine brush, positioned onto a cooled MALDI target, and then thaw mounted to adhere to the target by placing a warm thumb or finger under the target where the tissue was placed. The MALDI TOF instruments used in this study require target plate conductivity. Gold coated metal targets and indium tin oxide (ITO)-coated microscope glass slides are two common conductive surfaces used. Metal targets are often used as a sample substrate because of their high conductivity. When these are used, a section serial to the analysis section is cut and mounted on a glass slide for histological staining allowing for co-registration of histological features with the molecular signals detected. However, for small histological features such as the 80 μm glomeruli in the mouse kidney, it is difficult to track the same structures in a serial section and it is best to use the same section for mass spectrometry analysis and

histological staining. For this reason, conductive ITO slides were used for all applications in this work.

Tissue washing

It is often advantageous to wash a tissue section before matrix application and analysis. Many tissues, and kidneys in particular, contain many salts that can contribute to signal suppression with MALDI MS. The washing procedure is, of course, dependent on the molecules of interest that are to be analyzed. The two major classes of molecules studied in this work are proteins and lipids and each requires a unique tissue preparation. Procedures that have been found to work well for kidney analysis of both lipids and proteins are described below.

Lipids are abundant molecules on the tissue surface. In many cases, no additional washing steps are required and the matrix can be applied directly after sectioning for MALDI MS analysis. Recent work by Angel *et al.*⁷⁶ has shown that using an aqueous wash with a volatile buffer can enhance the sensitivity of lipids detected from the tissue surface, in part by removing salts and reducing matrix clusters. Based on this report, an ammonium formate wash was found useful for the lipid experiments conducted for kidney imaging in this work. This wash for lipid enhancement was done by dipping the sample slide in 50 mM ammonium formate at 4°C three times for five seconds followed by desiccation prior to matrix application.

Proteins can also be detected from a tissue sections without any wash, however, due to the high concentration of lipids and salts in the tissue, suppression of the MALDI MS signal is often observed. A common wash documented in the literature for protein studies uses a graded ethanol series. For high spatial resolution imaging in the kidney, it

was found that a more stringent wash was necessary to remove the lipids to increase sensitivity for protein detection. Given this, kidney sections were processed using a washing procedure described by Yang *et al.*⁸¹ Specifically, the sample slide was immersed in 70% ethanol for 30 s, 100% ethanol for 30 s, Carnoy's fluid for 2 m, 100% ethanol for 30 s, water for 30 s, and then 95% ethanol for 30 s.

Matrix Application for Micro-Structure Analysis

Matrix Deposition Methods for Imaging

A major issue for achieving high resolution images of biological tissue sections with MALDI MS is sample preparation. Appropriate sample preparation methods will create a fine, uniform, and densely packed matrix crystal surface that has sufficient sensitivity for the analytes of interest. Current matrix application methods for protein analysis involve spraying or spotting the matrix in a solvent solution on to the tissue section. The solvent aids in the extraction of proteins and peptides from the tissue, which then co-crystallize with the matrix on the sample surface, and increase the availability of these analytes for detection. However, applying the matrix in a solvent solution in this way may contribute to analyte delocalization and formation of crystals $>20\ \mu\text{m}$, limiting the usefulness of a $<10\ \mu\text{m}$ laser beam for high spatial resolution imaging. Figure 2.3A shows crystals formed using micro-spotting and spraying matrix dissolved in solvent. Micro-spotting involves deposition of matrix droplets in an array with a robotic spotter. Imaging resolution is thus limited by the size of the dried droplets and the pitch in which they are spotted (typical resolution $\geq 150\ \mu\text{m}$). Spraying the matrix has the advantage of continuous matrix coverage across the sample, but crystals tend to be larger than $25\ \mu\text{m}$ and there are gaps on the order of $15\ \mu\text{m}$. The large crystals and gaps introduce imaging

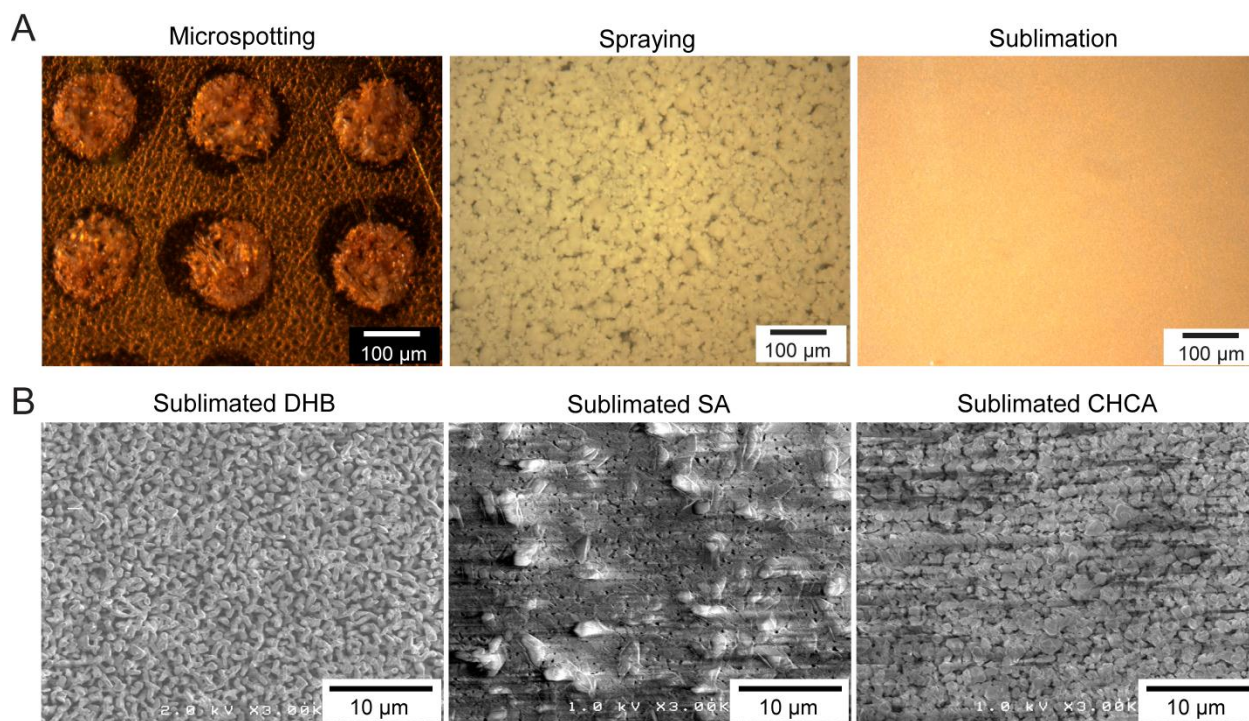


Figure 2.3. Optical and SEM analysis after MALDI matrix deposition. (A) Optical images of matrix crystals applied by microspotting, spraying, and sublimation. Scale bar = 100 μm . (B) SEM micrographs of sublimated DHB, SA, and CHCA on a gold plate. Sublimated matrix layers lack gaps in the surface and the crystals are on the order of 1 μm . Scale bar = 10 μm .

artifacts when the laser spot size is on the order of or smaller than these features. Matrix deposition by sublimation has overcome the crystal size and coverage problem for lipid analysis by producing a uniform and fine grain size of the matrix.⁶¹ As seen in the optical image and the SEM micrographs in Figure 2.3, sublimation produces uniform and complete matrix coverage and crystals on the order of 1 μm . SEM micrographs of three commonly used MALDI matrices are shown for demonstration. Sublimation was first introduced as a method of matrix deposition for imaging by Hankin *et al.* in 2007. However, due to the dry coating conditions this method was limited to analysis of lipids which are abundant on the tissue surface. Proteins were not detected with this solvent-free preparation method, presumably due to lack of sufficient contact between the proteins within the tissue and the matrix deposited on the surface. A method was recently published that involves recrystallization of a sublimated matrix on plate spotted samples.⁸⁰ The recrystallization process retained the small crystal size produced by the sublimation but was able to detect peptides with increased sensitivity. This concept has been extended to tissue imaging applications for the detection of peptides and proteins. A spectrum from a single pixel acquired from a kidney sublimated with CHCA followed by rehydration is displayed in Figure 2.4 showing detection of protein signals. Without rehydration no protein signal was detected. With sublimation now amenable to both lipid and protein imaging, high spatial ($\leq 25 \mu\text{m}$) resolution is now achievable for both of these classes of molecules.

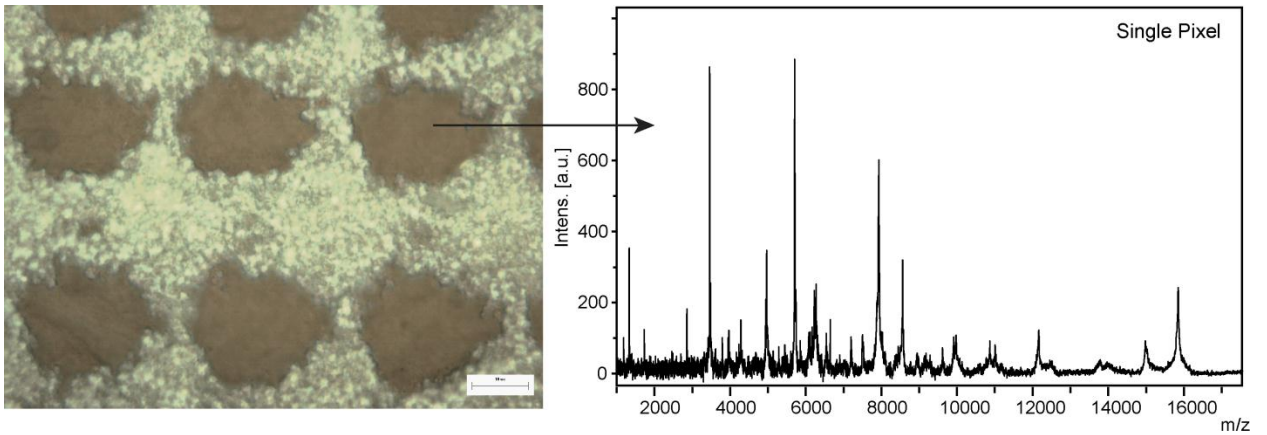


Figure 2.4. Protein IMS at high spatial resolution. The optical image shows the MALDI laser ablation regions from a sublimated/rehydrated CHCA matrix coating. The spectrum displayed is from a single pixel in the image. Scale bar = 10 μm .

Matrix Choice for Lipids and Proteins

While hundreds of compounds have been tested for use as MALDI matrices, only a handful are used for most applications. As discussed in the previous section, matrix deposition by sublimation was found to be necessary for the spatial resolution required for imaging glomeruli and tubules in the mouse kidney. In Table 2.1, matrices and their sublimation conditions are listed that were found to produce high quality signal in the kidney.

For many reported lipid studies 2,5-dihydroxybenzoic acid (DHB) has been a widely used matrix but, recently, 1,5-diaminonaphthalene (DAN) has garnered more attention due to its high sensitivity in both positive and negative mode.⁹² Figure 2.5 shows an average spectrum from serial kidney sections prepared with DAN or DHB. The spectra were collected using the same laser and instrumental conditions and the signal intensity increased approximately an order of magnitude with DAN compared to DHB in both positive and negative mode. As laser spot sizes get smaller, the sample ablation area (and thus number of molecules ablated) gets smaller as well so the increased sensitivity that DAN yields is especially important at high spatial resolution. DAN has been found to produce high quality lipid spectra with laser spot sizes at 10 μm down to even 2 μm , which is the smallest laser beam used in this work. In Figure 2.6, a kidney cortex is imaged at 10 μm spatial resolution for lipids with DAN displaying a number of unique kidney structures with specific lipid patterns. While DAN has been found to produce high quality spectra for many phospho- and glyco- lipids, surveying of matrices for best sensitivity is recommended particularly if a specific analyte of interest is being targeted. For example, in this work, we were interested in detecting glucose modified

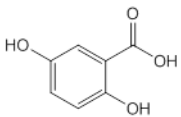
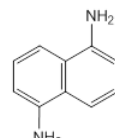
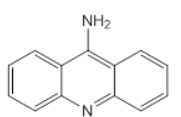
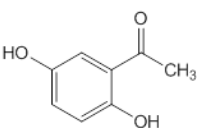
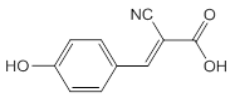
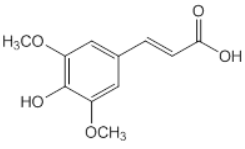
Matrix (Abbr.)	Formula	MW (Da)	Structure	Sub T (°C)	Sub Time (min)	Use
2,5-dihydroxybenzoic acid (DHB)	C ₇ H ₆ O ₄	154.026		110	7	lipids
1,5-Diaminonaphthalene (DAN)	C ₁₀ H ₁₀ N ₂	158.084		110	7	lipids
9-Aminoacridine (9-AA)	C ₁₃ H ₁₀ N ₂	194.084		150	12	lipids
2,5-Dihydroxyacetophenone (DHA)	C ₈ H ₈ O ₃	152.047		105	6	lipids, proteins
α -Cyano-4-hydroxycinnamic acid (CHCA)	C ₁₀ H ₇ NO ₃	189.042		135	30	peptides, proteins
Sinapinic Acid (SA)	C ₁₁ H ₁₂ O ₅	224.068		120	18	proteins

Table 2.1. Matrices and sublimation conditions used for high spatial resolution IMS.

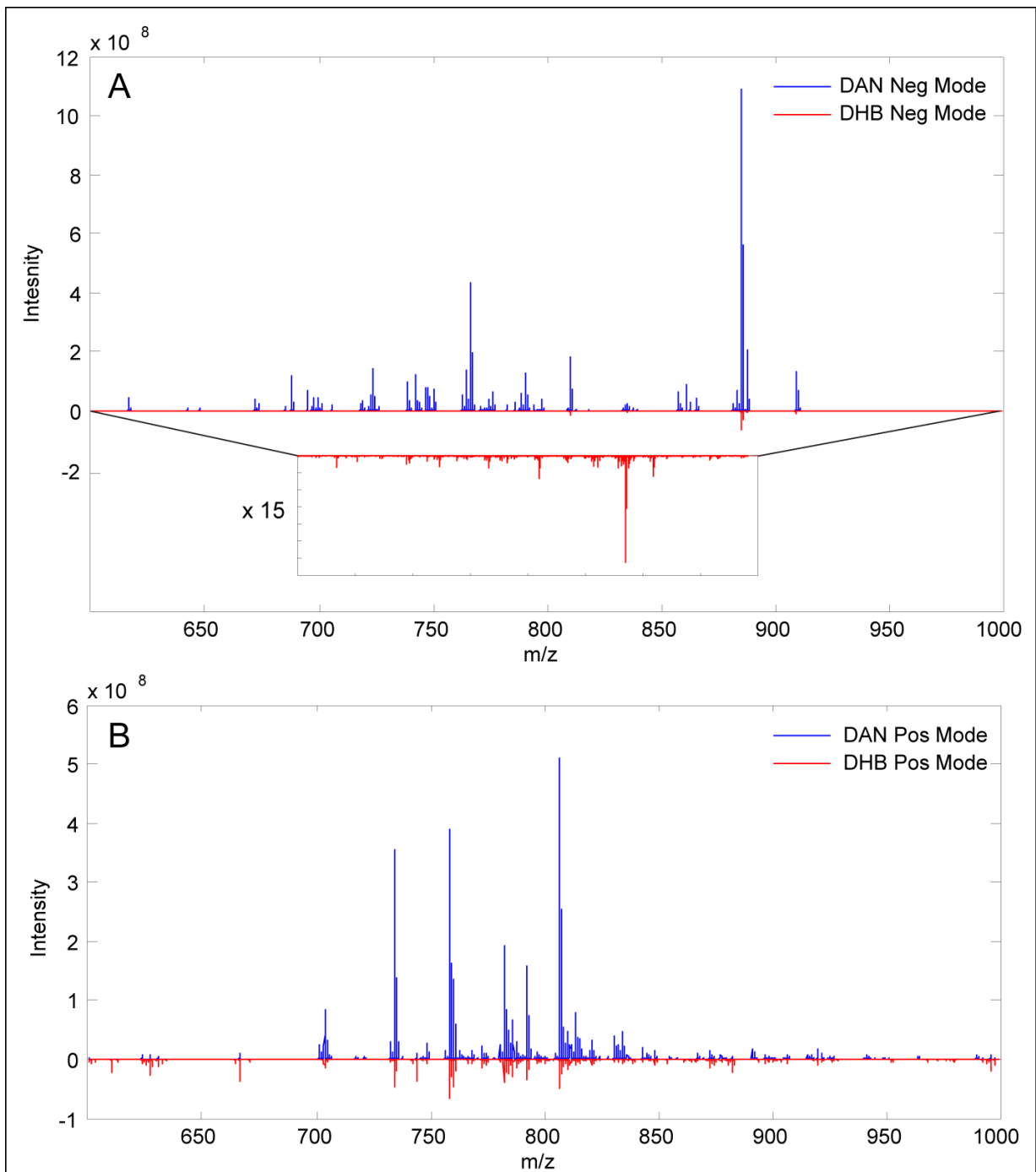


Figure 2.5. Comparison of DAN and DHB as a matrix for kidney lipid analysis. Negative mode (A) and positive mode (B) spectra from a kidney cortex comparing DAN matrix (blue) and DHB matrix (red). The same laser and instrumental conditions were used for both matrices.

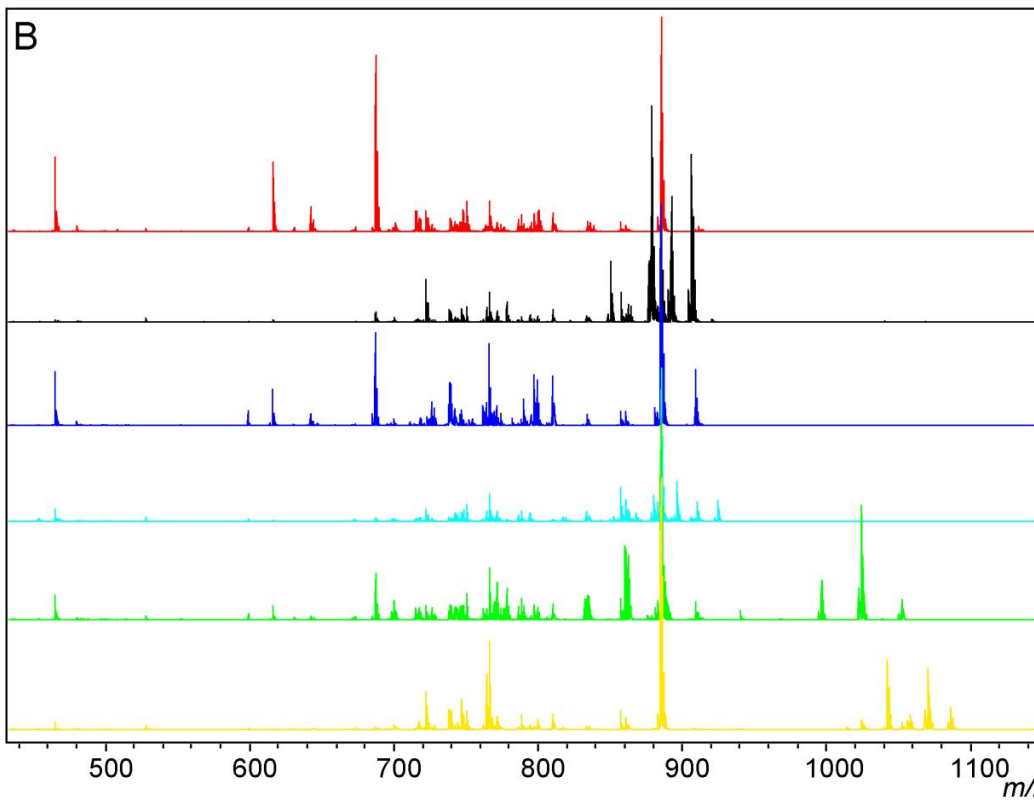
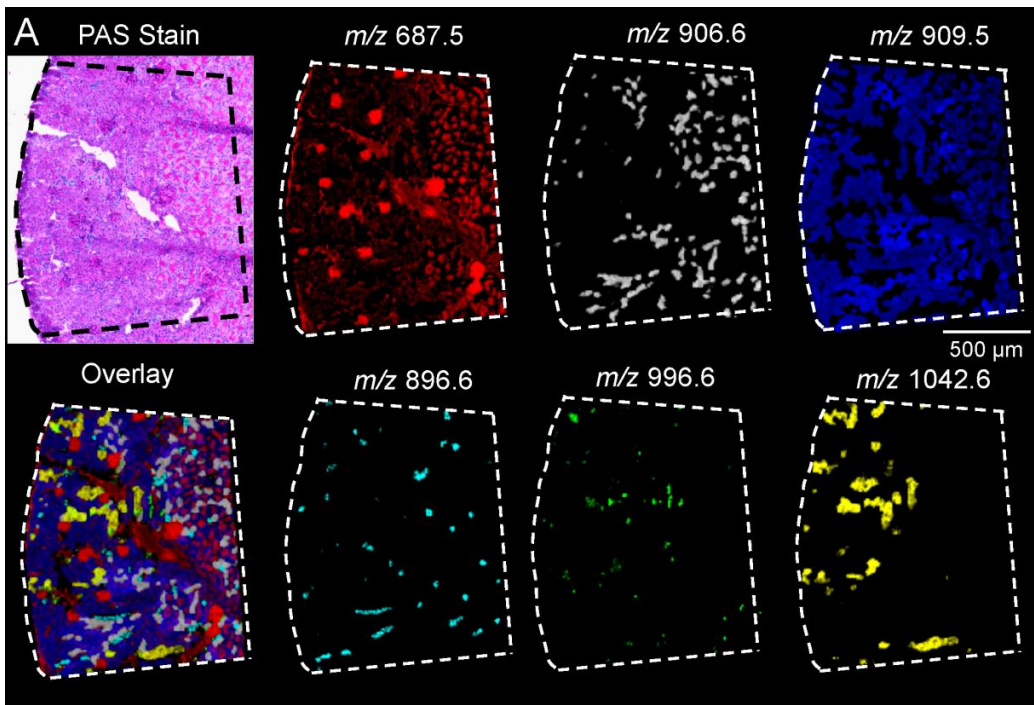


Figure 2.6. 10 μm resolution lipid imaging with DAN. (A) Selected ion images showing lipid localization in micro-structures of the kidney cortex. (B) Spectra selected from regions of the kidney where the color of the spectrum corresponds to the region from panel A with the same color.

aminophospholipids (i.e.- phosphatidylethanolamine (PE), described in chapter 3) which were suspected to be present in diabetic tissue. Use of DAN did not detect any glucose modified PEs in the kidney tissue but 9-aminoacridine (9-AA) increased the sensitivity of detection for this class of molecules. It should also be noted that while negative mode MALDI MS of lipids typically produces $[M-H]^-$ ions, the use of both 9-AA and DAN can produce $[M-CH_3]^-$ ions of phosphatidylcholine (PC) and sphingomyelin (SM) species, lipids usually detected in positive mode due to their permanent positive charge.^{93, 94} These $[M-CH_3]^-$ ions can overlap in mass with $[M-H]^-$ ions of PEs so care needs to be taken to distinguish these classes when making lipid assignments.

For protein and peptide analysis, sinapinic acid (SA) and α -cyano-4-hydroxycinnamic acid (CHCA) are the most commonly used compounds. These matrices were able to be sublimated on to a tissue surface but no protein signal could be detected with sublimation alone. As mentioned above, a rehydration step was found to be necessary to produce peptide and protein signal from matrix sublimated on a tissue surface. Rehydration is accomplished in a sealed petri dish containing 1 mL of 5% TFA at 85°C for 3.5 minutes. Sublimation/rehydration is suitable for high spatial resolution IMS of proteins as can be seen in the 25 μ m image in Figure 2.7. Protein signals specific to the glomerulus are displayed.

Matrix Deposition for Histology Directed IMS to Target Glomeruli

Histology-directed MALDI MS is an approach to imaging that combines histological information with robotics to target specific tissue regions. This method is advantageous in that it is targeted and much faster than imaging an entire tissue section. Histology-directed IMS has been previously described,⁶⁶ but some specific modifications

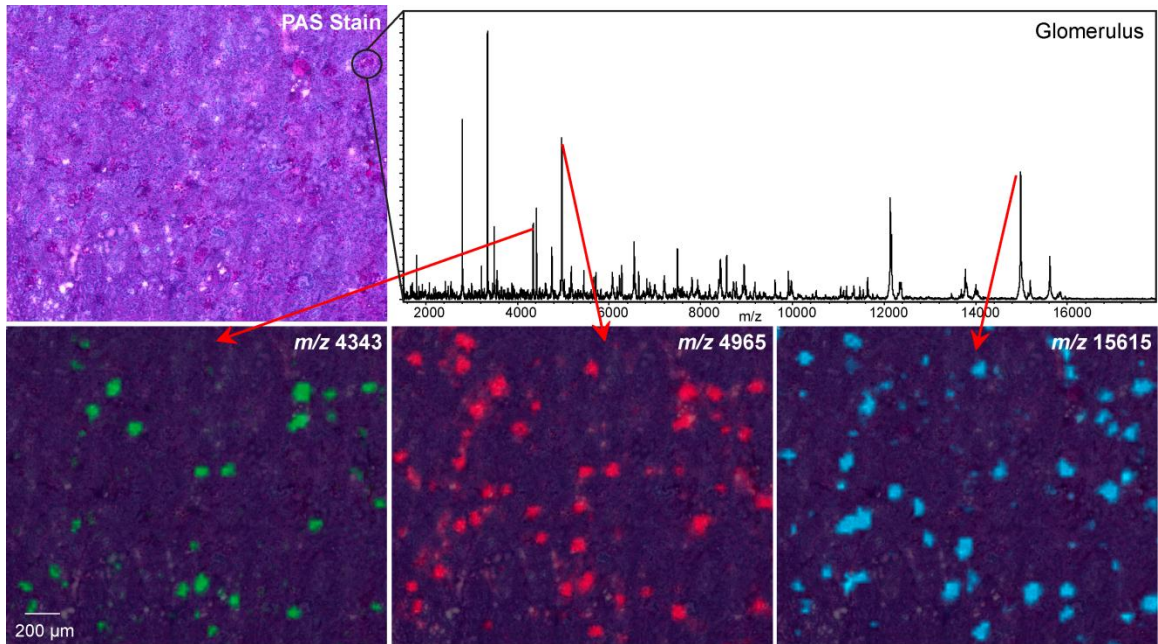
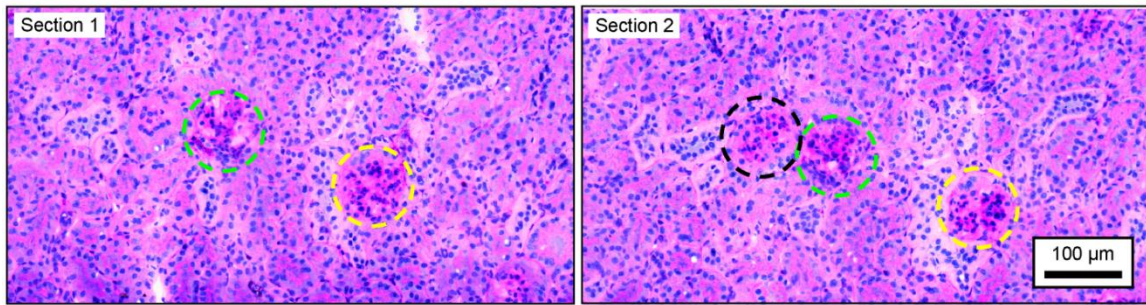


Figure 2.7. 25 μm resolution protein imaging with sublimated/rehydrated CHCA. Protein signals specific to the glomerulus are displayed.

to the published procedure are necessary to target glomeruli. Previous work used a histology stain on a serial section to guide the coordinate selection for analysis. However, targeting glomeruli requires use of the same section for both identification of tissue features (i.e. - glomeruli) and MALDI MS analysis. This is demonstrated in Figure 2.8A where it can be seen that a glomerulus observed in one section may not be present in the serial section. Additionally, while many glomeruli do track from one section to the next one, the relative positions of each translate differently in space with respect to another. Serial sections are often used because many common histology stains (such as H&E and PAS) interfere with MALDI MS signal. However, certain stains have been found to be compatible with MALDI MS such as cresyl violet.⁹⁵ Though this stain does not give as much histological information as H&E or PAS, it provides enough contrast to pick out glomeruli structures. Kidney sections mounted on an ITO glass slide can be stained with 0.5% cresyl violet for 30 s followed by an ethanol rinse for 15 s to aid in distinguishing the glomeruli under a microscope. After scanning the sample slide, the glomeruli can be identified and their coordinates recorded with respect to a set of fiducials on the MALDI slide. These coordinates can then be transferred to the automated acoustic robotic spotter (Portrait 630, Labcyte). In addition to spotting MALDI matrix, this robotic spotter can also deposit picoliter volumes of trypsin for *in situ* enzymatic digestion of proteins before matrix spotting.⁹⁶ In this way, MALDI MS/MS can be performed on peptides from these spots for identification of proteins. In this work, trypsin solution (76 ng/ μ L trypsin in 100 mM ammonium bicarbonate/10% acetonitrile) was spotted on the selected glomeruli in single droplets (~120 pL) for a total of 40 iterations allowing each droplet to dry for two minutes before spotting the next droplet. Proteolytic digestion was allowed to take place

A. Serial Sections



B. MALDI MS of Single Glomerulus

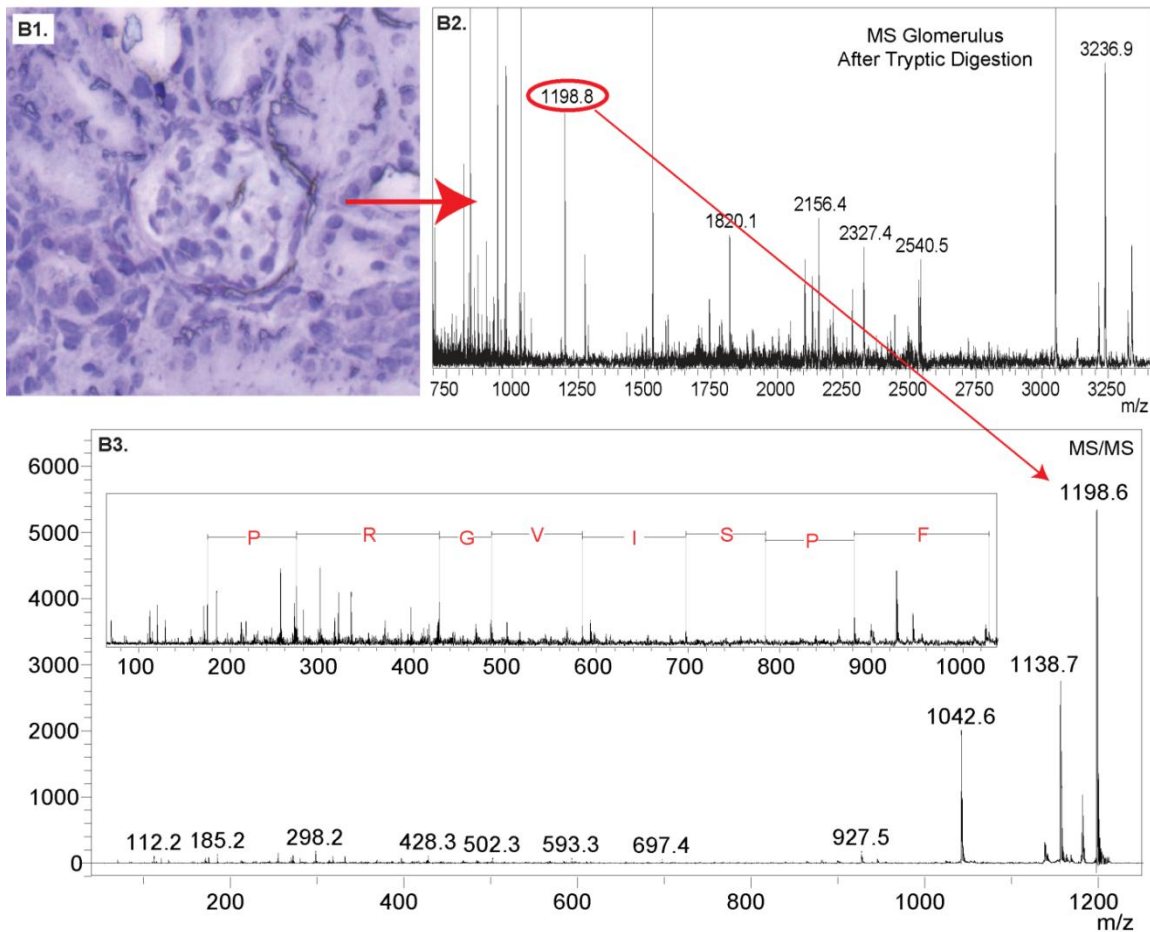


Figure 2.8 Glomerulus analysis with histology-directed profiling. (A) PAS stain of serial sections showing glomeruli. Glomeruli circled in yellow and green represent the same glomerulus in each section. The glomerulus circled in black is not found in the serial section demonstrating that the same section for picking coordinates (i.e. glomeruli) needs to be used for MS analysis. (B1) Cresyl violet stained glomerulus from *eNOS^{-/-} db/db* kidney section. (B2) MALDI MS spectrum of tryptic peptides from a selected glomerulus; peptide at m/z 1198 was sequenced using tandem MS mode. (B3) Tandem MS (MS/MS) spectrum and corresponding amino acid sequence of the peptide at m/z 1198; the peptide was identified as a tryptic fragment of actin by searching the mouse SwissProt database with MASCOT software.

for approximately two hours. Subsequently, MALDI matrix (10 mg/mL CHCA in 1:1 v/v mixture of acetonitrile and 0.2% trifluoroacetic acid) was robotically spotted on the trypsin digested glomeruli. An example of a spectrum from a single glomerulus is shown in Figure 2.8B. This type of workflow allows for protein identification directly from the tissue section by MS/MS fragmentation of the tryptic peptides along with database searching.

MALDI MS Instrumental Considerations for Direct Kidney Analysis

Imaging Resolution Considerations

The spatial resolution of an imaging experiment is most simply determined by the size of the laser beam spot on target and the pitch, or step size of the stage, between laser ablation spots. However, in practice, this is also dependent on the matrix crystal size. Lenses and improved optics have been used to focus the laser beam on the target. The commercial instruments used in this study can achieve a spot size of ~10 μm . However, others have achieved smaller laser spot sizes with special lenses with a co-axial laser beam path⁵² and laser beam filtration with a pinhole.⁷⁴ It is possible to image at a higher spatial resolution than the size of the laser beam using a technique is called oversampling. In oversampling, the matrix is completely ablated in an area and then the stage is moved a distance smaller than the ablation spot but enough so fresh material is available for ablation. While this has been used with some success, often it results in degradation of signal quality.

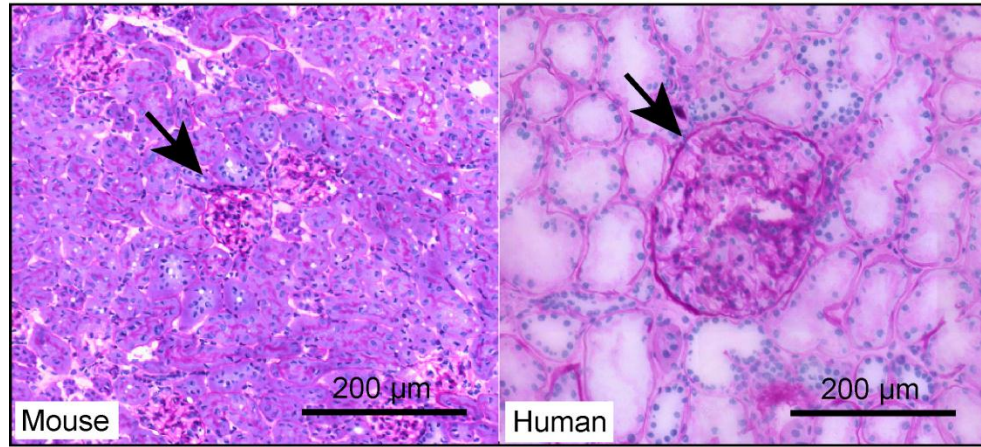
While increasing spatial resolution allows one to resolve smaller features and structures in a tissue section, there is a tradeoff. One has to consider the size of the features of interest, the time of the experiment, the size of the data and the sensitivity

required. In general, smaller spot sizes ablate less material and therefore the sensitivity goes down. One structure of interest in this study is the glomerulus. In humans this is $\sim 200 \mu\text{m}$, but in the mouse, the model used in this study, it is only $\sim 80 \mu\text{m}$ (Figure 2.9A). To adequately reconstruct ion images of a mouse glomerulus, a minimum of $50 \mu\text{m}$ spatial resolution has been found to be necessary but $\leq 30 \mu\text{m}$ is more desirable. While decreasing the pixel size increases the resolution of the glomerulus, it also increases the time of analysis and the data size if you are to image the same unit area. The number of pixels (i.e. number of spectra) is a square function of step size. As can be seen in Figure 2.9B, reducing the laser spot size from $100 \mu\text{m}$ to $25 \mu\text{m}$ (a factor of 4) increases the number of pixels (spectra) by 16 times.

Instrumentation for Imaging

MALDI sources can be interfaced with a number of different mass analyzers. In this work MALDI TOF and MALDI FTICR mass spectrometers are the main instruments used and the fundamentals of each have been described in Chapter I. As a general guideline, protein imaging is typically performed using linear TOFs and lipid imaging is most often done using reflectron TOFs and FTICR instruments where higher mass resolution is needed. In general, a linear TOF is the preferred instrument for protein imaging due to its speed, sensitivity, and theoretically unlimited mass range. In practice however, sensitivity and resolution cannot be optimized for all m/z values across a large mass range so instrument tuning is usually performed to optimize for given mass range. A Bruker Ultraflexxtreme MALDI TOF mass spectrometer equipped with a Smartbeam laser was the major instrument used for both lipid and protein imaging in this work.

A. Glomerulus Size



B. Laser Spot Size

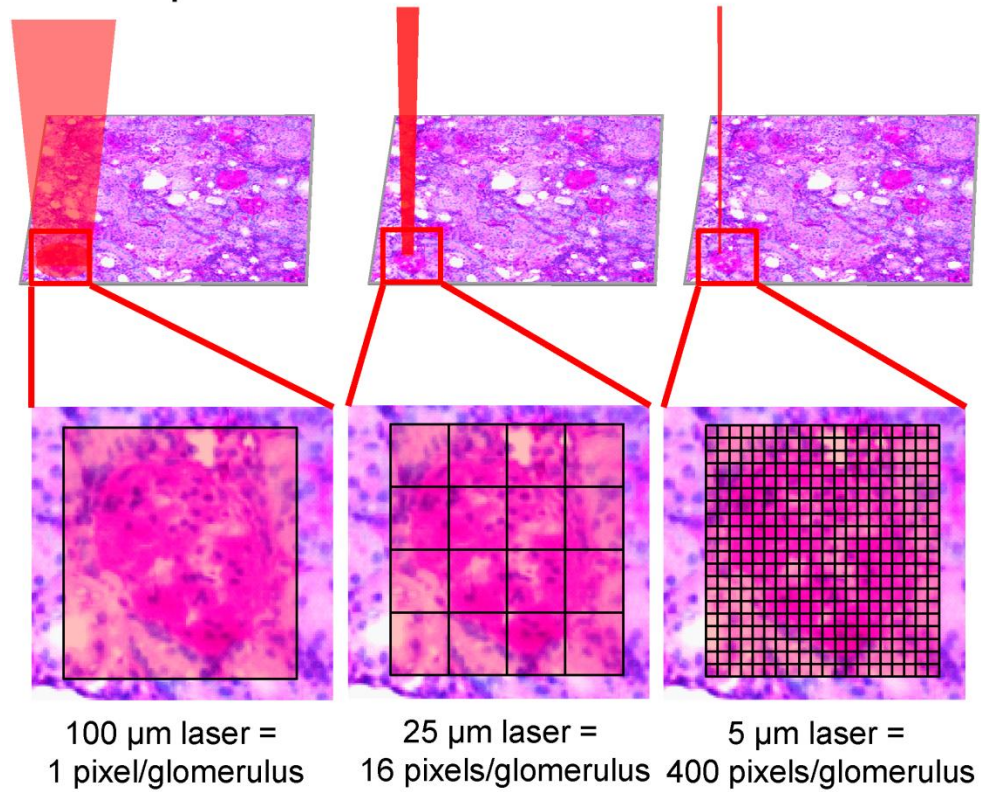


Figure 2.9. Spatial resolution considerations for IMS of glomeruli. (A) Comparison of size between a mouse glomerulus and a human glomerulus. (B) Schematic representation of how the laser spot size (and therefore resolution) affects the number of pixels acquired per glomerulus.

Protein imaging was performed using linear mode in the range of m/z 1,000 - 25,000 at a spatial resolution of 25 μm . Lipid imaging was performed on the same instrument in reflectron mode in the range of m/z 400 - 1,500 at a spatial resolution of 10 μm .

A MALDI FTICR MS was used in parallel to the TOF imaging experiments. Profiling and imaging experiments were performed on a 9.4T and 15T Bruker Solarix FTICR MS to obtain accurate mass measurements for ions of interest which assisted in the identification. In addition to high mass accuracy measurements, data can be acquired in continuous accumulation of selected ion (CASI) mode to increase the sensitivity of an experiment. In this mode, a selected m/z range is filtered in the quadrupole and accumulated in a hexapole before being sent into the ICR cell. By removing high intensity ions from other regions of the spectrum, low abundance species can be accumulated with a number of laser shots (hundreds to tens of thousands) before FTICR detection. Figure 2.10 demonstrates the increase in sensitivity and signal to noise across the lipid range in negative mode with CASI, where each color in Figure 2.10B represents a single CASI analysis. In this work CASI was utilized in the initial experiments that found glucose modified lipids in diabetic kidneys. This feature was also used extensively for lipid identification to increase the signal intensity of the parent ion before fragmentation.

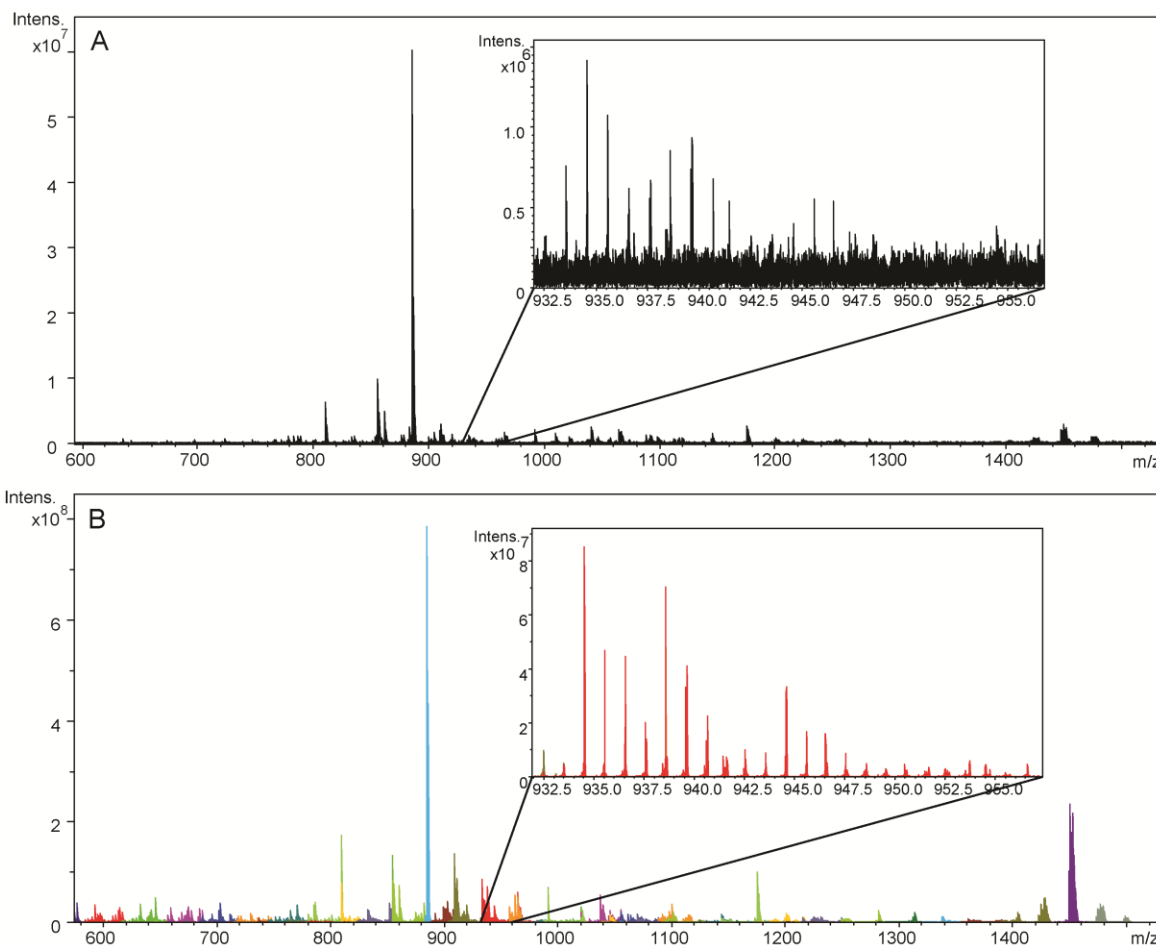


Figure 2.10. Sensitivity increase using CASI. (A) Standard full spectrum FTICR MS scan in negative ion mode. (B) Combined CASI spectra overlaid across the same mass range as in (A). Each color represents a single spectrum collected with a narrow mass window. Using CASI results in increased sensitivity and signal to noise as seen in the inset regions of (A) and (B).

Data Processing, Image Co-registration, and Image Analysis

Spectral Pre-processing

Spectral pre-processing is an important first step in analyzing imaging datasets. Pre-processing reduces experimental variance so that spectra within a single dataset and across multiple datasets can be better compared. Mass spectra are processed by background subtraction, normalization, and spectral realignment.⁹⁷ This helps reduce chemical noise, day to day instrument variations and signal intensity differences due to matrix coating. This not only allows for better comparison of expression differences between spectra but also increases image quality by increasing contrast and compensating for matrix inhomogeneity.

Histological Staining and Image Co-registration

After an imaging experiment is completed, the matrix can be washed off of the tissue section in a series of graded ethanols to allow for histological staining. H&E stain is a common and versatile stain that is often used. PAS is a stain of choice for kidney disease as it shows extracellular matrix build-up. After staining, the slide can be scanned and then the histology of the same section that was imaged with MS can be co-registered together to map ions of interest to specific structures within in the tissue section. This is particularly helpful for small tissue structures where it is difficult to find the corresponding histology without an overlay or in a serial section. Figure 2.11 shows an example of a co-registered PAS stain with the IMS data where specific lipid species can be seen to localize to specific kidney structures of glomeruli and tubules.

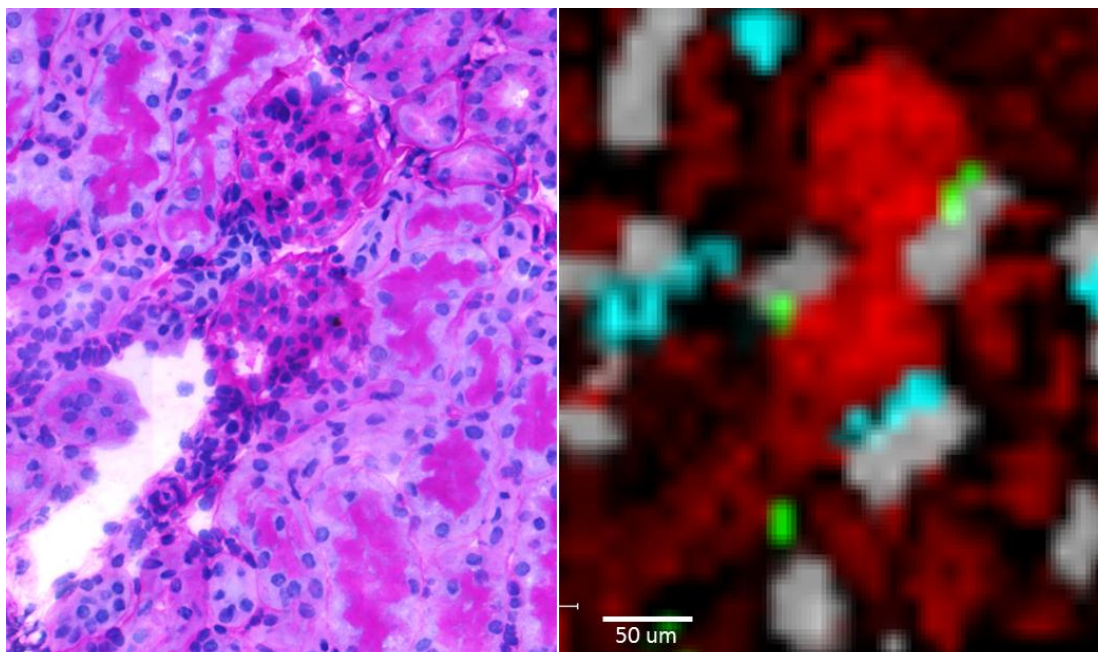


Figure 2.11. Co-registration with histology. Above is an example of several selected ion signals overlaid which show localization to distinct tissue structures. The PAS stained image on the left is the same section that the 10 μm IMS data was collected on. Ion image overlay displaying m/z 687.5 (red), m/z 896.6 (cyan), m/z 906.6 (white), and m/z 996.6 (green).

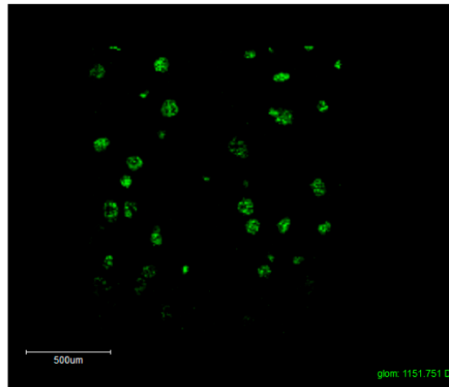
Data Analysis and Relative Quantitation with ImageJ

For MALDI imaging datasets, ImageJ software (National Institutes of Health, Bethesda, MD, USA) was used for relative quantitation of the lipid and protein species of interest. Monochromatic TIFF images were exported from FlexImaging to ImageJ. Areas of interest were selected in each image as individual glomeruli, tubules, or the entire kidney section. Signal intensity was measured as the mean intensity per area of interest. The general workflow for the ImageJ processing of ion images is shown in Figure 2.12. The mean and standard error were calculated for each MS peak of interest across the experimental groups. Differences were evaluated by the Kruskal-Wallis rank-sum test. Differences were considered statistically significant if p values were less than 0.05.

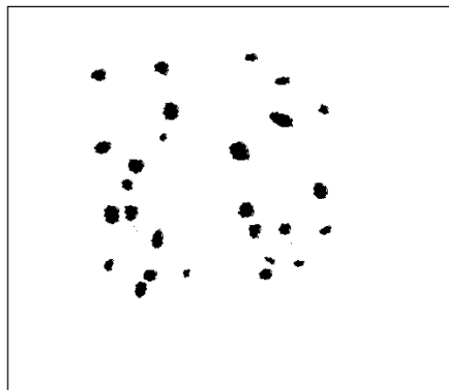
Conclusions

As demonstrated in this chapter, it is now possible to analyze the molecular composition in distinct renal tissue regions and even within smaller structures, such as individual renal glomeruli and tubules. In the following chapters these methods and workflows were applied to elucidate molecular changes under conditions of DN and examine the effect of a drug treatment. Chapter III will focus on changes in the lipid composition while Chapter IV will present findings on protein composition and changes in the kidneys of different experimental groups.

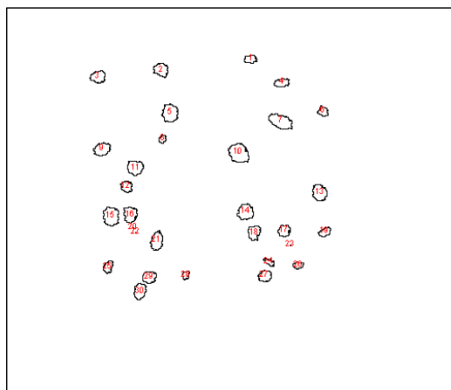
Export ion image as
monochromatic TIFF



Create mask, select regions
and apply to original data



Count regions and
calculate signal per area



Particle	Area	Mean Signal per Region
1	212	15.712
2	61	8.197
3	144	25.028
4	93	21.172
5	118	13.432

⋮

Figure 2.12. Workflow of ion image analysis with ImageJ.

Chapter III

DIABETIC NEPHROPATHY INDUCES ALTERATIONS IN THE GLOMERULAR AND TUBULE LIPID PROFILES

Overview

Diabetic nephropathy (DN) is a major life-threatening complication of diabetes. Renal lesions affect glomeruli and tubules but the pathogenesis is not completely understood. Phospholipids and glycolipids are molecules that carry out multiple cell functions in norm and disease and their role in DN pathogenesis is unknown. We employed high spatial resolution matrix-assisted laser desorption/ionization imaging mass spectrometry (MALDI IMS) to determine lipid changes in kidneys of *eNOS^{-/-} db/db* mice, a robust model of DN. Phospholipid and glycolipid structures, localization patterns, and relative tissue levels were determined in individual renal glomeruli and tubules without disturbing tissue morphology. Significant increase in the levels of specific glomerular and tubular lipid species from four different classes, i.e. gangliosides, sulfoglycosphingolipids, lysophospholipids, and phosphatidylethanolamines, were detected in diabetic kidneys compared to non-diabetic controls. Inhibition of non-enzymatic oxidative and glycooxidative pathways attenuated the increase in lipid levels and ameliorated renal pathology, even though blood glucose levels remained unchanged. Our data demonstrate that the levels of specific phospho- and glycolipids in glomeruli and/or tubules are associated with diabetic renal pathology. We suggest that

hyperglycemia-induced DN pathogenic mechanisms require intermediate oxidative steps that involve specific phospholipid and glycolipid species.

Introduction

Diabetic nephropathy (DN) can develop in about 1/3 of diabetic individuals and is characterized by specific glomerular and tubular lesions in the kidney. These lesions are associated with progression to end stage renal disease with subsequent requirement for renal dialysis and transplantation.² Despite the significance of DN, there is still incomplete understanding of the pathogenic mechanisms, particularly those underlying the differential susceptibility to DN.

Lipids may play a role in DN, but to date, the research focus has been on neutral lipids such as triacylglycerols and cholesterol.⁹⁸ Phospho- and glycolipids are two major classes of lipid molecules that carry out many biological functions ranging from regulation of physical properties of cellular membranes to cell signaling.^{99, 100} In diabetes, changes in the levels of these lipids in blood and tissues cause dysregulation of different cellular processes associated with pathogenesis.^{99, 101-105} Thus, phospho- and glycolipids may have a role in DN.

The present study is the first report of the application of MALDI IMS to investigate molecular changes in renal glomerular and tubular phospho- and glycolipids in DN. We utilized a set of experimental tools: a robust DN mouse model, which develops renal lesions comparable to those found in human disease;¹⁰⁶ a high spatial resolution MALDI IMS technology; and pyridoxamine (PM), which was employed to elucidate whether hyperglycemia induced oxidative pathways play a role in phospho- and glycolipid changes relevant to DN. PM is an inhibitor of oxidative and

glycoxidative reactions and has been shown to act via sequestration of redox active metal ions, scavenging of reactive carbonyl compounds, and scavenging of hydroxyl radical both *in vitro* and *in vivo*.^{21, 28, 107-110} We also used several different mouse models to further assess the association between renal damage and lipid profile. We determined molecular changes at the level of a single glomerulus or tubule, which has not been achieved in the previous studies of renal tissues using MALDI IMS.^{69, 87, 88} Our data demonstrated that the levels of specific phospho- and glycolipids in glomeruli and/or tubules of the kidney are associated with diabetic renal pathology. Inhibition of glycoxidative pathways, without lowering hyperglycemia, ameliorated lipid levels and renal lesions. We suggest that hyperglycemia-induced DN pathogenic mechanisms require intermediate oxidative steps that involve phospho- and glycolipids.

Results

Renal pathology in the eNOS^{-/-} C57BLKS db/db mouse model of Type 2 DN.

We employed eNOS^{-/-} C57BLKS *db/db* mice, the most robust mouse model of Type 2 DN to date. At >20 weeks of age, these mice exhibit albuminuria, arteriolar hyalinosis, increased glomerular basement membrane (GBM) thickness, mesangial expansion, mesangiolysis, focal segmental and early nodular glomerulosclerosis, and markedly decreased glomerular filtration rate.¹⁰⁶ In our study, eNOS^{-/-} C57BLKS *db/db* mice developed significant albuminuria at 6 weeks of age which increased dramatically by 22 weeks of age (Figure 3.1A). Treatment of diabetic mice with PM significantly ameliorated albuminuria at 22 weeks of age (Figure 3.1B). Kidneys of three animals from each treatment group were isolated and subjected to MALDI IMS analyses of lipids.

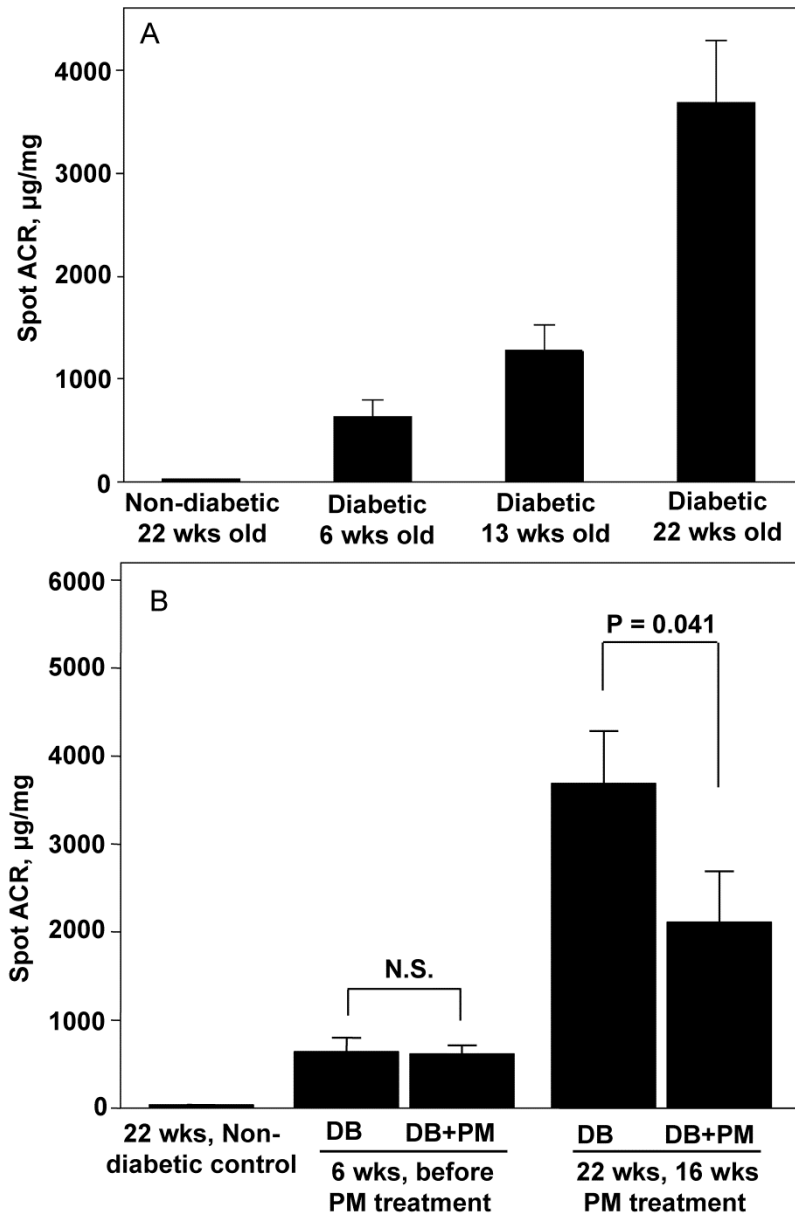


Figure 3.1. Urinary albumin-to-creatinine ratio (ACR) in diabetic mice and effect of PM treatment. (A) Urinary albumin-to-creatinine ratio in diabetic mice of different age. Urinary ACR was determined in non-diabetic control group and in diabetic group at the indicated age. (B) PM treatment of diabetic mice (400 mg/kg/day) started at 6 weeks of age and continued until 22 weeks of age. Urinary ACR in diabetic (DB) and diabetic + PM (DB+PM) groups was determined before and at the end of PM treatment; urinary ACR in non-diabetic control group was determined at 22 weeks of age. Each bar graph represents the mean \pm SEM (n=8). N.S. – not significant.

Blood glucose levels and renal pathology data for these mice are presented in Figure 3.2. Diabetic mice exhibited dramatic increase in glomerular and tubular pathologic lesions; PM treatment significantly ameliorated these lesions (Figure 3.2B-E). Interestingly, PM treatment did not inhibit hyperglycemia itself (Figure 3.2A). Therefore, use of PM treatment allowed us to compare renal lipid profiles in hyperglycemic animals with significantly different degrees of renal pathology.

Composition of mouse renal glomerular and tubular phospho- and glycolipids.

MALDI IMS was performed on renal sections from three biological replicates in each experimental group (non-diabetic, diabetic, and diabetic + PM). Because DN lesions affect primarily glomeruli and tubules, we focused on the lipid molecular patterns localized specifically within glomerular and tubular areas of the renal cortex. We examined 60-70 glomeruli and/or tubules per mouse in each experimental group. Multiple species that belong to different lipid classes were identified within glomerular and tubular structures (Table 3.1).

We then focused only on those specific phospho- and glycolipid species that exhibited significant changes in glomerular and/or tubular levels in diabetes compared to control. These species belonged to four lipid classes: gangliosides, sulfoglycosphingolipids, lysophospholipids, and phosphatidylethanolamines and are highlighted in Table 3.1.

Glomerular levels of major ganglioside NeuGc-GM3 are increased in DN.

Gangliosides are anionic glycosphingolipids located to the outer leaflet of plasma membranes and characterized by the presence of sialic acid in their structure.¹¹¹

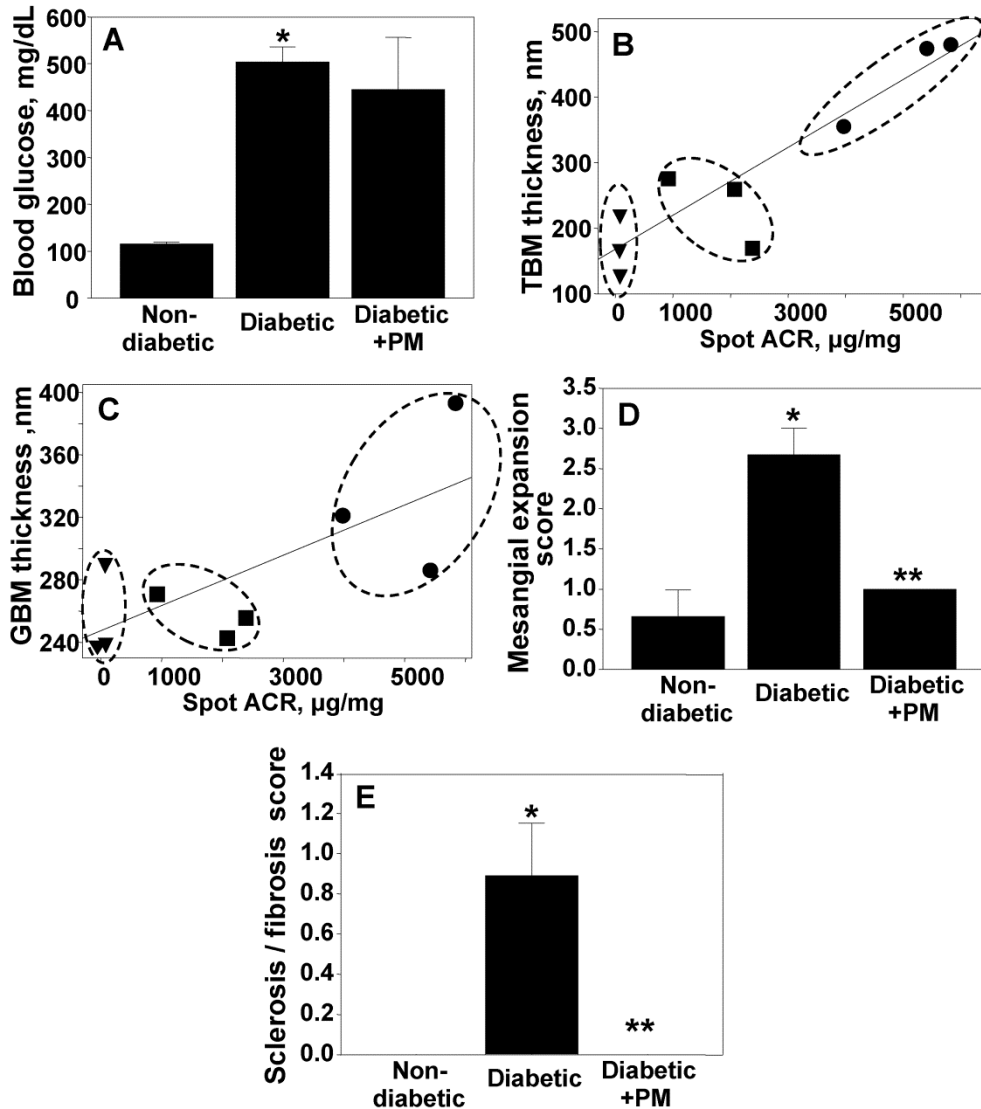


Figure 3.2. Renal injury and effect of PM treatment in kidneys. Animal groups and treatments were the same as in Figure 1. (A) Blood glucose levels. Correlation between tubular basement membrane (TBM) (B) or GBM (C) thickness and albuminuria: non-diabetic control (triangles), diabetic (circles), and diabetic treated with PM (squares). Expansion of renal mesangial matrix (D) and renal sclerosis/fibrosis (E) were scored on a scale of 0 to 3 as described under Methods. Sclerosis/fibrosis score is an average of the scores for global sclerosis, interstitial fibrosis and vascular fibrosis. Each bar graph represents the mean \pm SEM. * - $p < 0.05$, diabetic vs. non-diabetic groups; ** - $p < 0.05$, diabetic vs. diabetic + PM groups; $n = 3$.

Table 3.1. Composition of mouse renal glomerular and tubular lipids determined by direct tissue MALDI MS analysis. Lipids shown in **red bold** font were detected only in diabetic kidneys while the rest were detected in all experimental groups. All lipids were identified by MS/MS fragmentation analysis. *- lipid species identified with accurate mass and only head group specific fragments. Probable side chains included. †- resulted from the decomposition of SB1a during the ionization process.^{87, 112}

Lipid Class	Lipid ID	Theoretical <i>m/z</i>	Ion Species	Error (ppm)	Localization
I. Phospholipids					
Lysophospholipids	LPA (18:0)	437.2673	[M-H]⁻	-0.23	Glomerular
	LPC (16:0)	480.3095	[M-CH₃]⁻	-0.42	Glomerular
	LPC (18:2)	504.3095	[M-CH₃]⁻	-0.40	Glomerular
	LPC (18:0)	508.3408	[M-CH₃]⁻	-0.39	Glomerular
Glycerophospholipids	PA (18:0/18:1)	701.5127	[M-H] ⁻	0.57	Glomerular
	PE (16:0/20:4)	738.5079	[M-H] ⁻	0.70	Tubular
	PE (18:1/18:2)	740.5236	[M-H] ⁻	0.63	Tubular
	PE (18:2/18:0)	742.5392	[M-H] ⁻	0.85	Tubular
	PA (18:0/22:5)	749.5127	[M-H] ⁻	0.67	Glomerular
	PE (16:0/22:6)	762.5079	[M-H] ⁻	-0.31	Tubular
	PE (18:1/20:4)	764.5236	[M-H] ⁻	1.03	Tubular
	PE (18:0/20:4)	766.5392	[M-H] ⁻	-0.01	Tubular
	PE (40:8)	786.5079	[M-H] ⁻	0.12	Tubular
	PE (18:1/22:6)	788.5236	[M-H] ⁻	1.09	Tubular
	PE (18:0/22:6)	790.5392	[M-H] ⁻	-0.37	Tubular
	PS (38:3)	812.5447	[M-H] ⁻	0.49	Glomerular
	PS (40:5)	836.5447	[M-H] ⁻	1.20	Glomerular
	PS (40:4)	838.5603	[M-H] ⁻	1.19	Glomerular
	PI (18:0/22:4)	909.5499	[M-H] ⁻	-0.22	Tubular
	PI (18:0/22:4)	913.5811	[M-H] ⁻	1.42	Glomerular
Plasmalogens	PE (P-36:4)	722.513	[M-H] ⁻	0.97	Glomerular, tubular
	PE (P-16:0/22:6)	746.513	[M-H] ⁻	0.45	Glomerular, tubular
	PE (P-38:5)	748.5287	[M-H] ⁻	0.67	Glomerular, tubular
	PE (P-18:0/20:4)	750.5443	[M-H] ⁻	0.24	Glomerular, tubular
	PE (P-18:0/22:6)	774.5443	[M-H] ⁻	-0.08	Glomerular, tubular
Sphingophospholipids	SM (d18:1/16:0)	687.5446	[M-CH ₃] ⁻	1.02	Glomerular
	SM (d18:1/18:0)	715.5759	[M-CH ₃] ⁻	0.00	Glomerular

Table 3.1 (continued).

Lipid Class	Lipid ID	Theoretical <i>m/z</i>	Ion Species	Error (ppm)	Localization
I. Phospholipids (cont.)					
Glycated Phosphatidylethanolamine	Amadori-PE (P-36:4)	884.5658	[M-H] ⁻	-0.97	Glomerular, tubular
	Amadori-PE (36:5)	898.5451	[M-H] ⁻	0.56	Tubular
	Amadori-PE (16:0/20:4)	900.5607	[M-H] ⁻	-0.33	Tubular
	Amadori-PE (18:1/18:2)	902.5764	[M-H] ⁻	0.55	Tubular
	Amadori-PE (18:2/18:0)	904.592	[M-H] ⁻	0.55	Tubular
	Amadori-PE (P-38:6)	908.5658	[M-H] ⁻	0.28	Glomerular, tubular
	Amadori-PE (P-18:1/20:4)	910.5815	[M-H] ⁻	1.76	Glomerular, tubular
	Amadori-PE (P-18:0/20:4)	912.5971	[M-H] ⁻	-0.33	Glomerular, tubular
	Amadori-PE (16:0/22:6)	924.5607	[M-H] ⁻	-0.54	Tubular
	Amadori-PE (18:1/20:4)	926.5764	[M-H] ⁻	-0.86	Tubular
	Amadori-PE (18:0/20:4)	928.592	[M-H] ⁻	-0.32	Tubular
	Amadori-PE (P-40:7)	934.5815	[M-H] ⁻	0.21	Glomerular, tubular
	Amadori-PE (P-18:0/22:6)	936.5971	[M-H] ⁻	-0.11	Glomerular, tubular
	Amadori-PE (40:8)	948.5607	[M-H] ⁻	-0.95	Tubular
	Amadori-PE (18:1/22:6)	950.5764	[M-H] ⁻	0.21	Tubular
	Amadori-PE (18:0/22:6)	952.592	[M-H] ⁻	0.52	Tubular
II. Glycolipids					
Sulfoglycosphingolipids	SM4s(d18:1/h20:0)	850.571	[M-H] ⁻	0.94	Tubular
	SM4s(d18:1/h22:0)	878.6033	[M-H] ⁻	0.23	Tubular
	SM4s(d18:1/h24:1)	904.6189	[M-H] ⁻	-0.33	Tubular
	SM4s(d18:1/h24:0)	906.6346	[M-H] ⁻	-0.22	Tubular
	SM3(t18:0/20:0)*	1014.6405	[M-H] ⁻	-0.10	Tubular
	SM3(d18:1/22:0)	1024.6612	[M-H] ⁻	0.20	Tubular
	SM3(d18:1/h22:0)	1040.656	[M-H] ⁻	0.29	Tubular
	SM3(t18:0/22:0)	1042.6718	[M-H] ⁻	0.86	Tubular
	SM3(d18:1/24:1)	1050.6768	[M-H] ⁻	-0.10	Tubular
	SM3(d18:1/24:0)	1052.6925	[M-H] ⁻	0.09	Tubular
	SM3(t18:0/h22:0)	1058.666	[M-H] ⁻	1.04	Tubular
	SM3(d18:1/h24:1)	1066.671	[M-H] ⁻	0.66	Tubular
	SM3(d18:1/h24:0)	1068.6874	[M-H] ⁻	0.19	Tubular
	SM3(t18:0/24:0)	1070.7031	[M-H] ⁻	0.28	Tubular

Table 3.1 (continued).

Lipid Class	Lipid ID	Theoretical m/z	Ion Species	Error (ppm)	Localization
II. Glycolipids (cont.)					
Sulfoglycosphingolipids (cont.)	SM3(t18:0/h24:1)	1084.682	[M-H] ⁻	0.92	Tubular
	SM3(t18:0/h24:0)	1086.697	[M-H] ⁻	0.18	Tubular
	SM2a(d18:1/22:0)*	1227.7406	[M-H]⁻	-0.57	Tubular
	SM2a(t18:0/22:0)*	1245.7511	[M-H]⁻	-0.16	Tubular
	SM2a(d18:1/24:0)*	1255.7719	[M-H]⁻	1.04	Tubular
	SM2a(d18:1/h24:0)*	1271.7668	[M-H]⁻	-0.94	Tubular
	SM2a(t18:0/24:0)*	1273.7824	[M-H]⁻	0.47	Tubular
	SB1a(t18:0/20:0)*	1379.7727	[M-SO₃H]⁻	-0.94	Tubular
	SM1a(t18:0/20:0)*†	1379.7727	[M-H]⁻	-0.94	Tubular
	SB1a(d18:1/22:0)*	1389.7934	[M-SO₃H]⁻	0.07	Tubular
	SM1a(d18:1/22:0)*†	1389.7934	[M-H]⁻	0.07	Tubular
	SB1a(t18:0/22:0)*	1407.804	[M-SO₃H]⁻	0.92	Tubular
	SM1a(t18:0/22:0)*†	1407.804	[M-H]⁻	0.92	Tubular
	SB1a(d18:1/24:0)*	1417.8247	[M-SO₃H]⁻	-0.42	Tubular
	SM1a(d18:1/24:0)*†	1417.8247	[M-H]⁻	-0.42	Tubular
	SB1a(d18:1/h24:0)*	1433.8196	[M-SO₃H]⁻	-0.70	Tubular
	SM1a(d18:1/h24:0)*†	1433.8196	[M-H]⁻	-0.70	Tubular
	SB1a(t18:0/24:0)*	1435.8353	[M-SO₃H]⁻	-0.42	Tubular
	SM1a(t18:0/24:0)*†	1435.8353	[M-H]⁻	-0.42	Tubular
Gangliosides	NeuAc-GM3 (d18:1/16:0)*	1151.7059	[M-H] ⁻	-0.17	Glomerular
	NeuGc-GM3 (d18:1/16:0)*	1167.7008	[M-H]⁻	-0.51	Glomerular

Gangliosides are known to play major roles in cell-cell and cell-matrix recognition via interactions with integrins, matrix proteins and other glycosphingolipids as well as in innate immunity, apoptosis and carcinogenesis.¹¹³⁻¹¹⁵ We determined renal localization and levels of two abundant mammalian gangliosides, NeuAc-GM3 (m/z 1151.7) and its hydroxylated derivative NeuGc-GM3 (m/z 1167.7) (Figure 3.3). Both ganglioside species were localized exclusively to renal glomeruli (Figure 3.3A and B). However, there was a distinct difference in the response of these species to our experimental treatments. NeuAc-GM3 was detected at relatively high levels that were not significantly different in all treatment groups (Figure 3.3A, top row and 3.3D). In contrast, NeuGc-GM3 was present at relatively low levels in the glomeruli of non-diabetic animals but increased ~8-fold in the glomeruli of diabetic mice (Figure 3.3A, bottom row and 3.3D). Diabetic mice treated with PM had significantly lower levels of NeuGc-GM3 compared to untreated diabetic mice. (Figure 3.3A, bottom row and 3.3D). Levels of NeuGc-GM3 were proportional to the degree of renal damage as determined using 13 week old $eNOS^{-/-}$ db/db mice (Figure 3.1A and 3.4A) and 22 week old db/db and $eNOS^{-/-}$ mice (Figure 3.4B).¹⁰⁶

Levels of long-chain series sulfoglycolipids are increased within renal tubules in DN. Sulfoglycolipids are produced from glycosphingolipids via addition of one or several sulfate esters catalyzed by the enzyme cerebroside sulfotransferase (CST). Sulfoglycolipids are essential in such key biological processes as nerve fiber myelination and spermatogenesis.¹¹⁶ They are also enriched in mammalian kidneys where they have been shown to be involved in osmoregulation and acid-base homeostasis.^{117, 118} We have

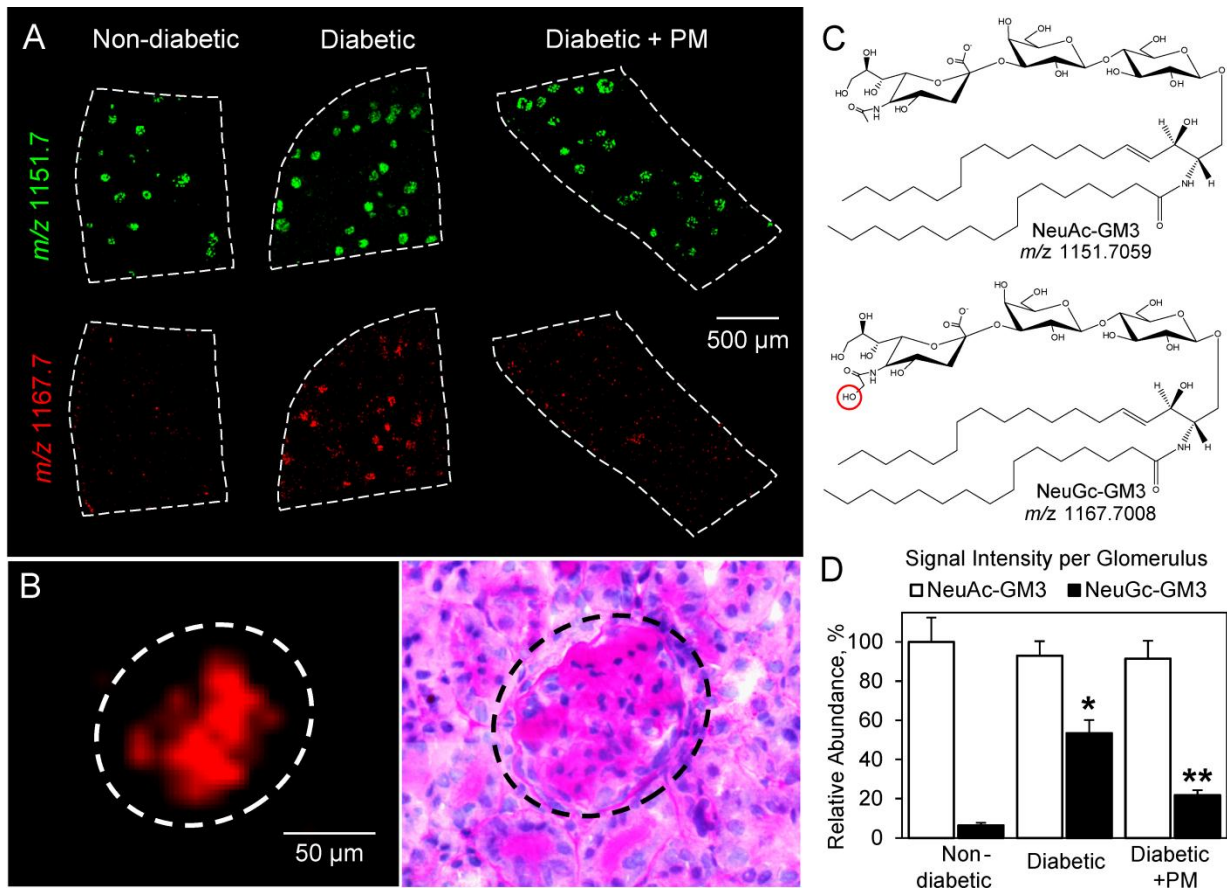


Figure 3.3. Gangliosides NeuAc-GM3 and NeuGc-GM3 show distinct changes in diabetic glomeruli. (A) MALDI TOF IMS ion images of *m/z* 1151.7 (NeuAc-GM3) and *m/z* 1167.7 (NeuGc-GM3) in kidneys from non-diabetic control mice, diabetic mice, and diabetic mice treated with PM. MALDI IMS was performed at 10 μ m spatial resolution and compared with PAS staining of the same section to confirm localization to glomeruli. (B) IMS of the signal at *m/z* 1167.7 and corresponding PAS staining showing the specific localization of NeuGc-GM3 to glomerulus. (C) Structures of gangliosides corresponding to the signals at *m/z* 1151.7 and *m/z* 1167.7 as identified using FTICR MS. The bar graph (D) represents Mean \pm SEM for three biological replicates per group analyzing 200 glomeruli total. The average signal per glomerulus was determined in ImageJ and data were normalized to non-diabetic NeuAc-GM3. * - $p < 0.05$, diabetic vs. non-diabetic groups; ** - $p < 0.05$, diabetic vs. diabetic + PM groups.

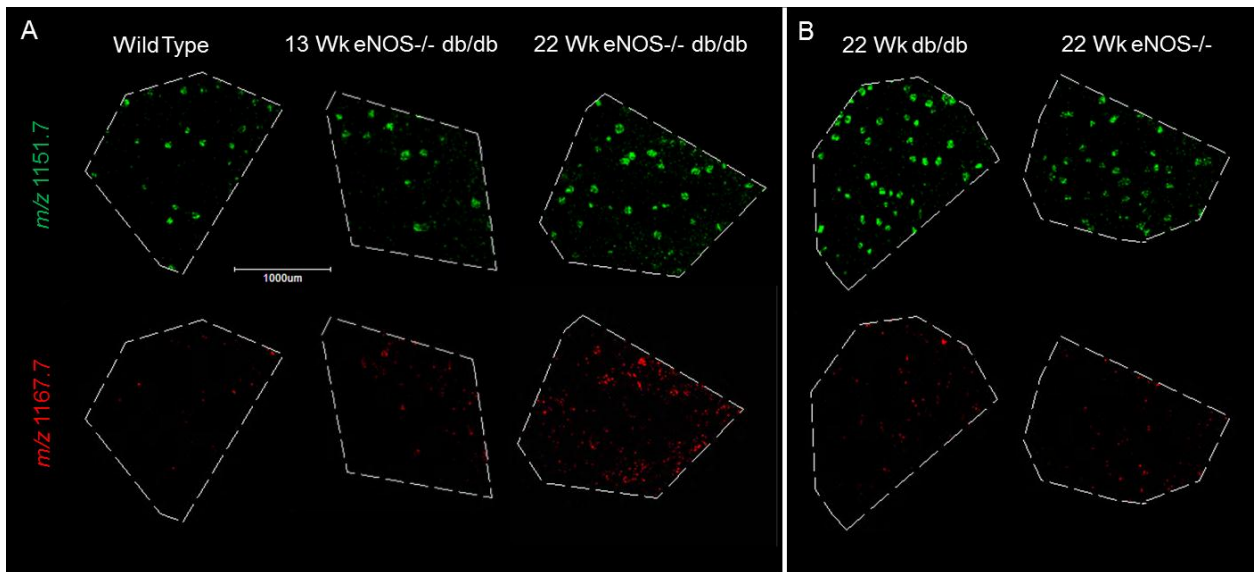


Figure 3.4. Gangliosides NeuAc-GM3 and NeuGc-GM3 in different mouse models. NeuAc-GM3 (m/z 1151.7) and NeuGc-GM3 (m/z 1167.7) were determined in kidneys of 13 and 22 week old eNOS^{-/-} db/db mice (A), and in 22 week old db/db and eNOS^{-/-} mice (B). Imaging was performed using MALDI TOF MS at 15 μm spatial resolution in the cortex region of the kidney.

identified several species of sulfoglycolipids localized specifically to mouse renal tubules: SM4s (sulfogalactoceramide), SM3 (sulfolactoceramide), SM2a (gangliotriosylceramide sulfate), and SB1a (gangliotetraosylceramide-bis-sulfate) and their different acyl chain derivatives (Table 3.1 and Figure 3.5). There was a significant increase in the levels of sulfoglycolipid species SB1a in diabetic kidneys from 22 wk old *eNOS^{-/-} db/db* mice compared to controls (Figure 3.6A and B). This increase was ameliorated in diabetic mice treated with PM (Figure 3.6A and B). Levels of SB1a showed an intermediate increase in 13 wk old *eNOS^{-/-} db/db* and in 22 wk old *db/db* mice; the levels did not increase in non-diabetic *eNOS^{-/-}* mice (Figure 3.7). In contrast to SB1a, levels of SM3, a less polar species that possesses a relatively short sugar chain, remained unchanged in the DN model (22 wk old *eNOS^{-/-} db/db* mice) compared to control (Figure 3.6A and B). Tubular localization of both sulfoglycolipids was confirmed by comparing the 10 μ m spatial resolution IMS data to a PAS stained image of the same section (Figure 3.6C). Similarly, level of SM4s, another sulfoglycolipid with a short sugar chain, was also unchanged in diabetic tubules compared to controls. Interestingly, SM3 and SM4s had very distinct non-overlapping tubular localization patterns (Figure 3.8).

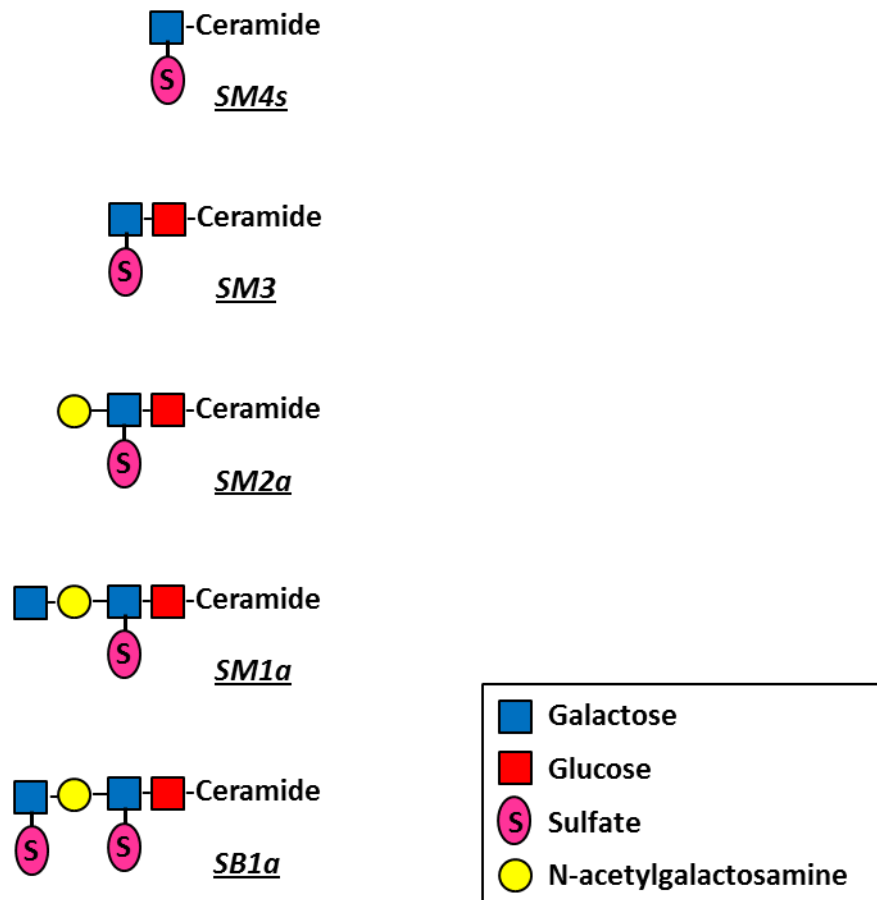


Figure 3.5. Structures of sulfoglycolipids.

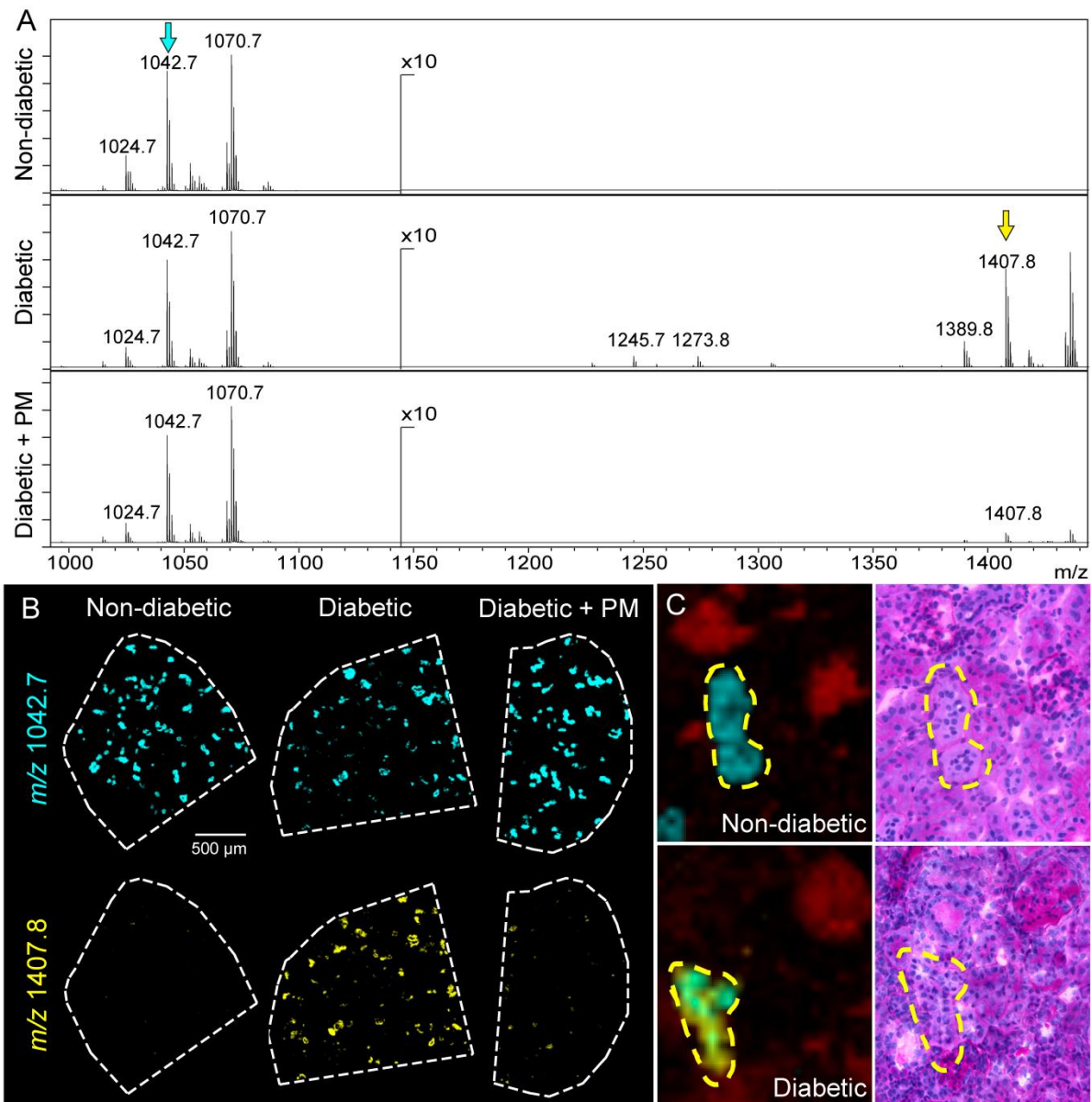


Figure 3.6. Levels of long-chain series sulfoglycolipids are increased within diabetic renal tubules. (A) Spectral region containing sulfoglycosphingolipids from tubular regions of non-diabetic, diabetic, and diabetic + PM kidneys. (B) Sulfoglycolipid SM3(t18:0/22:0), m/z 1042.7 (cyan), was common to the renal tubules and has similar levels in all the treatment groups. Sulfoglycolipid SB1a(t18:0/22:0), m/z 1407.8 (yellow), was increased in the tubules of the diabetic kidney and reduced upon PM treatment. These ion signals are marked with an arrow of corresponding color in panel A. (C) IMS overlay of the m/z 1042.7 (cyan) and m/z 1407.8 (yellow) ion signals displayed in panel B. An ion in red specifically localized to the glomeruli is shown for reference (left panels) and the corresponding PAS stained sections are shown in the right panels. Imaging performed using MALDI TOF MS at 10 μ m spatial resolution.

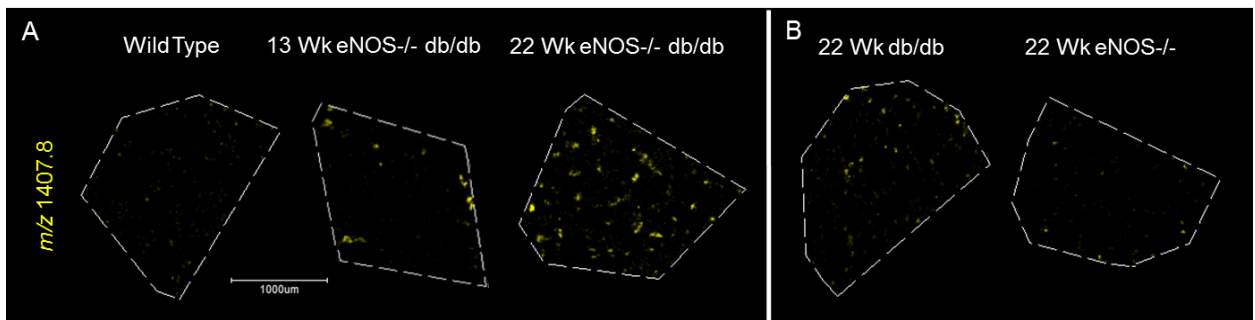


Figure 3.7. Long-chain series sulfoglycolipids in kidneys of different mouse models. Sulfoglycolipid SB1a(t18:0/22:0), m/z 1407.8 (yellow) were determined in the tubules of 13 and 22 week old eNOS^{-/-} *db/db* mice (A), and in 22 week old *db/db* and eNOS^{-/-} mice (B). Imaging was performed using MALDI TOF MS at 15 μ m spatial resolution in the cortex region of the kidney.

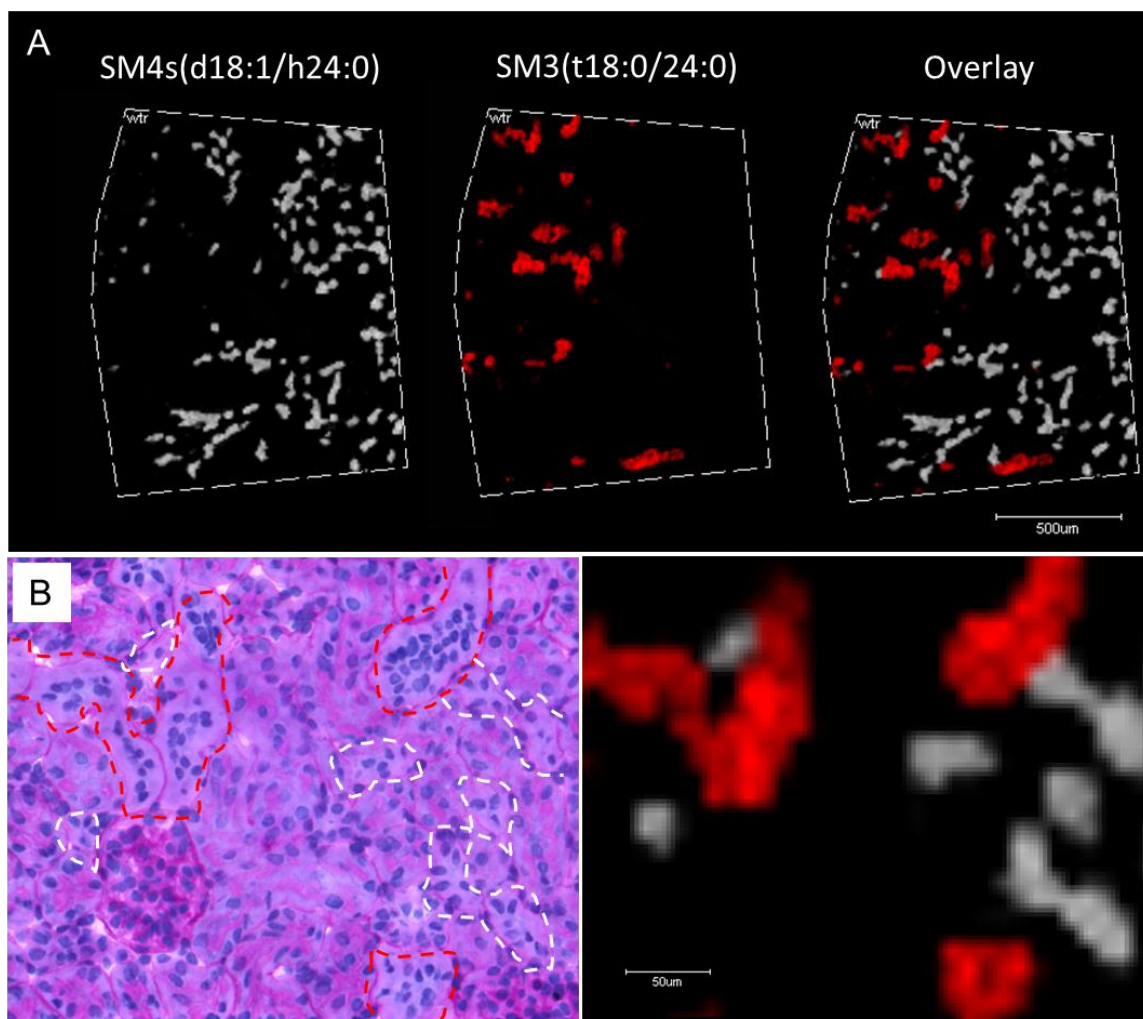


Figure 3.8. Tubular localizations patterns of sulfoglycolipids SM3 and SM4s. (A) MALDI IMS ion images of SM4s and SM3 localization in the cortex region of the kidney. SM4s(d18:1/h24:0) at m/z 906.6 and SM3(t18:0/24:0) at m/z 1070.7 are shown and are representative of other SM4s and SM3 localization. MALDI TOF IMS was performed at 10 μm spatial resolution. Scale bar = 500 μm . (B) PAS stain of the section analyzed with IMS and zoom-in of overlay from panel A to show specific tubular localization. Scale bar = 50 μm .

Major bioactive lysophospholipids are elevated in renal glomeruli in DN.

Bioactive lysophospholipids (LPLs) are important signaling and regulatory molecules involved in multiple pathogenic pathways including inflammation and fibrosis, key features of kidney disease.^{119, 120} However, renal LPL levels in DN have not been reported. We have detected LPL species comprising two major classes, lysophosphatidylcholine (LPC) and lysophosphatidic acid (LPA), in the mouse renal glomeruli (Table 3.1). The levels of both LPL classes were significantly increased in glomeruli of diabetic mice (Figure 3.9). Moreover, LPC levels were most prominently increased within those individual glomeruli exhibiting higher levels of fibrosis as determined by PAS staining (Figure 3.10) and were proportional to the degree of renal pathology in different mouse models (Figure 3.11). Levels were significantly diminished in diabetic mice treated with PM (Figure 3.9B-D). Other LPL classes such as lysophosphatidylserine, lysophosphatidylglycerol, and lysophosphatidylethanolamine were not detected in our study, possibly due to the sensitivity limits as their reported physiological levels in mouse plasma are 2-to-3 orders of magnitude lower compared to major LPLs.¹²⁰

Non-enzymatic modification of phosphatidylethanolamine by glucose is increased in the cortex of the DN kidney. Non-enzymatic adduction of glucose to aminophospholipids has been shown to increase in diabetic human plasma and animal tissues including kidney.^{121, 122} However, with the exception of diabetic atherosclerotic lesions,¹²³ the role of glycated lipids in diabetic complications has not been investigated.

We utilized MALDI IMS to analyze glycation of different phosphatidylethanolamine (PE) species in the kidney of a mouse model of DN. The

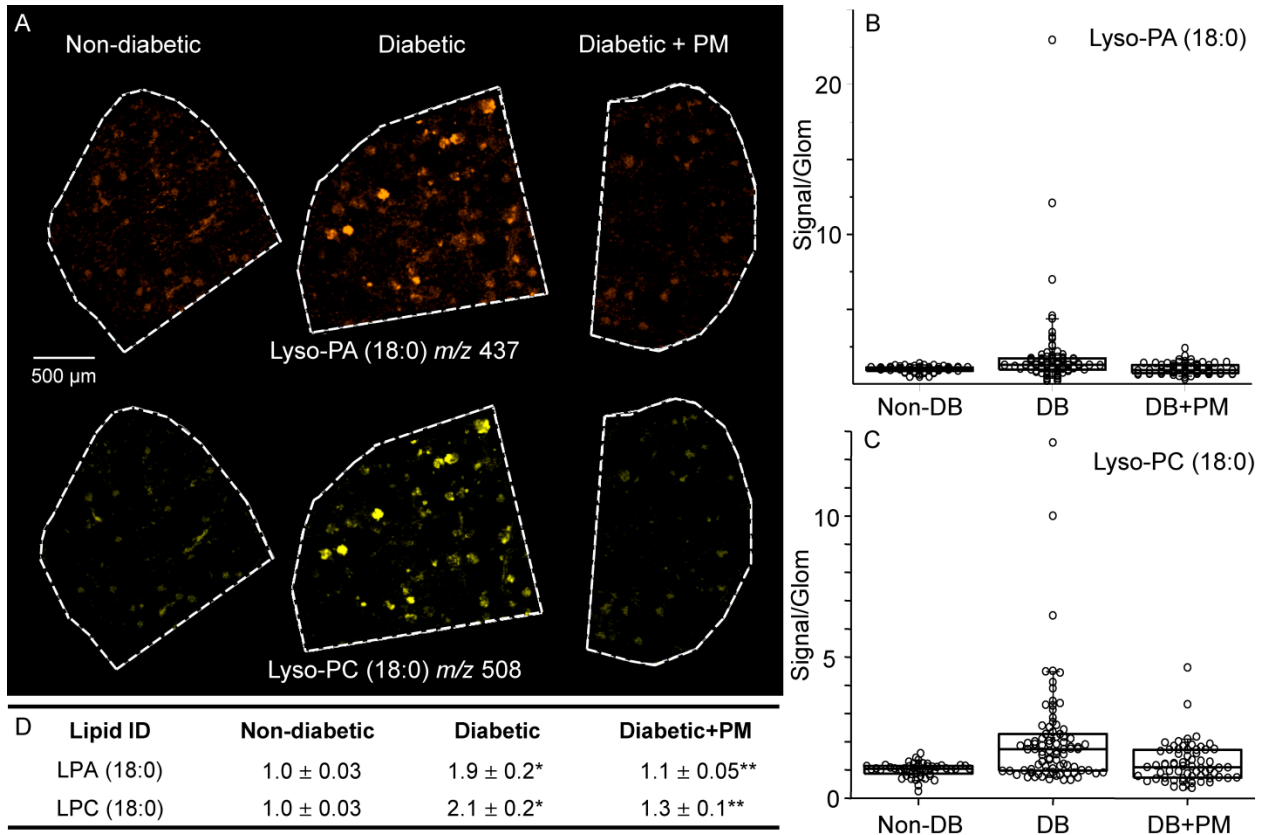


Figure 3.9. Levels of lysophosphatidic acid (LPA) and lysophosphatidylcholine (LPC) increase in the glomeruli of diabetic kidneys. (A) MALDI TOF IMS images showing glomerular localization and levels for representative LPA and LPC species (LPA 18:0) and (LPC 18:0). Distribution of LPA (B) and LPC (C) levels within individual glomeruli and summary statistical analyses (D). Data are normalized to non-diabetic LPL signal intensity. Each circle in the box plots represents the averaged intensity measurement from a single glomerulus as determined in ImageJ. * - $p < 0.05$, diabetic vs. non-diabetic groups; ** - $p < 0.05$, diabetic vs. diabetic + PM groups.

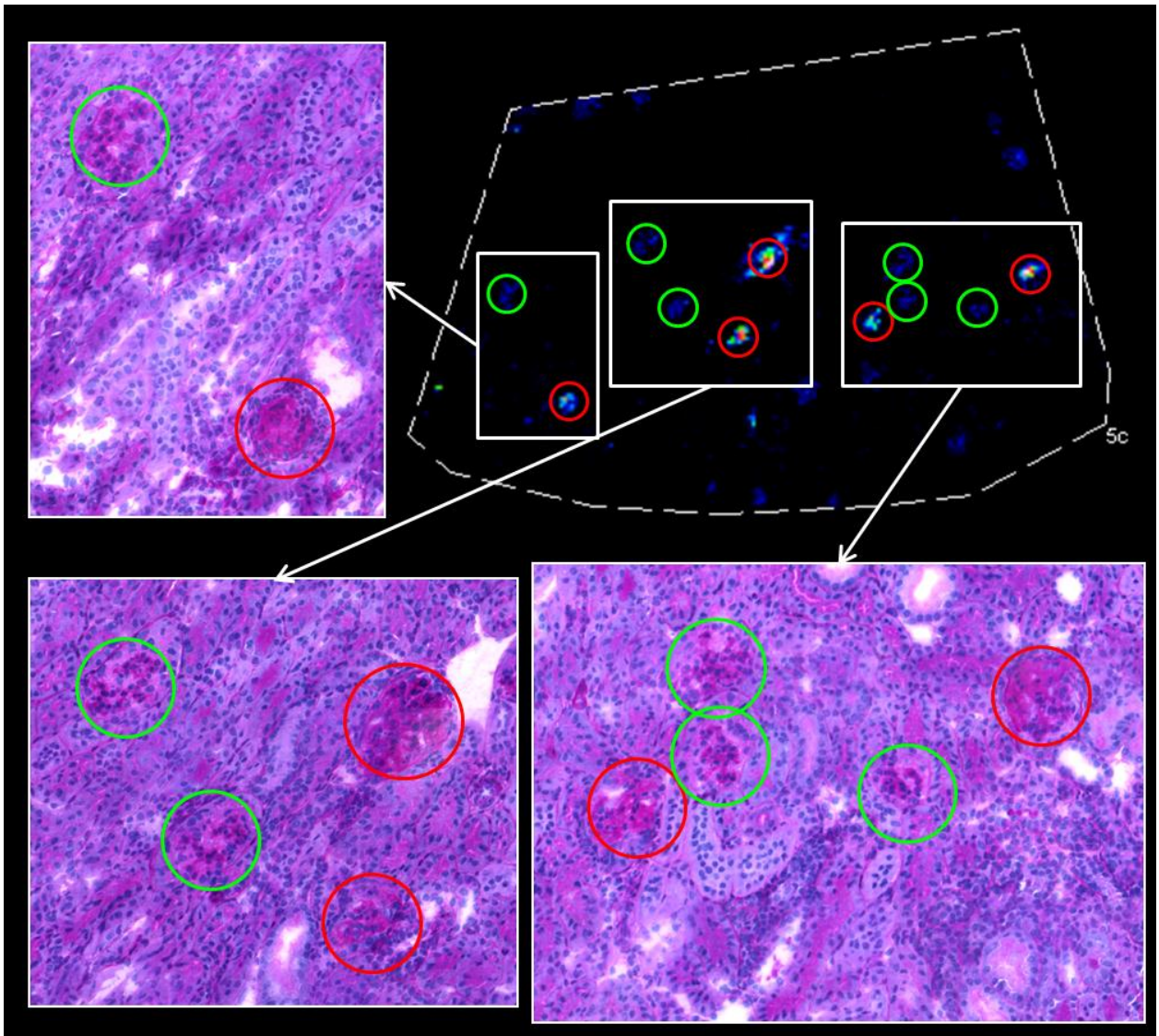


Figure 3.10. Comparison between the levels of LPC and degree of fibrosis within individual renal glomeruli. Upper right: Ion image of lysophosphatidylcholine (LPC (18:0)) in diabetic kidney. PAS stain of the same section used for IMS showing increased signal in more fibrotic glomeruli (red circles) compared to less fibrotic glomeruli (green circles).

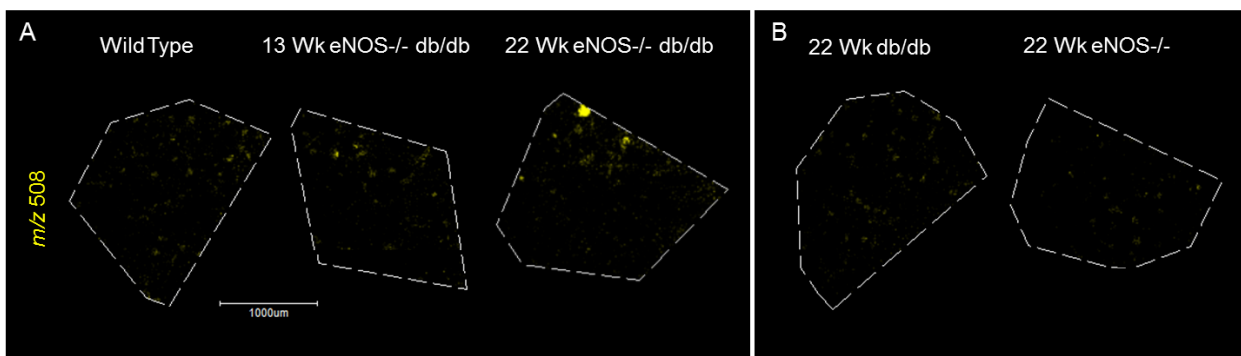


Figure 3.11. MALDI IMS of lysophosphatidylcholine (LPC) in kidneys of different mouse models. The signal at m/z 508 (LPC 18:0) was measured in glomeruli of 13 and 22 week old eNOS^{-/-} db/db mice (A), and in 22 week old db/db and eNOS^{-/-} mice (B). Imaging was performed at 15 µm spatial resolution in the cortex region of the kidney.

identities of PE species and their glucose modification (Amadori adduct) were determined in renal tissue sections using characteristic fragmentation patterns generated by tandem MS (Figure 3.12B). Unmodified PE species as well as unmodified plasmalogen PE species, characterized by the presence of a vinyl ether bond at the sn-1 position,¹²⁴ did not significantly change in diabetes compared to controls (Figure 3.12A).

Several Amadori-PE species, containing glucose adducted to the lipid amino group, were identified in the diabetic kidneys but were not detected in the non-diabetic kidneys (Table 3.1, Table 3.2, and Figure 3.12A, and Figure 3.13). MALDI IMS of transverse sections through the kidney showed that these signals were present in the cortex of the kidney. Treatment of diabetic mice with PM, did not significantly affect Amadori-PE levels (Figure 3.12 and Table 3.2), however, a tendency toward lower levels was observed in renal specimens from PM-treated mice (Table 3.2). Again, examining different time points and mouse models, the levels of Amadori-PEs seemed to correlate with the degree of renal pathology (Figure 3.13).

To determine more precise localization patterns of Amadori-PE species within the renal cortex, a region of the cortex in the diabetic kidney was imaged at high spatial resolution with a 10 μm step size (Figure 3.14). First, we found that PE lipids were not uniformly distributed throughout the cortex but had uniquely localized patterns. Further, we established that the unmodified and the Amadori forms of the same lipid species co-localize to the same areas of the cortex. This can be seen in Figure 3.14A where PE (P-18:0/20:4) and Amadori-PE (P-18:0/20:4) show the same localization pattern. Additionally, we determined that the majority of Amadori-PE species follow two major localization patterns in the renal cortex exemplified by the complementary patterns of

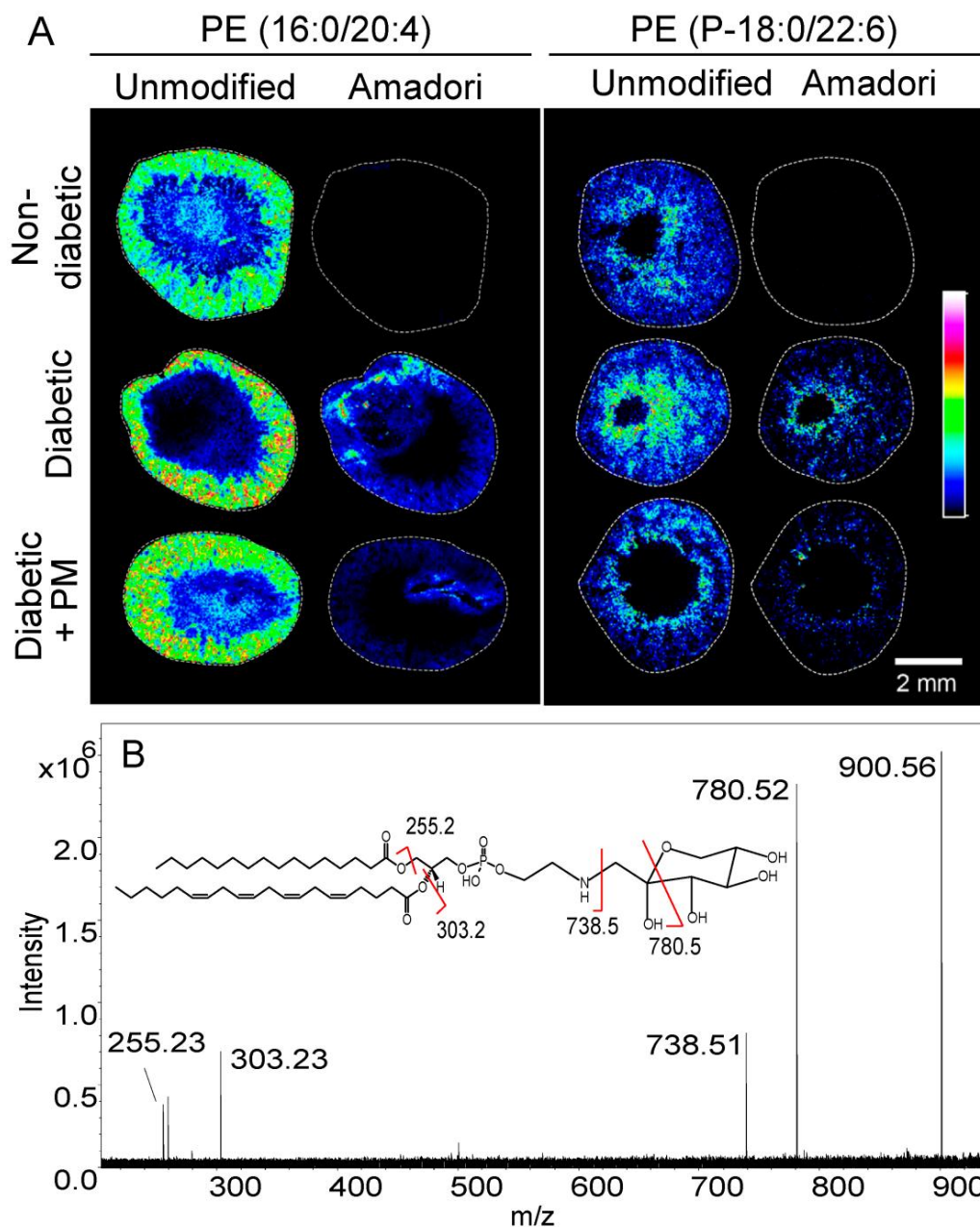


Figure 3.12. Analysis of glucose-modified (Amadori) phosphatidylethanolamine (PEs) species in non-diabetic, diabetic, and diabetic + PM mouse kidneys. (A) FTICR IMS at $40\ \mu\text{m}$ of transverse kidney sections showing localization and relative abundance of two different PE lipids along with their corresponding Amadori species. These glucose-modified species were detected in the cortex of the diabetic kidneys but not in non-diabetic kidneys. The colors represent relative signal intensity according to the scale bar on the right. (B) Identification of lipid species using Amadori-PE (16:0/20:4) as an example. The FTICR MS/MS spectrum with Amadori-PE (16:0/20:4) molecular ion (m/z 900.56), product ions and product ion assignments (inset) are shown.

Ratio of Amadori-PE to PE, %

<i>Treatment</i>	<i>PE (16:0/20:4)</i>	<i>PE (16:0/22:6)</i>	<i>PE (P-18:0/20:4)</i>	<i>PE (P-18:0/22:6)</i>
Control	0.4 ± 0.4	0.3 ± 0.3	0.2 ± 0.1	0.3 ± 0.2
Diabetic	23.2 ± 9.4*	18.9 ± 6.8*	17.5 ± 8.9*	16.1 ± 5.7*
Diabetic + PM	8.5 ± 2.5	7.4 ± 2.5	6.1 ± 1.8	7.8 ± 2.3

Table 3.2. Relative quantitation of Amadori-PE levels within renal cortex. Ratio of integrated Amadori-PE signal to unmodified PE signal from kidney imaging experiments.
* - p < 0.05, diabetic vs. non-diabetic groups.

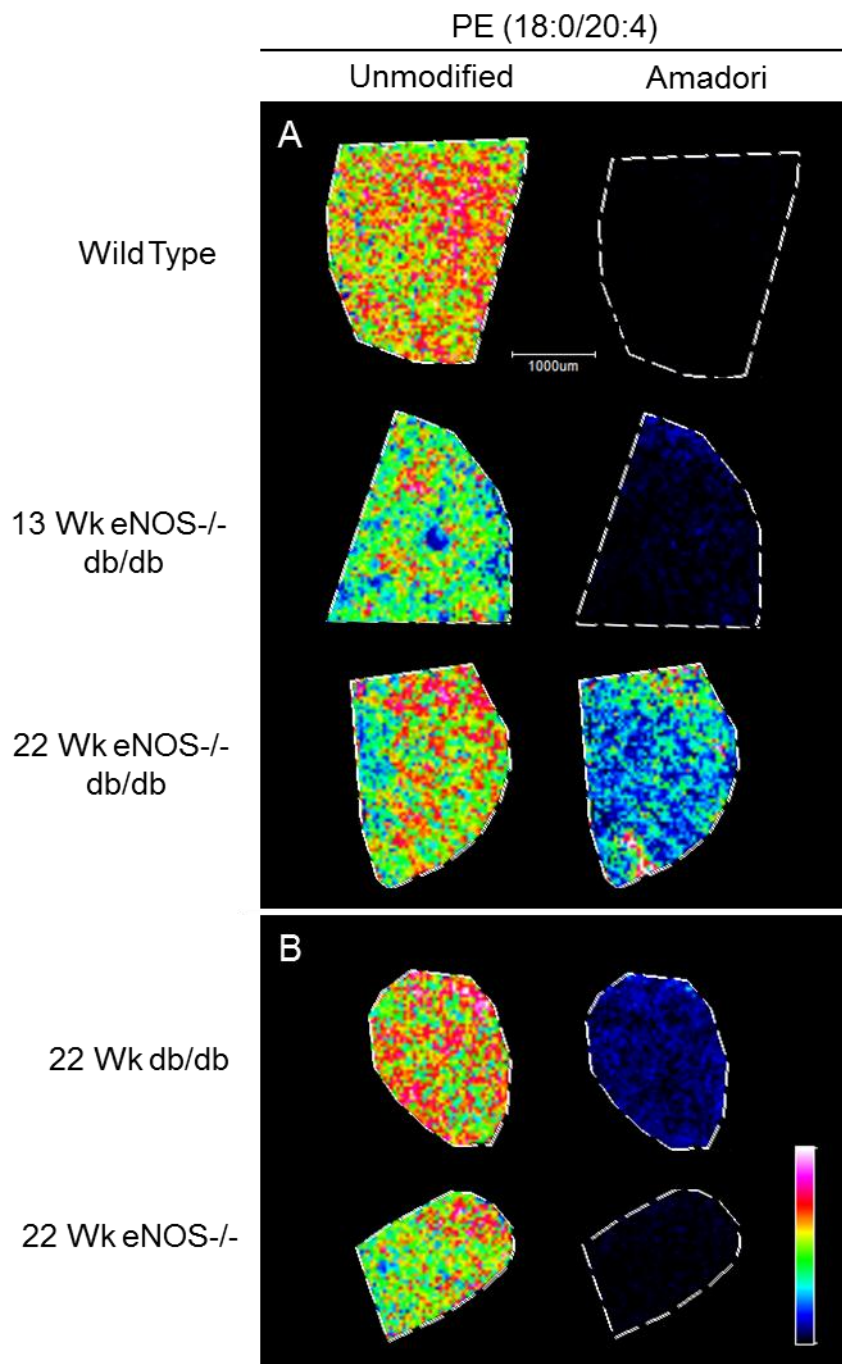


Figure 3.13. Analysis of glucose-modified (Amadori) phosphatidylethanolamine (PE) species in kidneys of different mouse models. Glucose-modified PE was determined in 13 and 22 week old eNOS^{-/-} db/db mice (A), and in 22 week old db/db and eNOS^{-/-} mice (B). Imaging was performed using FTICR MS at 40 µm spatial resolution in the cortex region of the kidney.

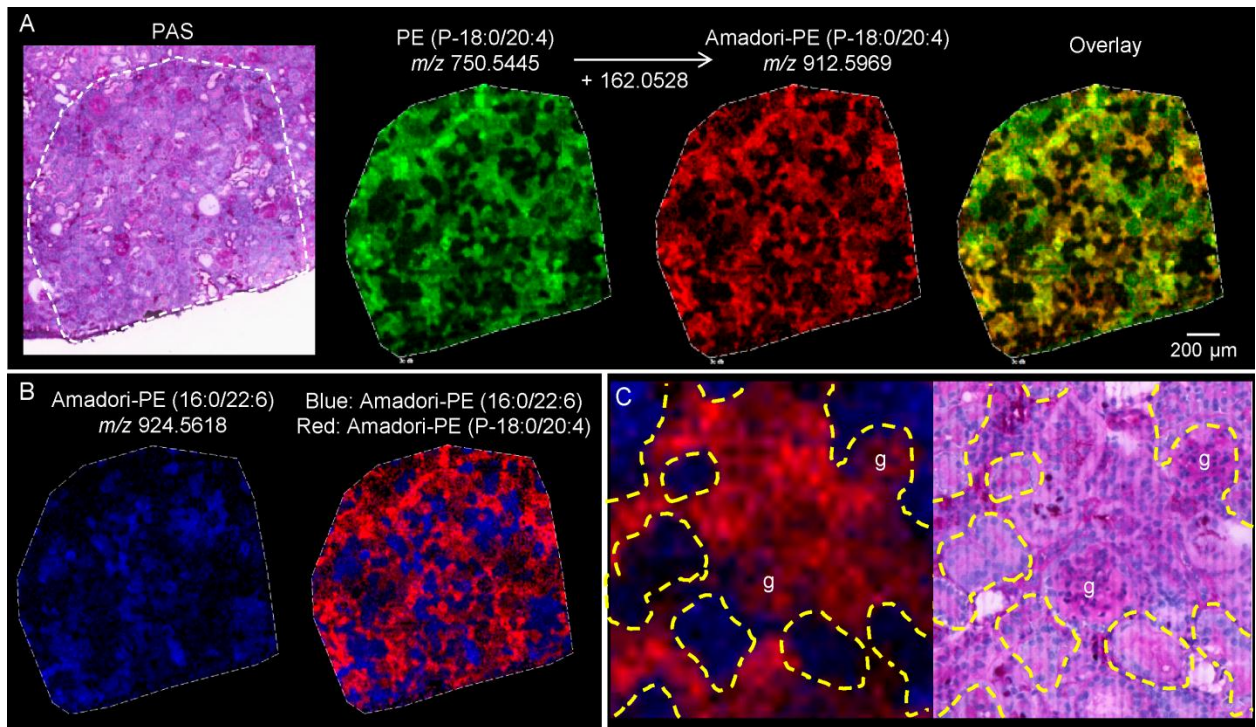


Figure 3.14. High spatial resolution (10 μm) MALDI FTICR IMS of glycosylated phosphatidylethanolamines (PEs). (A) Unmodified PEs and corresponding Amadori-PEs are co-localized to the same areas of the cortex. As an example, an overlay of PE (P-18:0/20:4) (green) and Amadori-PE (P-18:0/20:4) (red) shows co-localization in yellow. (B) Two distinct spatial localization patterns of glycosylated PE species in the renal cortex. Amadori-PE (16:0/22:6) (blue) displays the opposite localization pattern to Amadori-PE (P-18:0/20:4) (red, shown as a single ion image in panel A). (C) Zoom in on the IMS overlay from panel B (left) and corresponding region of the same section after staining with PAS (right). Amadori-PE (P-18:0/20:4) (red) is localized to glomeruli and some tubules while Amadori-PE (16:0/22:6) (blue) is localized to a distinct set of tubules. g = glomerulus

Amadori-PE (16:0/22:6) and plasmalogen Amadori-PE (P-18:0/20:4) (Figure 3.14B). The former is localized exclusively to a distinct set of tubules while the latter has a mixed glomerular and tubular localization (Figure 3.14C).

Discussion

Progress in science and medicine is closely associated with development of new experimental technologies that allow investigations to answer previously intractable questions concerning biological differences in normal and diseased tissue. The recent development of MALDI IMS technology enables molecular profiling of specific areas of the tissues while preserving tissue morphology. As demonstrated in this study, it is now possible to analyze the molecular composition and molecular modifications in distinct renal tissue regions and even within smaller structures, such as glomeruli and tubules. With the expected further improvement of spatial resolution ($<1 \mu\text{m}$), specific structural features within the glomerulus such as mesangium, GBM and even individual glomerular cells could be targeted for analysis.

Here, we utilized MALDI IMS technology to determine DN-related changes of molecular species from four major lipid classes in renal cortex, including individual glomeruli and tubules, determined directly from thin kidney sections. We employed a mouse model of DN known to exhibit severe renal damage¹²⁵ which was also observed in our study (Figure 3.1 and 3.2). Additionally, PM treatment was utilized in one experimental group which showed a reduction in albuminuria (Figure 3.1). This is consistent with the observed protective effects of PM on renal function demonstrated in several diabetic animal models^{24, 26, 28, 126} and in clinical trials, particularly at the early stages of the disease.^{25, 127}

Previous studies reported changes in ganglioside levels and metabolism in diabetic animal models.¹²⁸⁻¹³⁰ However, this is the first report on specific glomerular localization and levels of major gangliosides in DN. Of particular interest is the observed dramatic increase in the levels of NeuGc-GM3 in diabetic glomeruli (Figure 3.3). As sialic acids are synthesized via a branch of the glycolytic pathway, the increased flux through this pathway in diabetes may contribute to such increase. However, since sialic acid NeuAc is a precursor of NeuGc and ganglioside NeuAc-GM3 did not increase in diabetes (Figure 3.3A, top row) this mechanism is unlikely. Alternatively, NeuGc-GM3 may derive via non-enzymatic hydroxylation of the acetyl moiety of NeuAc-GM3 by hydroxyl radicals produced in diabetic oxidative stress.^{131, 132} This mechanism is consistent with decreased NeuGc-GM3 levels in the glomeruli of diabetic mice treated with PM, which has been shown to scavenge hydroxyl radical under high glucose conditions.^{20, 21} Interestingly, unlike in all other mammals, ganglioside NeuGc-GM3 is not metabolically produced in humans and is present only at trace levels in normal human tissues, most likely due to dietary sources.¹³³ However, NeuGc-GM3 is significantly increased in many human tumors where it may act as xeno-autoantigen causing chronic inflammation.¹³³ Therefore, it is possible that diabetic oxidative stress facilitates oxidation of NeuAc-GM3 and accumulation of NeuGc-GM3 in glomeruli, thus contributing to chronic inflammation in DN.

Our results suggest that sulfoglycolipids may play a role in DN pathogenesis. The exact mechanism remains to be elucidated. However, it is interesting that isolated rat renal tubules exposed to exogenous glucose *in vitro* showed increases in the levels of SM2a and SB1a but not SM3 sulfoglycolipids,¹³⁴ similar to our results in DN mouse

model (Figure 3.6). Experiments using cerebroside sulfotransferase (CST) knock-out mice, which do not synthesize sulfoglycolipids, have demonstrated significant reduction in monocyte infiltration of renal interstitium after ureteral obstruction in the knock-out compared to the wild-type mice. These studies suggested that sulfoglycolipids may promote renal inflammation and tubulointerstitial injury, possibly via ligation of L-selectin.¹³⁵

It is well established that lysophospholipids (LPLs) are important signaling and regulatory molecules involved in multiple pathogenic pathways.^{119, 120} LPL species may regulate cell signaling through altering the structure and fluidity of a lipid bilayer, particularly above their critical micelle concentration (CMC).¹²⁰ In this regard, the significant increase in glomerular LPL demonstrated in our study may facilitate CMC transition, thus affecting activities of membrane proteins.^{136, 137} However, most of the biological effects of LPL are mediated via G-protein coupled receptors. Particularly interesting is pro-fibrotic activity of lysophosphatidic acid (LPA) mediated via LPA1 receptor as has been demonstrated in UUO mouse model of renal fibrosis.¹³⁸ More recently, the receptor for advanced glycation end products (RAGE) has been shown to mediate pro-inflammatory action of LPA.¹³⁹ Since expression of RAGE is upregulated in diabetic kidney,¹⁴⁰ LPA-RAGE interaction may contribute to inflammatory damage in DN. Involvement of lysophosphatidylcholine (LPC) in renal pathology is indirectly suggested by the elevated LPC levels in plasma of patients with renal disease.^{141, 142} In the *in vitro* studies, LPC induced proliferation of cultured mesangial cells via a mechanism involving activation of EGF receptor signaling.¹⁴³ LPC is also a ligand for two G-protein coupled receptors G2A and GPR4, which are expressed in many human

tissues including kidney.^{144, 145} It is yet unknown whether these receptors are involved in pathogenesis of renal disease.

While prior studies have shown the elevated levels of Amadori-PEs in plasma of diabetic patients and in different organs of diabetic animal models,^{121, 122} ours is the first report establishing a relationship between glycated PEs and DN. Glycated PEs have been shown to alter the structure and stability of cell membrane proteins and promote lipid peroxidation,^{123, 146} thus exhibiting pathogenic potential. Our results suggest that Amadori-PEs play a minor role in DN pathogenesis. The levels of different Amadori-PE species in renal cortex were significantly elevated in diabetes but were not significantly inhibited upon PM treatment, even though a tendency toward lower levels was observed (Table 3.2). The notion that non-oxidative glucose adduction to PE has low pathogenicity is consistent with the previous findings using mice deficient in fructosamine-3-kinase (FN3K), the enzyme that facilitates dissociation of Amadori adducts to amino groups. These mice did not exhibit a pathogenic phenotype in any organs, including kidney, despite having significantly elevated levels of Amadori-modified tissue proteins.¹⁴⁷

In summary, our data demonstrate that the levels of specific phospho- and glycolipids in glomeruli and/or tubules of the kidney are associated with diabetic renal pathology. These lipid changes were detected in tubules and glomeruli, major sites of DN lesions and corresponded with the level of renal damage in the time course studies as well as in the models with different extent of renal damage. Through the use of PM, we also demonstrated that the inhibition of non-enzymatic oxidative pathways ameliorated lipid levels and renal pathology, suggesting that hyperglycemia-induced oxidative

pathways are required for the observed changes of lipid profiles in DN. The propensity to these oxidative pathways may contribute to individual susceptibility to DN in diabetes.

Methods

Animal studies. Animal experiments were performed at the AAALAC-accredited animal facilities at Vanderbilt University Medical Center according to institutional guidelines and IACUC-approved experimental protocol. Mice were housed in a pathogen-free barrier facility and given standard chow (Lab Diet 5015; PMI Nutrition International, Richmond, IN) and water ad libitum. Upon development of hyperglycemia (about 6 wks of age), eNOS^{-/-} C57BLKS *db/db* mice were randomized according to body weight and assigned to either diabetic or diabetic/PM treatment groups. Mice in diabetic/PM treatment group received PM in drinking water at a daily dose of 400 mg/kg body weight, based on previously published reports of PM protection from kidney injury in diabetic mice.²⁶ To minimize possible chemical degradation of PM, a light-sensitive compound, fresh solutions were prepared twice a week and administered in water bottles wrapped in aluminum foil as previously described.¹⁴⁸ PM treatment continued until mice were sacrificed at 22 wks of age. The control group included wild type C57BLKS mice. Kidneys were removed and either fixed for histological analyses by light and electron microscopy or flash frozen in liquid nitrogen and stored at -80°C for IMS analyses.

Determination of blood glucose and urinary albumin excretion. Glucose levels were measured in blood collected from the tail vein using OneTouch glucometer and Ultra test strips (LifeScan, Milpitas, CA) as previously described.^{106, 149} Albumin and creatinine excretion was determined in spot urine collected from individually caged mice using Albuwell-M kits (Exocell Inc, Philadelphia, PA) as previously described.^{106, 149}

Histological Analyses. Renal histology was assessed in mice at 22 weeks of age. The kidneys were removed and fixed overnight in 10% formalin at 4°C, and 3- μ m-thick sections were stained with periodic acid-Schiff (PAS) and Jones' silver staining. Histological evaluation by light microscopy was performed without knowledge of the identity of the various groups. A semi-quantitative index was used to evaluate the degree of glomerular mesangial expansion and sclerosis. Each glomerulus on a single section was graded from 0 to 3, where 0 represents no lesion, and 1, 2, and 3 represent mesangial matrix expansion or sclerosis, involving < 25, 25 to 50, and > 50% of the glomerular tuft area, respectively.

For electron microscopy, kidneys were cut into small tissue blocks (1 mm³) and fixed in 2.5% glutaraldehyde fixative with 0.1 mol/L cacodylate buffer, pH 7.4, overnight at 4°C. After postfixation with 1% osmium tetroxide, tissues were dehydrated in a series of graded ethanol preparations and embedded in epoxy resin (Poly/Bed 812 Embedding Media; Polysciences, Warrington, PA). Ultrathin sections were stained with uranyl acetate and lead citrate. Sections were observed by transmission electron microscopy (H-7000; Hitachi, Tokyo, Japan) at 75 kV to determine TBM and GBM thickness.

MALDI mass spectrometry. MALDI TOF Lipid Imaging: Frozen kidneys were sectioned on a cryostat at 8 μ m thickness, thaw mounted on conductive indium tin oxide coated glass slides, and dried in a desiccator. The tissue sections were washed by dipping the slide in 50 mM ammonium formate at 4°C three times for five seconds each to remove salts and increase the sensitivity for lipid analysis.⁷⁶ MALDI matrix was applied using a custom built sublimation apparatus which uses reduced pressure and heat for vapor deposition of the MALDI matrix on to the sample slide⁶¹ resulting in a uniform

MALDI matrix coating over the tissue. 1,5-Diaminonaphthalene (DAN) was sublimed at 110°C and 50 mTorr for 7 minutes. The resulting matrix coating contained 0.13 ± 0.02 mg DAN/cm². MALDI imaging experiments were performed in negative ion mode using a Bruker Ultraflextreme time-of-flight (TOF) mass spectrometer in reflectron geometry. Spectra were collected in the range of m/z 400-1500 with 10 shots/spectra. Raster steps were taken in 10 μm stage increments and the laser spot size was also 10 μm in diameter as measured on a thin matrix coating. Each imaging experiment was run as a set containing a kidney section from each experimental group. Areas of the cortex were selected for imaging of approximately 20,000 pixels per kidney. FlexImaging was used for image visualization.

MALDI FTICR Lipid Imaging: Frozen kidneys were sectioned as above. 9-aminoacridine (9-AA) MALDI matrix was applied by sublimation at 140°C and 50 mTorr for 12 minutes. The resulting matrix coating contained 1.1 ± 0.2 mg 9-AA/cm². MALDI imaging experiments were performed in negative ion mode using a 9.4 T SolariX MALDI Fourier transform ion cyclotron resonance (FTICR) mass spectrometer (Bruker Daltonics). Spectra were collected in the range of m/z of 400-1500 with 500 shots/spectra. Image resolution was set at 40 μm or 10 μm . FlexImaging and DataAnalysis were used for image visualization and data analysis.

After all imaging experiments, the MALDI matrix was removed from the slides by immersion in 70% ethanol followed by 95% ethanol for 30 s each. Kidney sections were then stained with PAS and renal tissue structures were matched to MALDI IMS data via image overlay.

Lipid Identification: All lipids reported were identified using MS/MS fragmentation along with accurate mass data. Accurate masses were determined after imaging experiments by profiling an adjacent tissue section using MALDI FTICR MS. Phospholipid species were isolated and fragmented with the FTICR MS using sustained off-resonance irradiation collision-induced dissociation (SORI-CID) for identification. Glycolipid species MS/MS fragmentation experiments were performed on a MALDI-LTQ-XL hybrid linear ion trap instrument (Thermo Scientific) using pulsed q-dissociation. The LipidMaps database (lipidmaps.org) was used to search the accurate mass data. Fragmentation patterns were interpreted manually along with tools from lipidmaps.org.

Relative quantitation of lipid levels. For the MALDI imaging datasets, ImageJ software (National Institutes of Health, Bethesda, MD, USA) was used to measure the relative abundance of the lipid species of interest between experimental groups. Monochromatic TIFF images were exported from FlexImaging to ImageJ. Areas of interest were selected in each image as individual glomeruli, tubules, or the entire kidney section. Signal intensity was measured as the mean intensity per area of interest (i.e.-glomeruli, tubules, or entire kidney cross-section). Glomerular and tubular signals were evaluated as single ions and the Amadori-PEs were evaluated as the ratio of the Amadori-PE signal to the unmodified PE signal.

Statistical analysis. Data were expressed as means \pm SEM and statistical analysis was performed using Student's *t* test for unpaired samples or ANOVA followed by post-hoc Student-Newman-Keuls comparisons. For the MALDI imaging datasets, the mean and standard error were calculated for each MS peak of interest. Differences were

evaluated by the Kruskal-Wallis rank-sum test followed by post-hoc Tukey test. Differences were considered statistically significant if p values were less than 0.05.

Acknowledgements

This chapter has been adapted from research originally published in the Journal of Lipid Research. Grove, KJ, Voziyan, PA, Spraggins, JM, Wang, S, Paueksakon, P, Harris, RC, Hudson, BG, Caprioli, RM. Diabetic Nephropathy Induces Alterations in the Glomerular and Tubule Lipid Profiles. *Journal of Lipid Research*, 55: 1375-1385, 2014.¹⁵⁰ © the American Society for Biochemistry and Molecular Biology.

CHAPTER IV

HIGH SPATIAL RESOLUTION IMAGING MASS SPECTROMETRY FOR DETECTING SPATIAL DISTRIBUTIONS OF PROTEINS IN HEALTHY, DIABETIC AND DIABETIC TREATED KIDNEYS

Overview

Imaging mass-spectrometry (IMS) allows for molecular profiling of specific morphologically distinct tissue regions, such as fibrotic glomerular lesions, without disturbing the overall tissue morphology. For this study, a robust mouse model of diabetes (eNOS^{-/-} *db/db*) with and without pyridoxamine (PM) treatment was investigated with high spatial resolution IMS to investigate protein expression changes in microstructures of kidney sections. We report histology-directed analysis of individual glomeruli as well as 25 μ m MALDI IMS which revealed molecular localization at the level of single glomeruli and tubules. Differential relative abundances of a number of protein signals were found between the experimental groups. Identified markers with increased expression in DN included fibronectin, fragments of albumin and fragments alpha-1-antitrypsin (A1AT). These proteins were found to be absent or attenuated in the non-diabetic and PM treatment groups.

Introduction

While diabetic nephropathy (DN) takes years to develop, it is largely irreversible and remains a major health complication for diabetic patients. The pathogenic mechanisms underlying this disease remain unclear and so uncovering molecular events that define mechanisms of susceptibility and disease progression can improve early detection and provide potential targets for drug therapy. Proteomic technologies have been used in this vein to discover biomarkers and uncover proteins and pathways that contribute to the pathophysiology of the kidney. A number of previous proteomic studies have looked for biomarkers in the urine and blood¹⁵¹⁻¹⁵⁴ but fewer have looked in the kidney itself.^{35, 89, 155, 156} The ability to localize molecular changes in tissue, at the site of disease, may provide insight into new molecular markers and provide a better understanding of disease progression.

Here, on-tissue histology-directed profiling and high spatial resolution imaging has been used to determine protein changes in the kidney of a robust model of DN, the eNOS^{-/-} db/db mouse. The present study is the first report of direct kidney MALDI IMS for protein analysis with the spatial specificity to analyze individual renal glomeruli and tubules. Proteomic signatures that correlated with disease were identified and their localization within the kidney was determined. The relative abundance of these signatures was evaluated after treatment with PM; an experimental drug being that has been shown to slow the progression of kidney disease.^{25, 28, 127}

Results

Histology-directed profiling for protein expression in glomerular lesions.

Histology-directed MALDI IMS was utilized to analyze individual glomeruli in renal sections of wild-type mice and eNOS^{-/-} db/db mice which develop robust DN.¹⁰⁶ Glomeruli from eNOS^{-/-} db/db mice exhibited significant ECM deposition in PAS-stained sections (Figure 4.1A). Kidney sections were stained with cresyl violet, a stain that does not interfere with MALDI MS, and glomeruli were identified and selected for trypsin spotting (Figure 4.1B). After *in situ* tissue digestion, tryptic peptides from the individual glomeruli were analyzed by MALDI MS and the most abundant peptide signals were identified using tandem MS. In the MS spectrum from a single diabetic mouse glomerulus (Figure 4.1C), a peptide at m/z 1906 was identified as a tryptic fragment of fibronectin (Figure 4.1D). The fibronectin deposition was detected in glomeruli but not in non-glomerular cortical areas of the diabetic mice. In the wild-type mice, levels of fibronectin were not statistically different from the background noise (Figure 4.1E). The peaks at m/z 1363 and 2572 were also identified as fibronectin peptides and exhibited similar intensity patterns as the fibronectin tryptic peptide at m/z 1906. In addition, peaks at m/z 1529 and 1274 were identified as tryptic fragments of hemoglobin, a peak at m/z 1744 was a tryptic fragment of histone H2B, and the peak at m/z 1198 was a tryptic fragment of smooth muscle actin (Figure 4.1C).

Proteomic studies have established that protein abundance in complex biological samples is proportional to the abundance of corresponding proteolytic peptide fragments.^{157, 158} In MALDI IMS studies, the intensities of proteolytic peptide ions resulting from *in situ* trypsin digestion corresponded to the intact protein ion intensity.⁹⁶

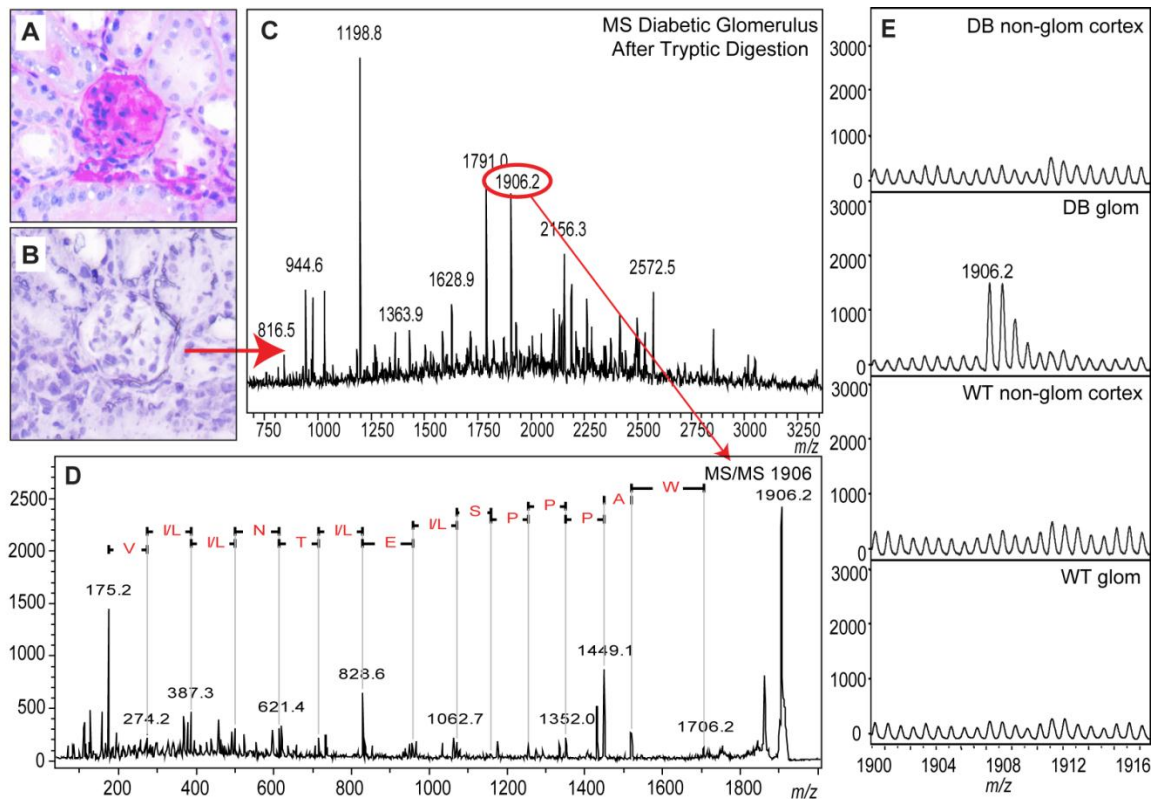


Figure 4.1. Identification of fibronectin deposition in individual glomeruli. (A) PAS stained glomerulus from $eNOS^{-/-} db/db$ kidney section exhibiting abnormal extracellular matrix deposition and sclerotic regions. (B) Cresyl violet stain of the same glomerulus shown in panel A from a serial kidney section. (C) MALDI MS spectrum of tryptic peptides from a selected glomerulus; peptide at m/z 1906 was sequenced using tandem MS mode. (D) Tandem MS (MS/MS) spectrum and corresponding amino acid sequence of the peptide at m/z 1906; the peptide was identified as a tryptic fragment of fibronectin by searching mouse SwissProt database with MASCOT software. (E) MALDI MS spectra in the region of the tryptic fibronectin peptide at m/z 1906 from glomeruli and non-glomerular cortex areas of $eNOS^{-/-} db/db$ and wild-type mice. Increases in renal fibronectin deposition occurred specifically in glomeruli of $eNOS^{-/-} db/db$ mice.

Therefore, we used the abundance of fibronectin peptide with m/z 1906 to determine relative deposition of fibronectin in different areas of the kidney and in kidney glomeruli. Ten random glomeruli from each kidney section of wild-type mice, eNOS^{-/-} *db/db* mice and PM treated eNOS^{-/-} *db/db* mice were subjected to *in situ* tryptic digestion followed by MALDI MS analysis. As shown in Figure 4.2A and B, glomerular fibronectin deposition was significantly increased in eNOS^{-/-} *db/db* mice and PM treatment reduced the amount of glomerular fibronectin deposition in eNOS^{-/-} *db/db* mice. This increase in fibronectin deposition by IMS was consistent with that determined using classical immunohistochemistry (Figure 4.3). Interestingly, there was also ~2.5-fold increase in smooth muscle actin, a well-known marker of DN,¹⁵⁹ in the eNOS^{-/-} *db/db* glomeruli compared to that of control. This increase was completely inhibited in PM treated eNOS^{-/-} *db/db* mice.

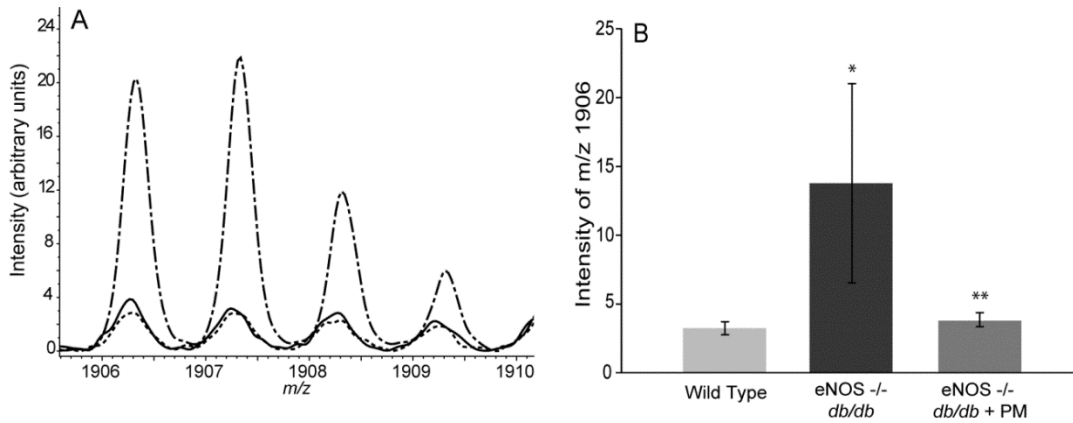


Figure 4.2. Treatment of eNOS^{-/-} db/db mice with PM inhibited glomerular fibronectin deposition. (A) MALDI MS spectra of tryptic fibronectin peptide at *m/z* 1906 were determined in glomeruli of non-diabetic wild type C57BKS mice (dotted line), eNOS^{-/-} db/db mice (dashed-and-dotted line), and eNOS^{-/-} db/db mice treated with PM (solid line). (B) The mean intensity of tryptic fibronectin peptide at *m/z* 1906. * - the difference between eNOS^{-/-} db/db and WT was significant, $P < 0.001$ (n=10); ** - the difference between eNOS^{-/-} db/db and eNOS^{-/-} db/db + PM was significant, $P < 0.001$ (n=10).

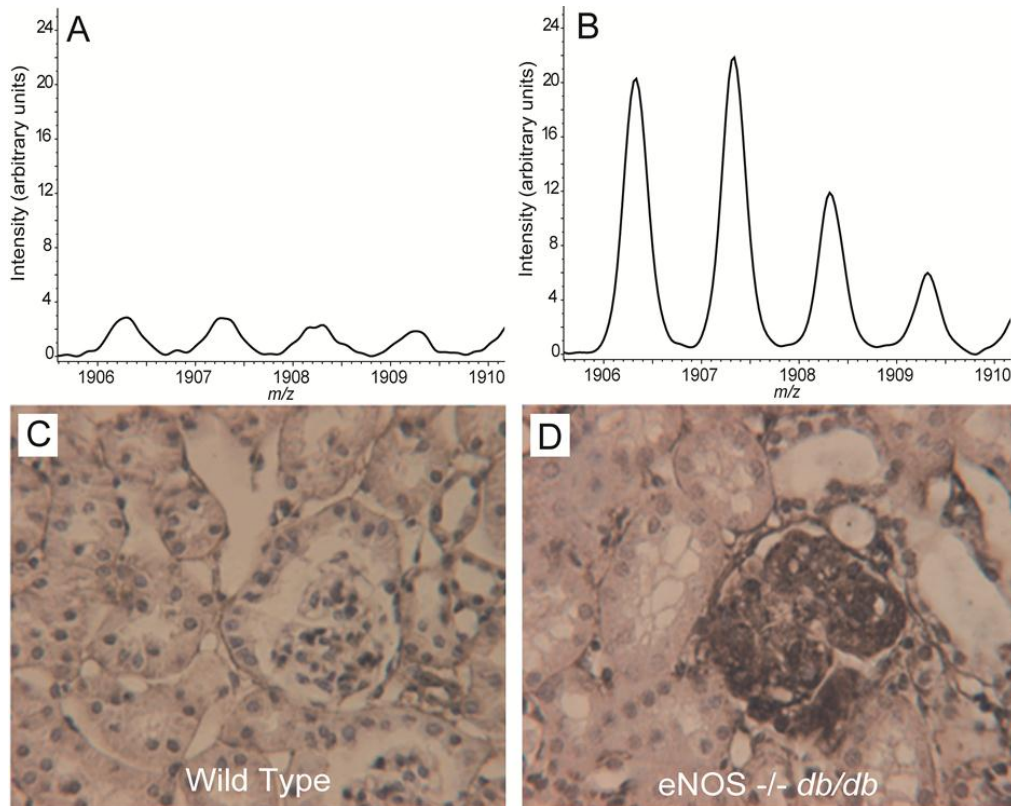


Figure 4.3. Increase in glomerular fibronectin deposition in eNOS^{-/-} db/db mice by MALDI MS and validation by IHC. MALDI MS spectra in the region of the tryptic fibronectin peptide at *m/z* 1906 from glomeruli of wild type (A) and eNOS^{-/-} db/db (B) mice. Immunohistochemical analysis of fibronectin deposition in wild type (C) and eNOS^{-/-} db/db (D) mice using fibronectin antibody.

High spatial resolution MALDI IMS reveals protein differences in specific regions of DN kidney cortex. Protocols were developed for high spatial resolution MALDI IMS protein analysis of small renal structures such as glomeruli and tubules. Kidney sections were coated with CHCA matrix by sublimation which produced a uniform coating with crystal sizes $\sim 1 \mu\text{m}$. After sublimation and deposition of the matrix on to the tissue surface, the slides were rehydrated in a humid environment which increased protein incorporation into the matrix layer. High spatial resolution imaging was performed on thin kidney sections from DN and wild type mice to determine protein expression differences between the experimental groups. Tissues were imaged at a $25 \mu\text{m}$ spatial resolution in the mass range of m/z 1000 to 25000 and then co-registered with the PAS stained histology image of the same section. At this spatial resolution, and with co-registration, features such as glomeruli could be determined in the MALDI IMS data.

Since the glomerulus is one of the structures known to be damaged in DN, we examined the protein expression differences in the glomeruli between the experimental groups. Figure 4.4 shows the average spectra from glomeruli of non-diabetic and DN kidneys. Signals such as m/z 1851, 4343, 4965, and 15600 were present in all glomeruli. Several signals were found to be increased in DN glomeruli such as m/z 3650, 4415, and 8710. The signal at m/z 4415 was particularly interesting because it has a mass difference of 72 Da from the common glomerulus signal at m/z 4343. Because a mass shift of 72 Da could represent a carboxyethyl lysine (CEL) modification, a known AGE to be increased in DN, the expression and localization of this signal was examined more closely. Additionally, we were interested in the expression of this signal in the PM treated mouse kidney, since PM is an inhibitor of AGEs. Figure 4.5A shows the localization of m/z 4343

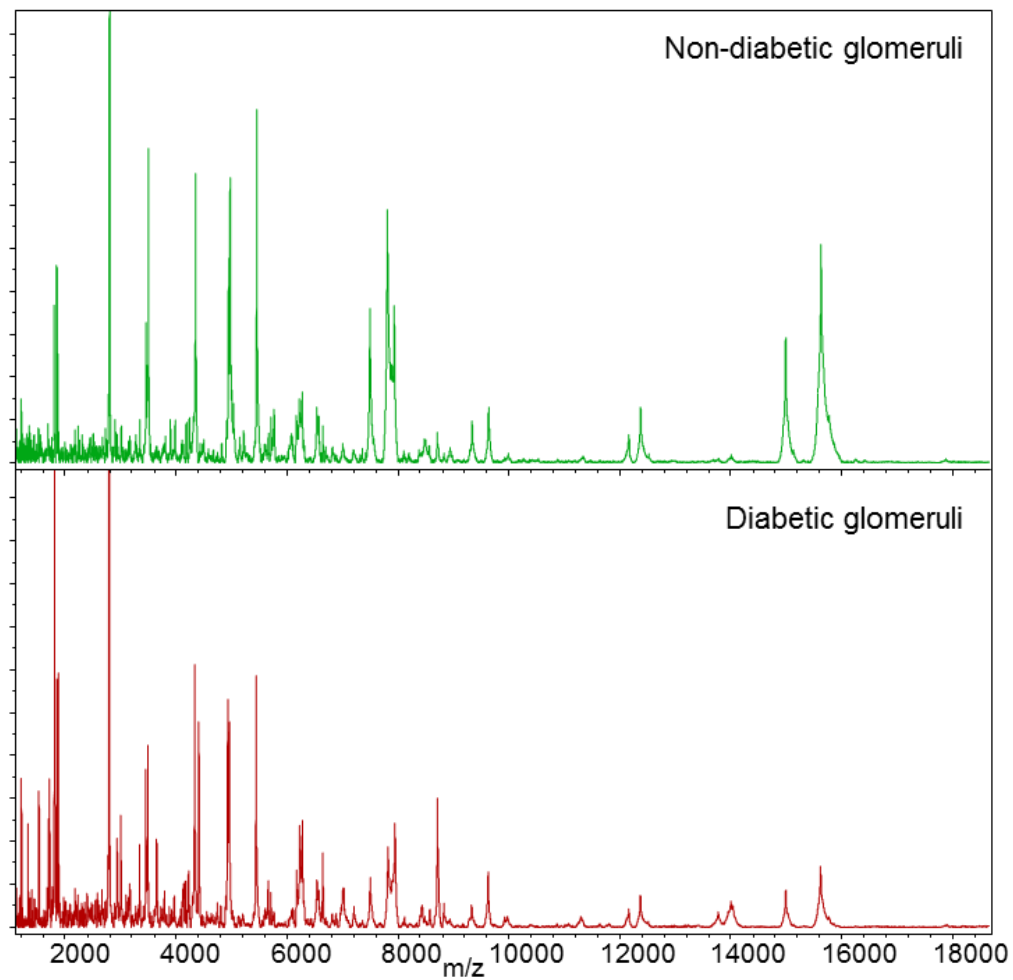


Figure 4.4. Average spectra from glomeruli in non-diabetic and diabetic mouse kidneys.

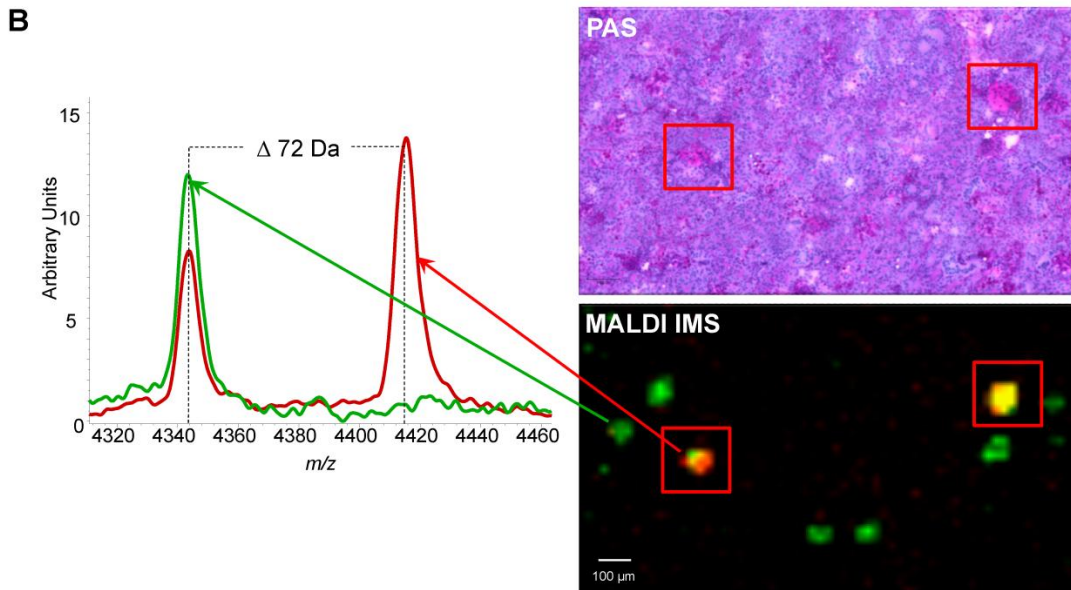
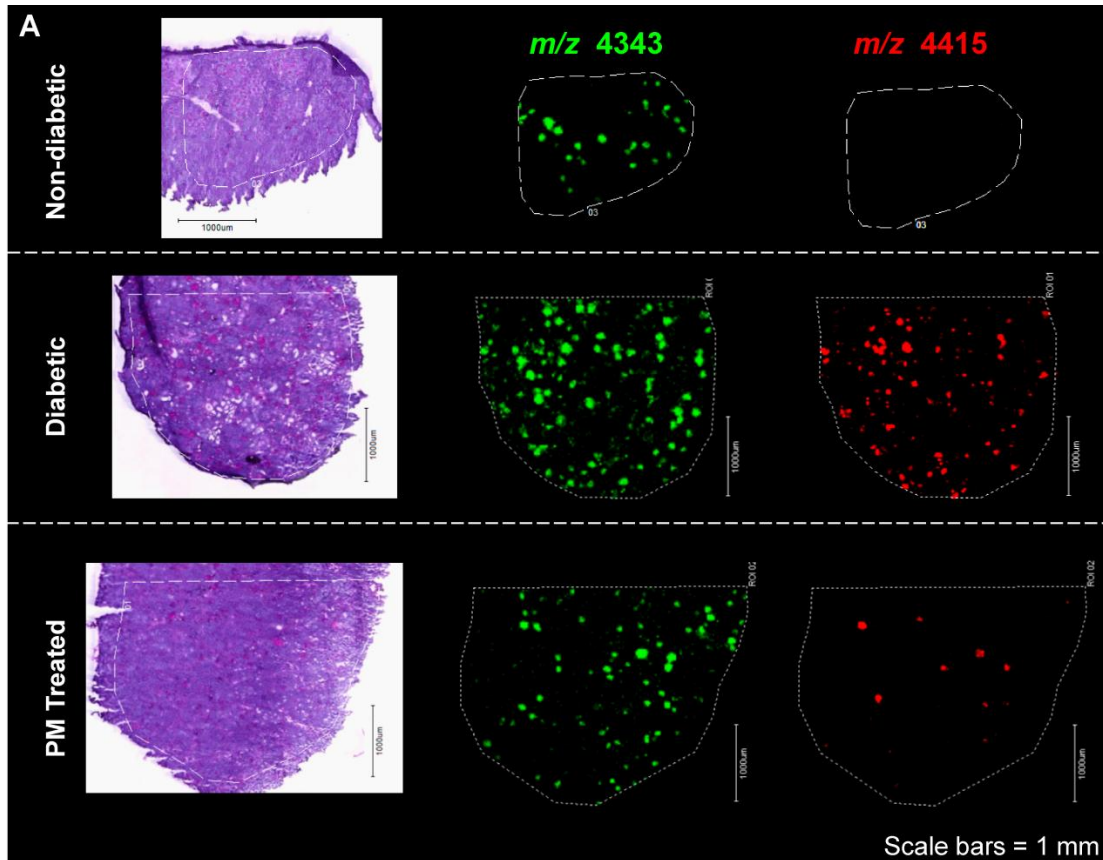


Figure 4.5. High spatial resolution IMS shows protein changes in glomeruli of diabetic kidneys. (A) MALDI IMS of kidneys imaged at 25 μm spatial resolution showed a signal at m/z 4343 localize to glomeruli of all experimental groups. A signal at m/z 4415 (+72 Da from m/z 4343), localizes specifically to the diabetic glomeruli and is absent in the non-diabetic glomeruli. (B) The signal at m/z 4415 is present in glomeruli with more intense PAS staining.

and m/z 4415 in kidneys of each experimental group. The signal at m/z 4415 was not present in the glomeruli of wild type kidneys. In the PM treated animals, this signal was lower than in the untreated counterparts. Because this signal was not completely absent in PM treated glomeruli, we wanted to more closely examine the glomeruli where this signal was localized. As seen in Figure 4.5B, this signal is present in more sclerotic glomeruli as determined by the more intense pink staining from the PAS which highlights extracellular matrix.

Beyond the differences in the glomerulus, the high spatial resolution imaging revealed a number of other signals to be differential between the wild type and DN kidneys. These signals were present in discrete regions in the DN kidney and one example is shown in Figure 4.6. It was not obvious based on histology or mass spectral patterns what the corresponding region in the wild type kidney was to compare it with. Because of this, spectra from across the tissue were extracted for further analysis. About 1,000 spectra from each a wild type cortex and a DN cortex were loaded into ClinProTools (Bruker) for peak picking. The integrated areas of 240 peaks were calculated for all individual spectra. The free statistics program Tanagra was used for further analysis of this set of peaks. PCA was performed and a plot of the first two principle components is shown in Figure 4.7A. The first principal component was able to describe the variation between the wild type spectra and the DN spectra in this dataset. Therefore, the loadings of the first component were examined to determine what peaks influenced this separation (Figure 4.7B). These peaks were examined in the imaging datasets of biological replicates and peaks which showed a consistent pattern were selected for further analysis.

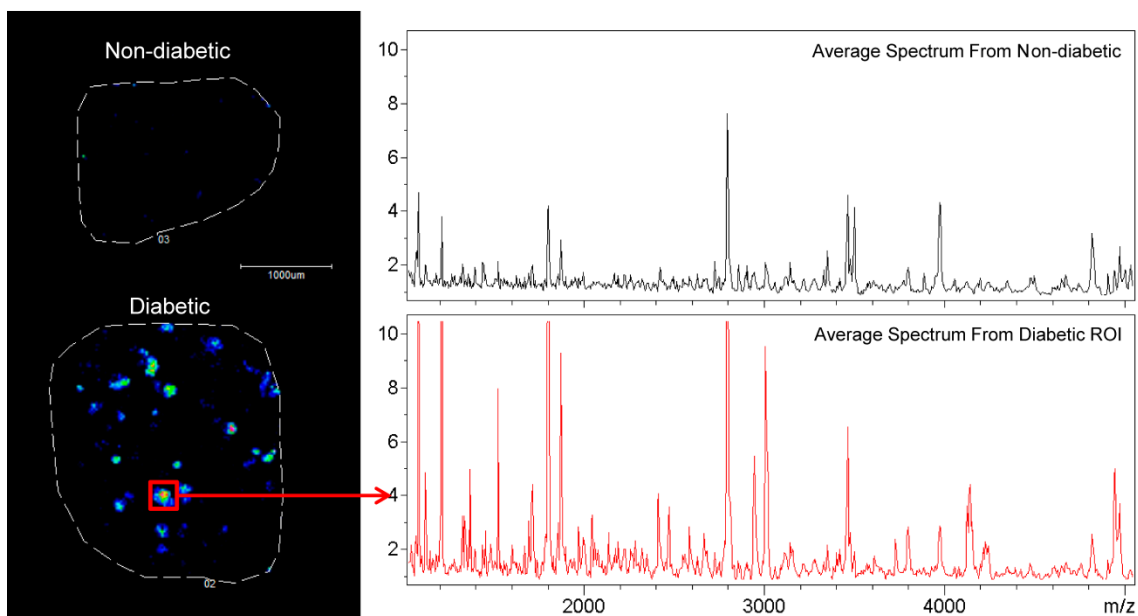


Figure 4.6 Low molecular weight species increased in diabetic kidney cortex. An example of one low molecular weight species, m/z 1903, that was not detected in the non-diabetic kidney and present in the diabetic kidney with a highly localized distribution. The top right shows the average spectrum from the non-diabetic kidney. The bottom spectrum shows the average selected spectrum from the region of interest shown to the left. There is an increase of signals in the range of 1-4.5 kDa. Imaging performed with MALDI IMS at 25 μm .

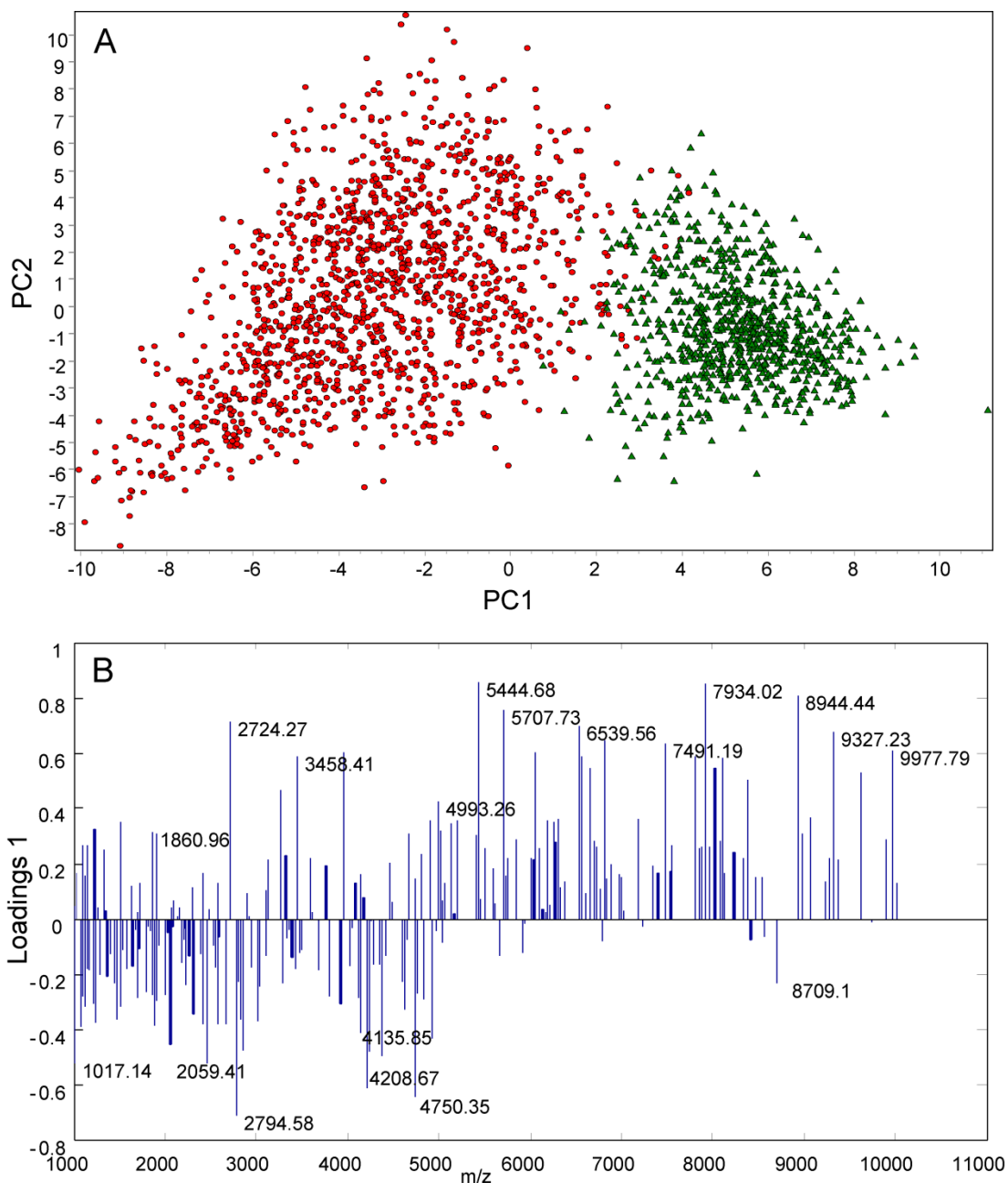


Figure 4.7. PCA based differentiation of spectra from IMS. (A) Scores plot of the first two principle components differentiating spectra from IMS of diabetic (red circles) and non-diabetic (green triangles) kidneys. (B) Plot of loadings from PC1 vs each m/z .

Identification of peaks from IMS. A number of peaks could differentiate wild type and DN kidneys; however, it is important to determine the molecular identity to investigate the biological roles. Because many of the peaks of interest were localized to small regions of the tissue, targeted approaches were necessary for identification. Two strategies were used to identify peaks of interest from the IMS experiments: image directed on-tissue MS/MS of peaks 1-3kDa and LC-MS/MS of homogenized serial sections targeting IMS signals of interest using top-down electron transfer dissociation (ETD) for fragmentation. Additionally, high mass resolution on-tissue MS was performed using a 15T FTICR MS on diabetic kidneys for accurate mass measurements to assist in identification. Table 4.1 lists proteins identified. Of particular interest were signals related to albumin and alpha-1-antitrypsin (A1AT) and these were further investigated.

Identification and localization of alpha-1-antitrypsin. Closer examination of the discriminating peaks revealed two unique sets of peaks increased in diabetic kidneys (Figure 4.8A). The three signals in each peak set showed the same localization and were each separated by 14 Da. The first peak in both sets was targeted for ETD MS/MS (Figure 4.8B) by selecting precursor ions at m/z 589.5, $[M+7H]^+_{7+}$ and m/z 601.9, $[M+7H]^+_{7+}$ which correspond to the MALDI TOF peaks at m/z 4120 and m/z 4208, respectively. These two peaks were identified as C-terminal fragments of alpha-1-antitrypsin 1-4, differing by one serine amino acid. In the mouse, alpha-1-antitrypsin (A1AT) is represented by a cluster of related genes. Based on accurate mass measurements the sets of triplicate peaks which are separated by 14 Da are most likely the same C-terminal 35 and 36 fragments of alpha-1-antitrypsin 1-2 and alpha-1-

Table 4.1. Table of identified proteins. Italicized entries are probable identifications based on FTICR MS measurements. The parentheses annotate the amino acid sequence and modifications represented by the signal.

MALDI TOF <i>m/z</i>	Clusters With	Identification	ID Method
1018	DB	Albumin (359-366)	LIFT
1108	DB	Albumin (356-363)	LIFT
1211	DB	Napsin-A (387-398)	LIFT
1237	DB	Albumin (557-567)	LIFT
1474	DB	Albumin (356-366)	LIFT
1479	DB	Albumin (557-569)	LIFT
1802	DB	Histone H2A (115-130)	LIFT
2008	DB	Transgelin (183-201)	LIFT
2042	DB	Albumin (557-574)	LIFT
2398	DB	Transgelin (179-201)	LIFT
2665	DB	Albumin (26-48)	LIFT
2794	DB	Albumin (25-48)	LIFT
4120	DB	A1AT (379-413)	ETD
4208	DB	A1AT (378-413)	ETD
4938	DB	Thymosin B10 (2-44 acetylated)	ETD
4965	DB	Thymosin B4 (8-50 acetylated)	ETD
5445	WT	<i>Cytochrome C oxidase polypeptide 7C (17-63)</i>	<i>Accurate Mass</i>
5708	WT	<i>ATP synthase subunit epsilon, mitochondrial (2-52)</i>	<i>Accurate Mass</i>
8709	DB	Apolipoprotein A-II (25-102)	Trypsin Bottom up, LIFT
8944	WT	ATP synthase-coupling factor 6, mitochondrial (33-108)	ETD
9912	WT	Acyl-CoA-binding protein (2-87 acetylated)	ETD
9978	WT	Cytochrome c oxidase subunit 6B1 (2-86, acetylated, 2 disulfide bonds)	ETD

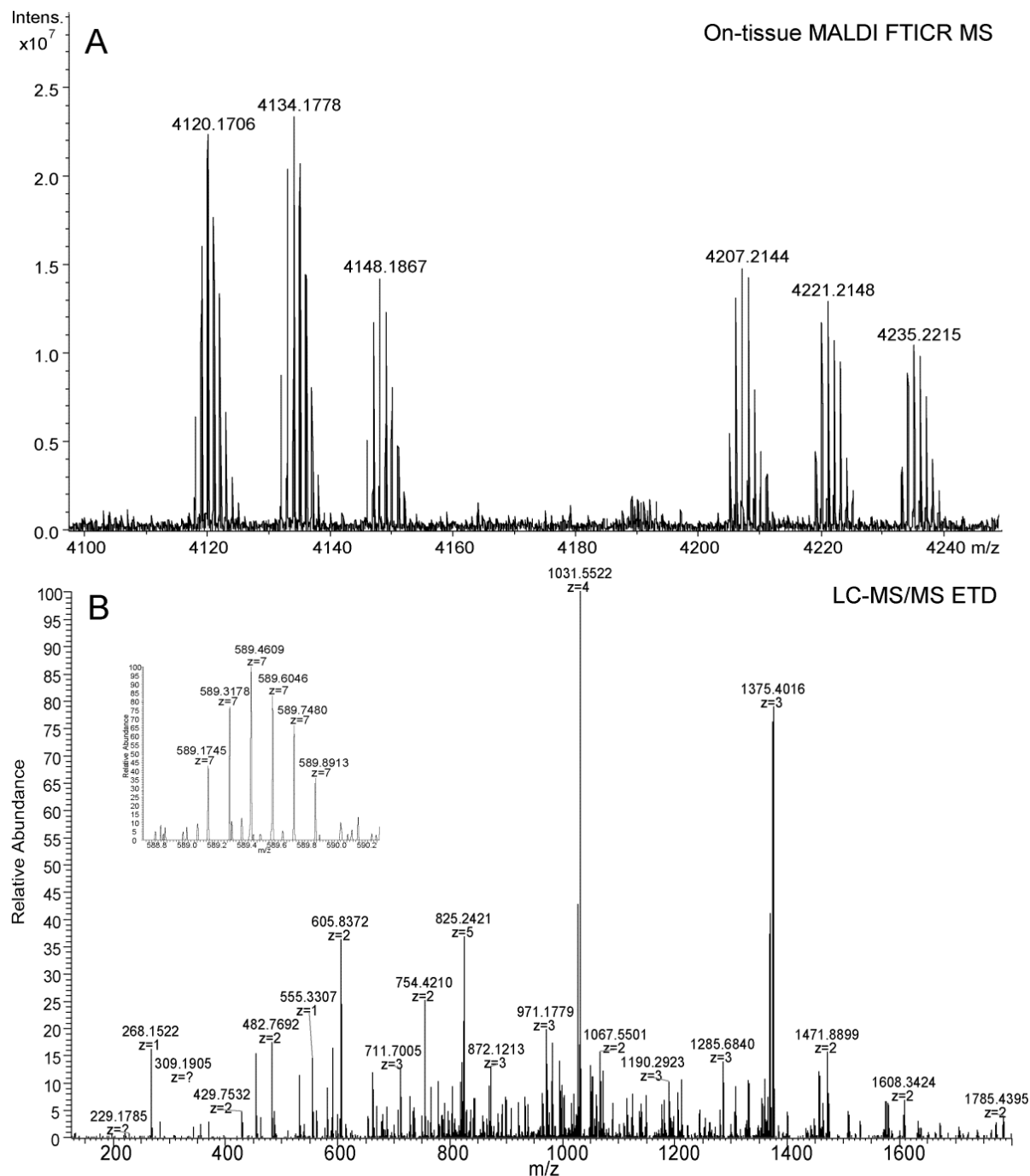


Figure 4.8. MALDI and ESI analysis of C-terminal fragments of A1AT. (A) MALDI FTICR spectrum from diabetic kidney tissue showing C-terminal A1AT fragments present in the diabetic mouse kidney. The first set of peaks represents the C-terminal 35 amino acids of three forms of A1AT while the second set of peaks represents the C-terminal 36 amino acids. (B) ETD fragmentation spectrum of m/z 589.5, $[M+7H^+]^{7+}$ (inset, corresponds with m/z 4120.17 $[M+H^+]^+$ from panel A) which was identified as the C-terminal 35 amino acids of A1AT 1-4.

antitrypsin 1-1. A1AT 1-2 differs from A1AT 1-4 by one leucine in place of one valine amino acid while A1AT 1-1 has two leucines in place of two valines from A1AT 1-4. These amino acid differences would result in mass shifts of 14 Da each. Figure 4.9 shows the spatial distribution of the C-terminal 35 amino acids at m/z 4120 along with the relative abundance of this signal in the kidney determined from three biological replicates in each group. Both the images and relative quantitation show a clear increase in this signal in the diabetic kidney and a decrease with PM treatment. Additionally, this signal appears to be more concentrated in cast regions of the diabetic cortex.

Albumin fragments in the DN kidney. On tissue MS/MS analysis revealed a number of albumin fragments were present in diabetic kidneys (Table 4.1). To further investigate this, high mass resolution IMS was performed on diabetic kidneys using a 15T FTICR MS. Mass signals were then compared to theoretical albumin fragments using the FindPept tool from ExPASy (<http://web.expasy.org/findpept>). This search returned a number of ‘hits’ that included those that already had MS/MS confirmation and additional probable albumin fragments. Interestingly, all of the possible albumin fragments originated from three main regions of the intact albumin. Table 4.2 lists identified and probable peptides detected in the DN kidneys. Several albumin fragments were selected for further analysis to determine the relative abundance of these peptides within non-diabetic, diabetic, and PM treated diabetic kidneys. These fragments had unique and localized distributions within the diabetic kidney as shown in Figure 4.10. As can be seen in the box plots in Figure 4.10, these fragments are dramatically increased in DN and further, attenuated by PM treatment.

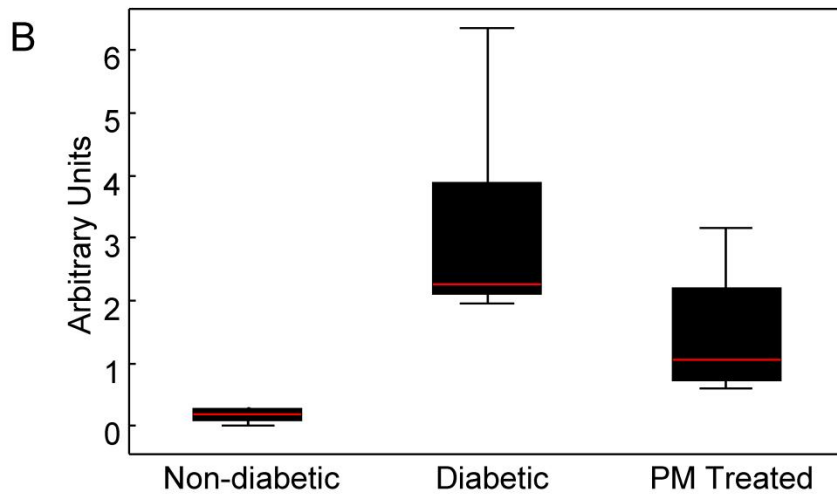
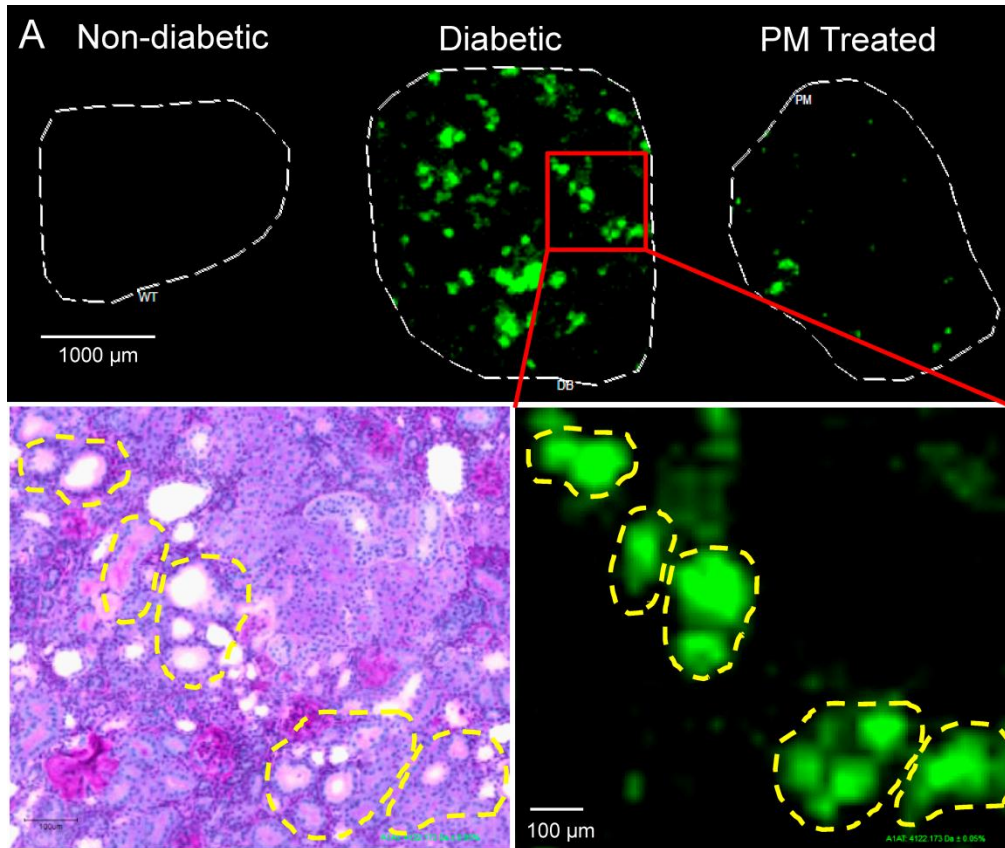


Figure 4.9. Localization and relative abundance of A1AT C-terminal fragment. (A) Representative example of m/z 4120 localization in non-diabetic, diabetic, and PM treated diabetic kidney cortex. This signal appears to be present in tubular regions of the kidney. (B) Relative abundance of m/z 4120 between experimental groups. $n = 3$ per group. Imaging performed with MALDI TOF at 25 μm spatial resolution.

Table 4.2. Albumin fragments detected in diabetic kidneys.

Measured (m/z)	Theoretical (m/z)	ppm	Sequence	Position	ID Method
2409.1690	2409.1690	0.00	(R)EAHKSEIAHRYNDLGEQHF(K)(G)	25-44	Accurate Mass
2466.1890	2466.1909	-0.77	(R)EAHKSEIAHRYNDLGEQHF(K)G(L)	25-45	Accurate Mass
2791.4270	2791.4274	-0.16	(R)EAHKSEIAHRYNDLGEQHF(K)GLVL(I)	25-48	MS/MS
2662.3841	2662.3848	-0.26	(E)AHKSEIAHRYNDLGEQHF(K)LVL(I)	26-48	MS/MS
1585.7380	1585.7394	-0.87	(F)LYEYSRRRHPDYS(V)	355-366	Accurate Mass
1107.5324	1107.5330	-0.56	(L)YEYSRRRHP(D)	356-363	MS/MS
1472.6564	1472.6553	0.72	(L)YEYSRRRHPDYS(V)	356-366	MS/MS
1222.5596	1222.5600	-0.34	(Y)EYSRRRHPDYS(S)	357-365	Accurate Mass
1093.5166	1093.5174	-0.69	(E)YSRRRHPDYS(S)	358-365	Accurate Mass
1017.4855	1017.4861	-0.59	(Y)SRRRHPDYS(V)	359-366	MS/MS
2299.2471	2299.2479	-0.31	(E)LVKHKPKATAEQLKTVMDDF(A)	556-575	Accurate Mass
1236.7062	1236.7059	0.21	(L)VKHKPKATAEQ(L)	557-567	MS/MS
1349.7903	1349.7900	0.24	(L)VKHKPKATAEQL(K)	557-568	MS/MS
1477.8854	1477.8849	0.32	(L)VKHKPKATAEQLK(T)	557-569	MS/MS
1578.9322	1578.9326	-0.23	(L)VKHKPKATAEQLK(T)(V)	557-570	MS/MS
2039.0955	2039.0954	0.05	(L)VKHKPKATAEQLKTVMDDF(F)	557-574	MS/MS
2186.1631	2186.1638	-0.34	(L)VKHKPKATAEQLKTVMDDF(A)	557-575	Accurate Mass

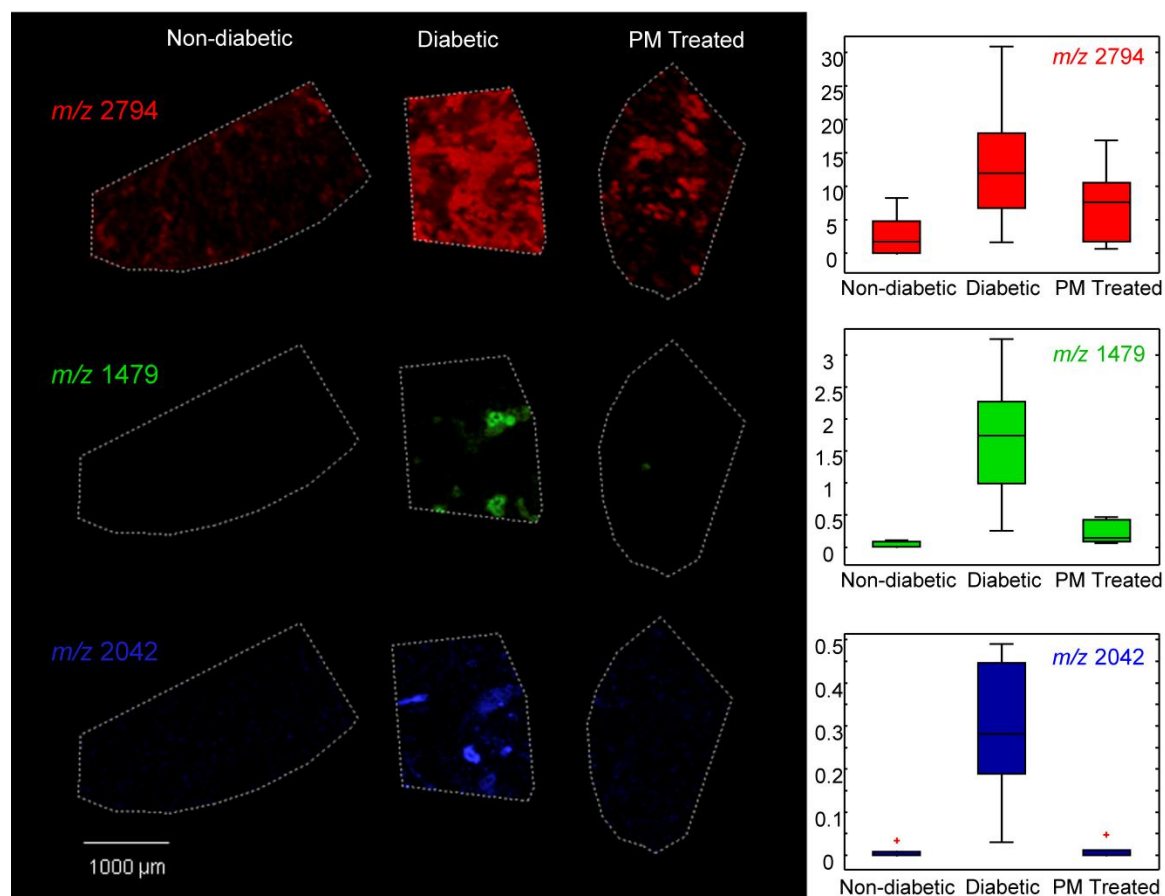


Figure 4.10. IMS and relative quantitation of albumin fragments. Imaging performed with MALDI TOF at 25 μm spatial resolution. Relative abundance determined by the average intensity per imaged region. $n=3$ per group.

Immunofluorescence staining shows tubular localization of albumin fragments. After determining the presence of albumin fragments in the DN kidney, we wanted to further determine the precise structures where these were localized. Serial sections were cut and MALDI IMS was performed on one section at a spatial resolution of 25 μm and immunofluorescence staining for tubular specific proteins was performed on the other. Two antibodies were used, one which stained proximal tubules, and another which stained distal tubules and collecting ducts. The resulting images of the immunofluorescence and IMS were co-registered. Fragments of albumin were found in these tubular structures (Figure 4.11).

Discussion

DN is characterized by structural and functional changes in glomeruli and tubular regions of the kidney cortex; however, much remains unknown about the molecular mechanisms of this disease. In this study we sought to detect and identify markers of DN at the site of disease and evaluate their response with therapeutic intervention. To do so, histology-directed profiling and high spatial resolution imaging was applied to a robust mouse model of DN to determine relative protein expression differences in pathologic lesions in microstructures of the kidney.

Protein mass signals with the specificity to single glomeruli were detected in this study. One of these was fibronectin, which through histology-directed profiling we demonstrated identification and relative quantitation. Glomerular fibronectin deposition is a prominent known feature of diabetic kidney injury.¹⁶⁰ Previous studies have shown that high glucose can increase ECM expression^{161, 162} through reactive oxygen species generation.¹⁶³ In this study, we found tryptic peptides of fibronectin increased in glomeruli of eNOS^{-/-} db/db kidneys compared to healthy kidney glomeruli.

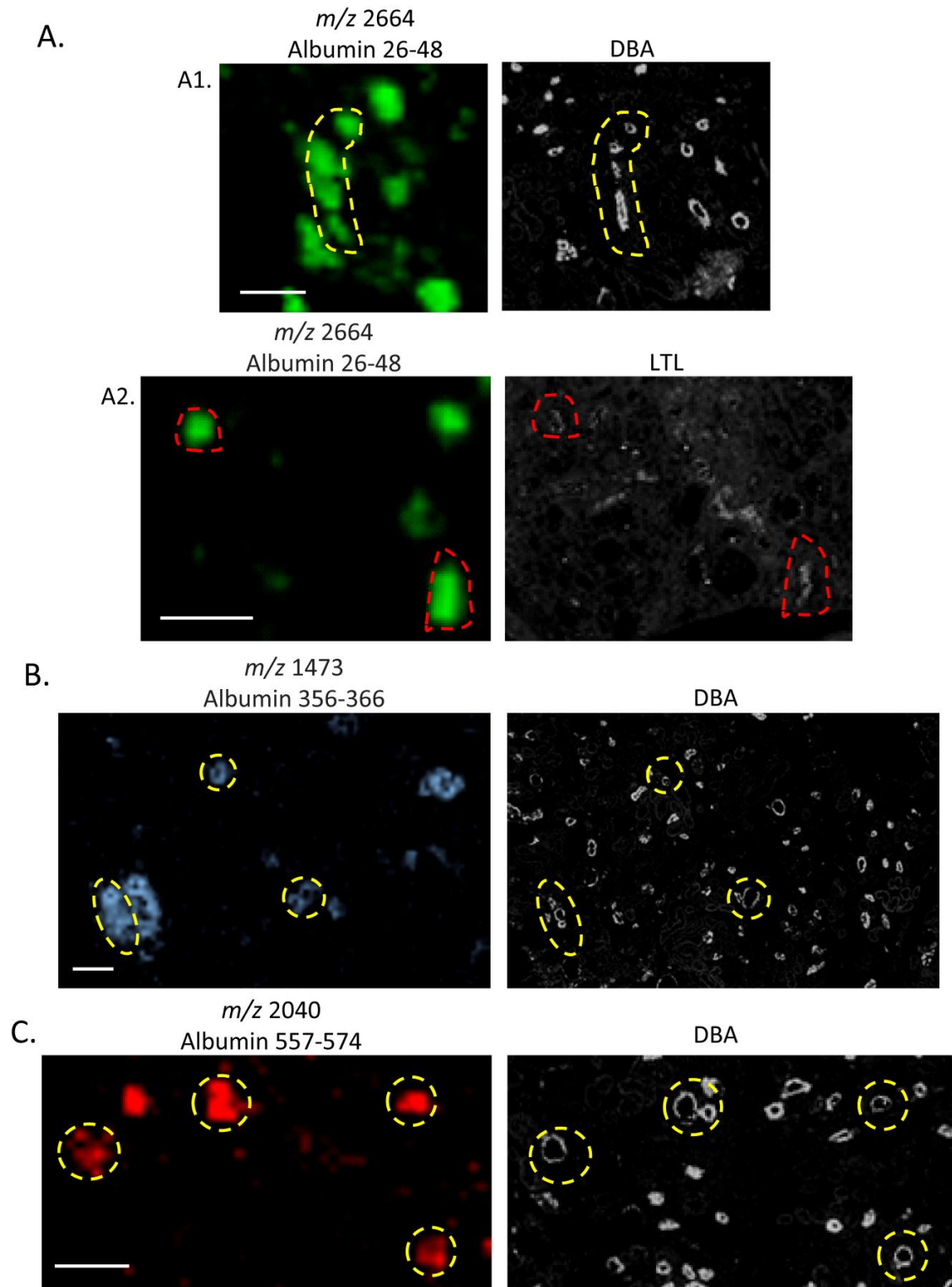


Figure 4.11. Albumin fragments localize in tubules of diabetic kidney. Albumin fragments co-localize with dolichos biflorus agglutinin (DBA), a distal tubule and collecting duct marker, and Lotus tetragonolobus lectin (LTL), a proximal tubule marker. All scale bars = 200 μ m.

We also determined that PM treatment attenuated the levels of fibronectin deposition in the eNOS^{-/-} *db/db* kidney glomeruli, suggesting that increased renal ECM deposition involves oxidative pathways.

In addition to profiling, high spatial resolution IMS of intact proteins was used to detect expression patterns in glomeruli. Signals at *m/z* 3650 and 4415 were unique to DN glomeruli and may be a marker of disease progression. It was noted that the peak at *m/z* 4415 in the DN glomeruli has a mass shift of +72 Da from a glomerular protein found in the wild type kidney. This mass shift is consistent with the AGE modification carboxyethyl lysine and its presence is reduced significantly with PM treatment, a known inhibitor of AGE modifications. In the present study, identification of this molecule was unsuccessful. Further work is needed to both identify this molecule and confirm the modification.

IMS of the kidney cortex revealed differential signals outside of the glomerulus as well. Further, many of these differential signals were identified through targeted approaches. Identification of protein peaks from IMS experiments is a challenge and a bottleneck in the IMS workflow. Two main approaches commonly used to identify signals from IMS are on-tissue fragmentation¹⁶⁴ and off-line tissue homogenization/extraction and LC separation followed by bottom-up or top-down approaches. Efficiency of on-tissue fragmentation can be limited with singly charged proteins, particularly for signals >5 kDa, and works best for abundant ions. Bottom-up approaches with LC/MS have been used to identify proteins from IMS but it can often be difficult to match intact masses from protein databases to those detected in IMS. Top-down^{70, 165, 166} MS/MS approaches are becoming more popular and useful for identification of IMS signals as the intact mass from each experiment can be directly compared. However, identification becomes even more of a challenge when signals of interest are localized to very

small tissue structures as was the case in this study. Here we used two targeted strategies for protein identification that used very little tissue. First, image-directed on-tissue MS/MS was used to identify proteins that localized to small tissue structures, where the MS/MS sampling area was guided by the IMS data on a serial section. Using this approach a number of albumin fragments were identified directly from tissue in highly localized tubule regions. In the second strategy several thin serial sections were collected and homogenized followed by a targeted LC-MS/MS run. The nearness of the sections to the one imaged helped ensure that the same signals would be present in the homogenized sample and targeting the m/z of interest increased the sensitivity of analysis versus data dependent approaches.

A1AT is an inhibitor of serine proteases. It has activity against a number of proteases but its main target is elastase, which not only breaks down elastin but other ECM proteins as well. It should be noted then that an increase in A1AT could lead to ECM accumulation. Upon interaction with a target protease, A1AT is cleaved in its reactive center loop generating a 4kDa fragment. Alternatively, non-target proteolytic cleavage has been reported in the reactive center loop as well without known inhibitory function.¹⁶⁷⁻¹⁶⁹ In this study we report two sites in the reactive center loop where A1AT is cleaved. Further studies are needed to determine the nature and function of these A1AT fragments in the DN kidney. However, in a number of other studies, both A1AT and C-terminal fragments of A1AT have been found in the urine of patients with diabetes and other forms of kidney damage^{151, 152, 170-173} indicating this protein as a potential biomarker of kidney disease.

It is well established that processing of albumin is mishandled in the diabetic kidney. Detection of albumin in the urine indicates kidney damage and is in fact the main diagnostic used to assess early disease and disease progression.^{3, 174} It was generally accepted that in healthy

kidneys only a small amount of albumin passed through the glomerular filter and then was taken up by the proximal tubules and degraded.¹⁷⁵ The albumin that was not taken up was excreted intact in the urine. While intact albumin is the main measure in the clinic, more studies are showing that albumin fragments increase as well and these are not always detected by traditional assay methods.¹⁷⁶⁻¹⁷⁸ The origin of albumin fragments is also of interest. Some studies suggest fragments are made in the urine by urine proteases.^{173, 179} While this may happen, others have found fragments present in the kidney as well.¹⁸⁰⁻¹⁸² Our data are in support of the hypothesis that albumin fragments are formed in the kidney. We have detected them in post-glomerular regions (Figure 4.11) suggesting that they may be formed during processing in the tubules. Our data are in agreement with other studies which have suggested that after lysosomal degradation in the proximal tubule, albumin fragments are returned to the lumen of the tubule to be excreted in urine. The extent of fragments found in our study also seem to correlate with disease severity as PM treatment reduced the abundance of albumin fragments detected in the kidney (Figure 4.10).

In summary, using IMS, we have demonstrated identification and relative quantitation of disease related molecular changes in different renal regions, including individual glomeruli and tubules, directly from thin kidney sections. Low molecular weight albumin fragments and C-terminal A1AT were detected in the DN kidney. Without reducing hyperglycemia, a known influencer of kidney damage, PM treatment attenuated these markers of disease. Here, MALDI IMS is shown to be a tool to evaluate the efficacy of a therapeutic intervention, identify markers, and gain understating of the molecular mechanisms of kidney diseases.

Methods

Mouse model of diabetic nephropathy. Animal experiments were performed at the AAALAC-accredited animal facilities at Vanderbilt University Medical Center according to institutional guidelines and IACUC-approved experimental protocol. In this study, we employed eNOS^{-/-} C57BLKS db/db mice, the most robust mouse model of Type 2 DN to date. At >20 weeks of age, these mice exhibit dramatic albuminuria, arteriolar hyalinosis, increased GBM thickness, mesangial expansion, mesangiolysis, focal segmental and early nodular glomerulosclerosis, and markedly decreased GFR.¹⁰⁶ Control group included wild type C57BLKS mice. Experiment continued until mice were sacrificed at 22 wks of age. Kidneys were removed, flash frozen in liquid nitrogen and stored at -80°C. Glucose levels were measured in blood collected from the tail vein using OneTouch glucometer and Ultra test strips (LifeScan, Milpitas, CA). Albumin and creatinine excretion was determined in spot urine collected from individually caged mice using Albuwell-M kits (Exocell Inc, Philadelphia, PA).

Immunohistochemistry and immunostaining. Immunohistochemical detection of fibronectin was performed using an anti-fibronectin antibody (Sigma, St. Louis, MO). The kidney sections then were incubated using the avidin-biotin-horseradish peroxidase technique (Elite Vectastain ABC kit; Vector Laboratories, Burlingame, CA), and staining was visualized using 3,3'-diaminobenzidine. Fluorescein-labeled lotus tetragonolobus lectin (LTL) and fluorescein-labeled dolichos biflorus agglutinin (DBA) kits were from VectorLabs (Burlingame, CA). Immunostaining was performed as previously described.¹⁸³

Renal tissue preparation. Frozen kidneys were sectioned on a cryostat at 10 µm thickness and thaw mounted on to ITO coated glass slides. Kidney tissue sections were washed by immersion in 70% ethanol for 30s, 100% ethanol for 30s, Carnoy's fluid for 2 min, 100%

ethanol for 30s, water for 15s, and then 95% ethanol for 30s. Slides were then stored in a desiccator until further processing on the same day.

Histology-directed profiling: Histology-directed IMS was performed as described previously,⁶⁶ with some modifications. After washing, kidney sections were stained with 0.5% cresyl violet for 30s followed by an ethanol rinse. The cresyl violet stain aided in distinguishing the glomeruli under a microscope and is compatible with MALDI MS. Sample slides were scanned using a Mirax slide scanner from Zeiss. Mirax Viewer, Adobe Photoshop, and ImagePro were used to identify and record the coordinates of the glomeruli within the kidney sections on the digital images. Coordinates of non-glomerular cortical areas were also recorded. The coordinates of the selected areas in the kidney were transferred to the automated acoustic robotic spotter (Portrait 630, Labcyte) for deposition of trypsin and the MALDI matrix. Trypsin solution (76 ng/ μ L trypsin in 100 mM ammonium bicarbonate/10% acetonitrile) was spotted on the tissue (on the glomeruli and non-glomerular cortex coordinates) in single droplets (~120 pL) for a total of 40 iterations allowing each droplet to dry for two minutes before spotting the next droplet. Proteolytic digestion was allowed to take place for approximately two hours. Subsequently, MALDI matrix (10 mg/mL CHCA in 1:1 v/v mixture of acetonitrile and 0.2% trifluoroacetic acid) was robotically spotted on the trypsin digested glomeruli.

For high spatial resolution IMS: MALDI matrix was applied using a custom built sublimation apparatus which uses reduced pressure and heat for vapor deposition of the MALDI matrix on to the sample slide⁶¹ resulting in a uniform MALDI matrix coating over the tissue. α -Cyano-4-hydroxycinnamic acid (CHCA) was sublimed at 135°C and 50 mTorr for 30 minutes. Matrix coated sample slides were then rehydrated in a petri dish containing 1 mL of 5% TFA for 3.5 min at 85°C.

MALDI mass spectrometry. Histology-directed profiling: MALDI MS analyses of tryptic peptides were acquired on a Bruker UltrafleXtreme TOF/TOF mass spectrometer in positive ion reflectron mode. Analysis was performed with 250 shots/spectra. Digestion peptide profiles from the glomeruli were acquired in the range of m/z 600-3900. Peaks with significant intensity changes between the groups were manually selected for MS/MS fragmentation using the LIFT mode. The LIFT device raises the potential energy of the ions to induce fragmentation. MS/MS spectra were submitted to the MASCOT (Matrix Science) database search engine to match tryptic peptide sequences to their respective intact proteins.

MALDI TOF IMS: MALDI imaging experiments were performed in positive ion mode using a Bruker Ultraflex extreme mass spectrometer in linear geometry. Spectra were collected in the range of m/z 1000-20000. Raster steps were taken in 25 μm stage increments and the laser spot size was also 25 μm in diameter as measured on a thin matrix coating. Each imaging experiment was run as a set containing a kidney section from each experimental group and areas of the cortex were selected for imaging. FlexImaging was used for image visualization.

MALDI FTICR MS: MALDI imaging experiments were performed in positive ion mode using a 15 T Solarix MALDI Fourier transform ion cyclotron resonance (FTICR) mass spectrometer (Bruker Daltonics). Spectra were collected in the range of m/z of 800-10000. Image resolution was set at 60 μm . FlexImaging and DataAnalysis were used for image visualization and data analysis.

After all imaging experiments, the MALDI matrix was removed from the slides by immersion in 70% ethanol followed by 95% ethanol for 30 s each. Kidney sections were then stained with PAS and renal tissue structures were matched to MALDI IMS data via image overlay.

Protein Identification. For identification using image-directed on-tissue MS/MS, serial sections were cut and mounted on the MALDI target with the same orientation. One section was imaged to determine the localization of signals of interest. The imaged tissue was used as a guide for regions to sample on the serial section for MS/MS of the peaks of interest. Peaks were isolated and fragmented using LIFT mode on a Bruker Ultraflexreme. MS/MS spectra were searched using MASCOT. For identification using LC-MS/MS, five sections immediately following the section used for IMS were collected in 30 μ l of 50% methanol with 0.1% TFA. The sample was vortexed and then sonicated for 5 m. The homogenized sample was diluted 10-fold with 0.1% formic acid and loaded onto a C₈ reverse-phase capillary trap column using a helium-pressurized cell. The sample in the trap column was then loaded on to an analytical column for LC separation followed by mass analysis on a LTQ Orbitrap Velos (Thermo Scientific). The instrument was operated using both data-dependent and targeted scan events. To determine the mass for the targeted scan events, accurate mass measurements for the singly charged peaks of interest were acquired from tissue with a 15T MALDI FTICR MS. Two charge states per peak were then calculated to target for fragmentation in the LTQ Orbitrap Velos. For LC-MS/MS analyses, full scan (m/z 400-2000) spectra were acquired followed by electron transfer dissociation (ETD) fragmentation.

Relative abundance of protein signals: For the MALDI imaging datasets, ImageJ software (National Institutes of Health, Bethesda, MD, USA) was used to measure the relative abundance of the protein signals of interest between experimental groups. Monochromatic TIFF images were exported from FlexImaging to ImageJ. Signal intensity was measured as the mean intensity per imaged area.

Statistical analysis. Data were expressed as means \pm SEM and statistical analysis was performed using Student's *t* test for unpaired samples or ANOVA followed by post-hoc Student-Newman-Keuls comparisons. For the MALDI imaging datasets, the mean and standard error were calculated for each MS peak of interest.

CHAPTER V

CONCLUSION AND PERSPECTIVES

High Spatial Resolution Imaging for Elucidating Markers of Kidney Disease

This project investigated the molecular changes that take place in the glomerulus and kidney cortex to explore the pathogenic mechanisms of this disease by use of MALDI IMS. MALDI IMS was utilized in this study to image tissue sections of kidneys both in a healthy state and in severe DN to elucidate lipid and protein changes that occur with disease. Additionally, the response of these lipids and proteins was investigated after treatment with PM, a promising drug candidate for the treatment of diabetic nephropathy.

The first goal of this research project was to develop MALDI MS methods for direct tissue analysis of glomeruli and tubules within a kidney cortex by imaging mass spectrometry and histology directed profiling techniques. The small size of the glomerulus (~ 75 μm in mice) had previously made MALDI IMS of this tissue structure a challenge; however, recent advances in imaging resolution and sample preparation have made this accessible. Sublimation as a matrix application method has been developed for imaging of both lipids and proteins from thin kidney sections. SEM analysis (Figure 2.3) showed that this sample preparation technique resulted in a homogenous crystal coating lacking gaps with crystal sizes on the order of 1 μm , thus suitable for high spatial resolution imaging. Rehydration of the sublimated matrix coating has been found to be critical for detection of proteins from tissue. Routine MALDI MS protein imaging is now performed at 25 μm spatial resolution (Figure 2.7) and MALDI MS lipid imaging is performed at

10 μm spatial resolution (Figure 2.6). At these resolutions the glomeruli are easily imaged within the kidney cortex. This work integrated multiple modalities including high spatial resolution imaging, high mass accuracy and resolving power measurements, and standard histology (Figure 2.11) to increase the information measured from tissue sections.

After developing methods for micro-structure analysis in kidneys, kidneys from three experimental groups were studied: wild type (non-diabetic control), eNOS^{-/-} *db/db* (diabetic) and PM treated eNOS^{-/-} *db/db* mice. The eNOS^{-/-} *db/db* mouse was chosen for these studies because it is one of the most robust models, mimicking the progressive functional and structural damage documented in human diabetic nephropathy.

In Chapter III, high spatial resolution MALDI IMS (10 μm) revealed unique lipid expression in small kidney structures such as the glomeruli and tubules of the cortex. Identification and renal localization of over 75 lipids was determined (Table 3.1) with many of these differentiating disease. Overall, changes in four lipid classes- gangliosides, sulfoglycosphingolipids, lysophospholipids, and phosphatidylethanolamines were determined. One example is the ganglioside NeuAc-GM3 (m/z 1151.7) and its hydroxylated derivative NeuGc-GM3 (m/z 1167.7). The former was found to localize to the glomeruli of all three kidney types whereas the latter was observed only in the DN glomeruli (Figure 3.3). Attenuated levels of NeuGc-GM3 were observed in PM treated DN glomeruli. Additionally, high mass accuracy measurements using FTICR MS indicate early glycation product modifications (Amadori, +162.0528 Da) on specific phosphatidylethanolamine (PE) lipids in the diabetic kidney tissue (Figure 5.1). It has been found that the modified PEs localize to the cortex region of the diabetic kidneys. Over 15 glucose modified PEs have been detected and imaged. This is the first report of the detection along with spatial localization of Amadori-PEs in tissue.

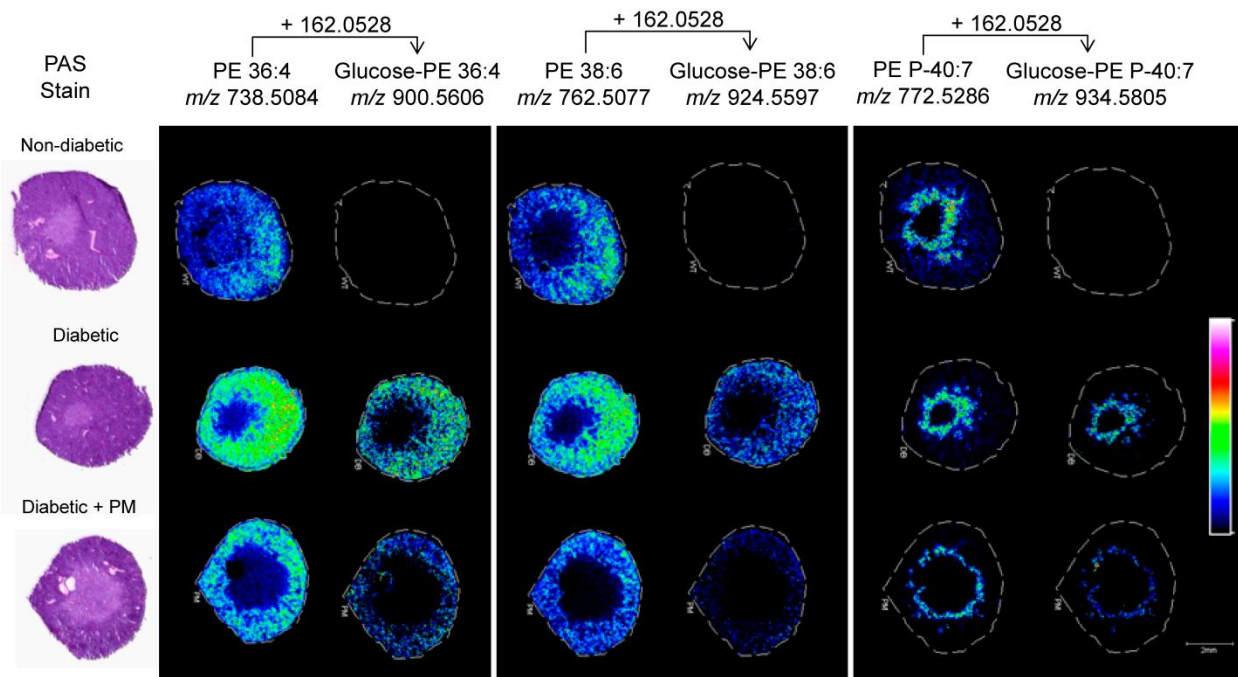


Figure 5.1. Glucose modified PE's are increased in the cortex region of the diabetic kidneys.

In Chapter IV, protein expression changes were investigated in the kidney cortex of the different experimental groups. Specific to glomeruli, fibronectin (Figure 4.2) and a signal at m/z 4415 (Figure 4.5) were found to be increased. The signal at m/z 4415 is suspected to be a carboxyethyl lysine AGE modification on the signal at m/z 4343 based on the co-localization of the two signals, the increase in DN, and the reduction with PM treatment. Interestingly this marker seems to correlate with more diseased glomeruli (Figure 5.2). Further, other signals increased in the DN kidneys were identified which included C-terminal regions of A1AT (Figure 4.9) and fragments of albumin (Table 4.2, Figure 4.10). The renal localization and differential relative abundance of these proteins between experimental groups was determined. In all cases, these were the most abundant in untreated DN tissue and attenuated in PM treated DN kidneys. A1AT may have a role in ECM accumulation and albumin is a known marker to increase in diabetic urine and so the increased detection of albumin fragments provides further data on how its processing is altered in DN. These data provide new molecular insight on what is happening in DN and may prove to be useful markers of disease and progression.

Future Research Directions

Investigation of Other Organs Affected by Diabetes

Future work will extend this study to other organs affected by diabetes. It is of interest to not only explore other molecules that change in organs such as the liver, brain, heart and eyes, but to investigate if the findings in the kidney are unique to this organ or extend to other organs. The liver is in fact a major source of A1AT and so tracking the expression and form of this protein at different stages of diabetes in the liver could be of interest. Additionally, lipids are a part of every organ and so determining the expression and localization of modified lipids in different organs affected by diabetes should be done. In fact, work is already being done in livers to

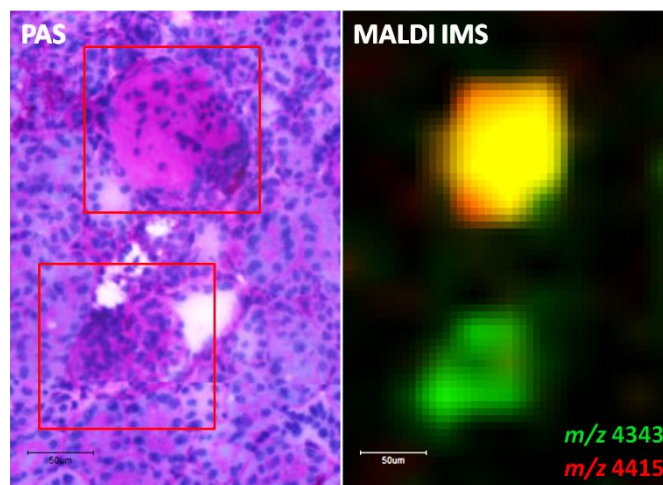


Figure 5.2. Markers of diseased glomeruli. The signal at m/z 4415 (plotted in red in the MALDI image) was found to localize to more sclerotic glomeruli (as observed with the brighter pink PAS staining). Note- yellow indicates co-localization of the red and green signals. Scale bar = 50 μ m.

look for modified PEs. Figure 5.3 shows two different PE modifications detected in the diabetic liver, the Amadori-PE that was described in kidneys in Chapter III, and a carboxymethyl (CM)-PE that is more abundant in the diabetic liver as well. CM is another AGE modification.

Increasing Spatial Resolution and Sensitivity

MALDI imaging was first introduced almost two decades ago. Since this time, aside from the applications it was used for, much of the research surrounding it was focused on advancements in spatial resolution and sensitivity. Significant progress has been made and these efforts are still ongoing. It is expected that routine imaging will soon be performed at a spatial resolution of $< 1 \mu\text{m}$. The average mammalian cell is $\sim 8 \mu\text{m}$ and so this will provide structural resolution below the single cell level. This will truly put IMS on par with standard optical pathology but with multiplexed molecular specific images. The level of detail provided at this spatial resolution is highlighted in Figure 5.4 where a human kidney section was imaged showing a unique display of specific biomolecules highlighting different tubular structures and a single glomerulus. This was imaged with a $2 \mu\text{m}$ spatial resolution using a custom built instrument with transmission geometry laser optics to achieve a highly focused beam. As laser spot sizes get smaller and smaller however, the number of molecules ablated is reduced as well. Much effort will need to be focused on further improving sample preparation and increasing sensitivity.

Application to Human Studies

The present study found a number of lipids and proteins that correlated with disease in a robust mouse model of DN. It would be of great interest to extend these studies to human diabetes to determine if these molecules are involved in human DN pathogenesis and are

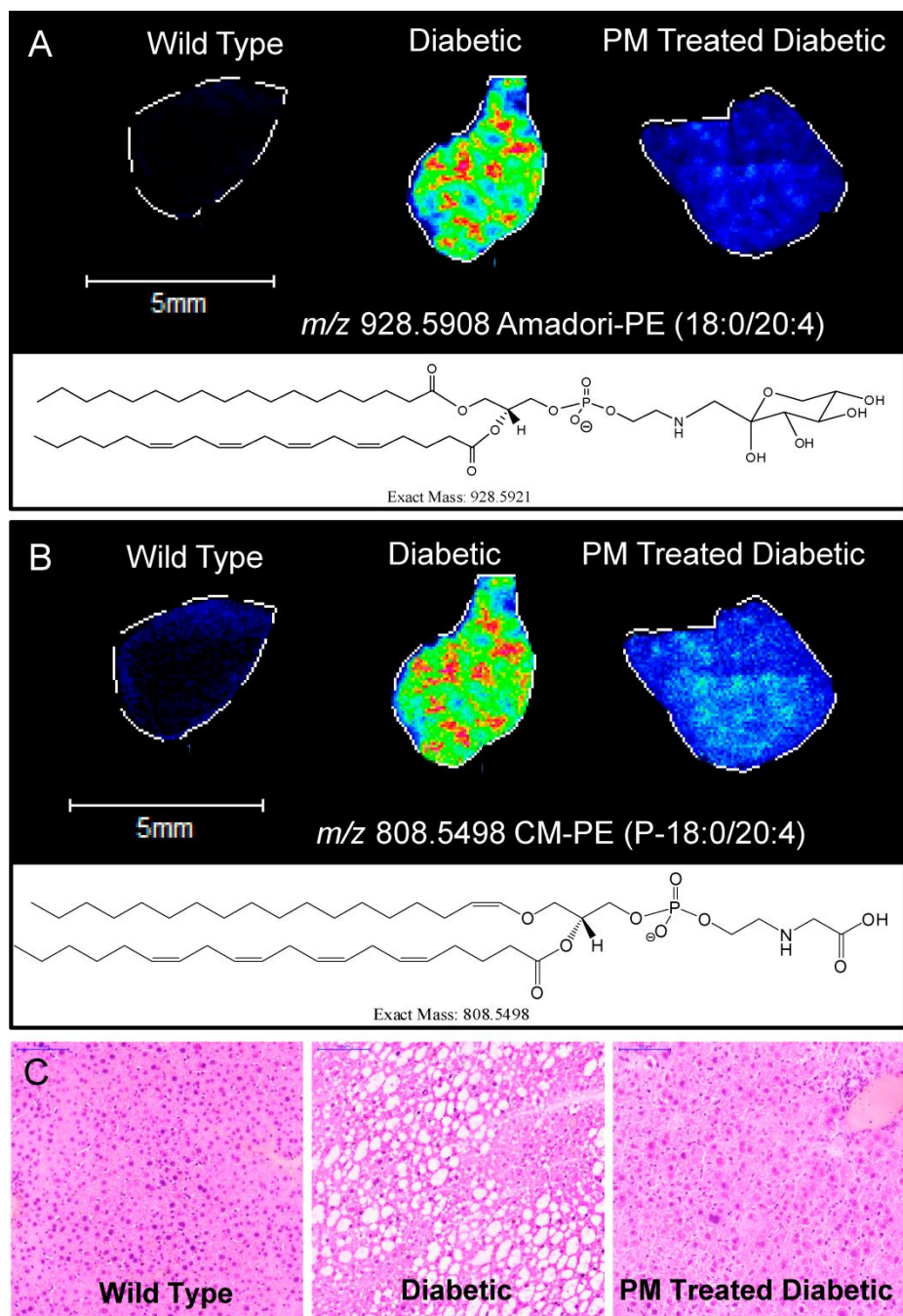
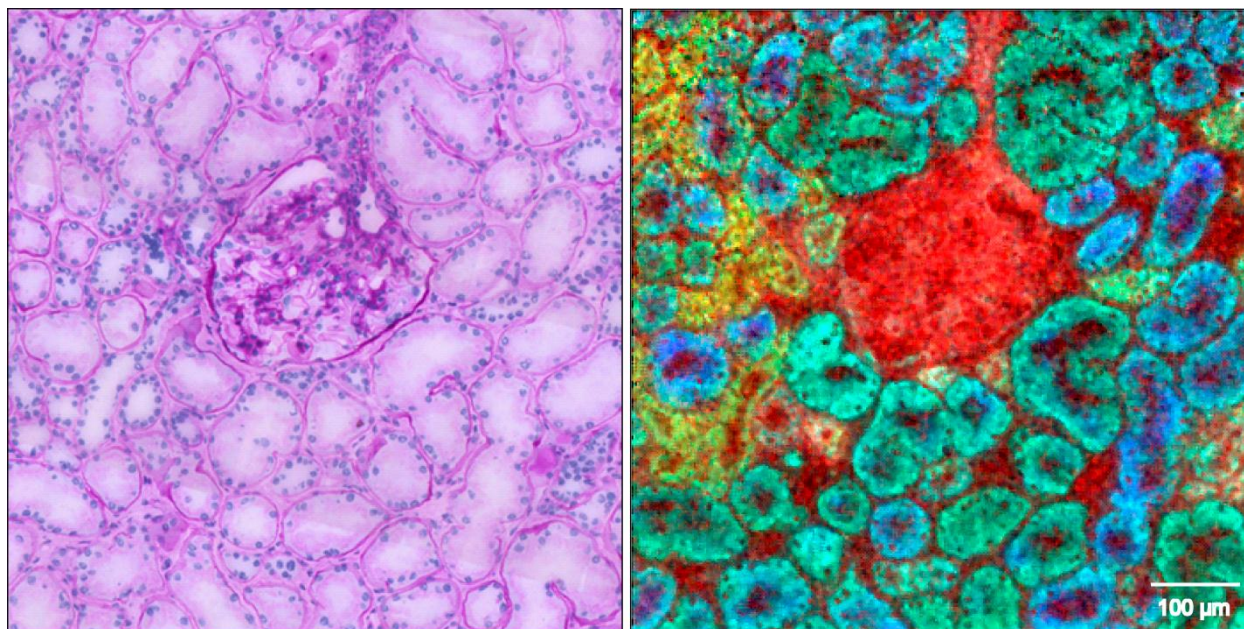


Figure 5.3. Modified lipids in diabetic livers. (A) Example of an Amadori-PE shown to increase in the diabetic liver. (B) Example of a carboxymethyl-PE (CM-PE) shown to increase in the diabetic liver. (C) H&E histology of a liver from each group.



Human Kidney
PAS Stain

2 μm IMS Ion Overlay with Tentative IDs

Red = m/z 750; PE(P-38:4)

Yellow = m/z 863; PI(36:1)

Green = m/z 885; PI(38:4)

Blue = m/z 1052; SM3 (d18:1/24:0)

Figure 5.4. Lipid IMS of human kidney section. On the right is an ion image overlay of four lipid species imaged at 2 μm spatial resolution using transmission geometry MALDI IMS. On the left is a PAS stain of the section serial to the one imaged with IMS. Scale bar = 100 μm .

biomarkers of human disease. Kidney biopsy is not currently the standard care for diagnosis of DN so tissue sources are not abundant. However there are cases where biopsy is performed and this could be valuable tissue to apply the methods described in this work. New and specific knowledge gained from these studies may lead to more accurate diagnosis and prognosis potentially raising the need to reevaluate the use of biopsy. The methods described in this work are directly applicable to human tissue for both lipid and protein imaging as demonstrated in Figure 5.4 and Figure 5.5, respectively.

Conclusions

In summary, high spatial resolution molecular imaging was used to elucidate changes in different classes of biomolecules including proteins and lipids in diseased and healthy kidneys. These measurements have shown lipid and protein alterations directly at the site of disease (i.e. - glomerular and tubular lesions). Additionally, PM treatment was found to reduce the severity of DN assessed by both pathology analysis and molecular analysis as determined by imaging mass spectrometry. Without reducing hyperglycemia, PM, an inhibitor of non-enzymatic oxidative pathways, attenuated the levels of lipids and proteins found in this study to associate with DN. This suggests that these molecules require hyperglycemia-induced oxidative pathways. This high resolution imaging technology is a powerful tool to determine the spatial context of molecular changes, specifically to detect protein and lipid modifications associated with diabetic nephropathy from specific structures within the renal cortex. Determining proteins that undergo change in disease conditions and evaluating response to treatment may lead to new molecular markers of disease, provide insight into disease pathogenesis, and characterize

treatment response. This technology can have an impact not just in diabetic nephropathy, but any kidney disease as we are measuring minute changes in intact tissue.

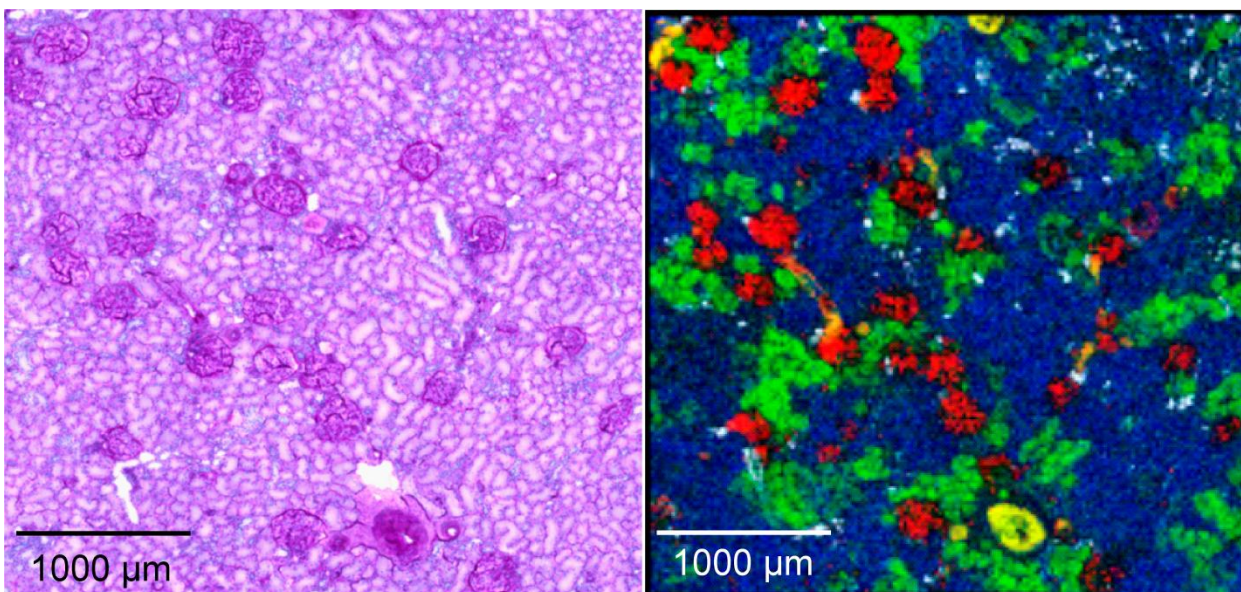


Figure 5.5. Protein IMS of human kidney. On the right is a 20 μm spatial resolution IMS ion image overlay displaying m/z 1618 (blue), m/z 1950 (white), m/z 2592 (green), m/z 8415 (yellow), and m/z 13787 (red). The PAS stain on the left is of the same section.

REFERENCES

1. Centers for Disease Control and Prevention. National diabetes fact sheet: national estimates and general information on diabetes and prediabetes in the United States, 2011. Atlanta, GA: U.S. Department of Health and Human Services, Centers for Disease Control and Prevention, 2011.
2. Collins, AJ, Foley, RN, Chavers, B, Gilbertson, D, Herzog, C, Johansen, K, Kasiske, B, Kutner, N, Liu, J, St Peter, W, Guo, H, Gustafson, S, Heubner, B, Lamb, K, Li, S, Peng, Y, Qiu, Y, Roberts, T, Skeans, M, Snyder, J, Solid, C, Thompson, B, Wang, C, Weinhandl, E, Zaun, D, Arko, C, Chen, SC, Daniels, F, Ebben, J, Frazier, E, Hanzlik, C, Johnson, R, Sheets, D, Wang, X, Forrest, B, Constantini, E, Everson, S, Eggers, P, Agodoa, L: 'United States Renal Data System 2011 Annual Data Report: Atlas of chronic kidney disease & end-stage renal disease in the United States. *Am J Kidney Dis*, 59: A7, e1-420, 2012.
3. Gross, JL, de Azevedo, MJ, Silveiro, SP, Canani, LH, Caramori, ML, Zelmanovitz, T: Diabetic Nephropathy: Diagnosis, Prevention, and Treatment. *Diabetes Care*, 28: 164-176, 2005.
4. Cooper, ME: Pathogenesis, prevention, and treatment of diabetic nephropathy. *The Lancet*, 352: 213-219, 1998.
5. Brownlee, M: Biochemistry and molecular cell biology of diabetic complications. *Nature*, 414: 813-820, 2001.
6. Adler, AI, Stratton, IM, Neil, HAW, Yudkin, JS, Matthews, DR, Cull, CA, Wright, AD, Turner, RC, Holman, RR: Association of systolic blood pressure with macrovascular and microvascular complications of type 2 diabetes (UKPDS 36): prospective observational study. *BMJ*, 321: 412-419, 2000.
7. Ravid, M, Brosh, D, Ravid-Safran, D, Levy, Z, Rachmani, R: MAin risk factors for nephropathy in type 2 diabetes mellitus are plasma cholesterol levels, mean blood pressure, and hyperglycemia. *Archives of Internal Medicine*, 158: 998-004, 1998.
8. Nishikawa, T, Edelstein, D, Du, XL, Yamagishi, S-i, Matsumura, T, Kaneda, Y, Yorek, MA, Beebe, D, Oates, PJ, Hammes, H-P, Giardino, I, Brownlee, M: Normalizing mitochondrial superoxide production blocks three pathways of hyperglycaemic damage. *Nature*, 404: 787-790, 2000.

9. Kanwar, YS, Sun, L, Xie, P, Liu, F-y, Chen, S: A Glimpse of Various Pathogenetic Mechanisms of Diabetic Nephropathy. *Annual Review of Pathology: Mechanisms of Disease*, 6: 395-423, 2011.
10. Forbes, JM, Coughlan, MT, Cooper, ME: Oxidative Stress as a Major Culprit in Kidney Disease in Diabetes. *Diabetes*, 57: 1446-1454, 2008.
11. LEASK, A, ABRAHAM, DJ: TGF- β signaling and the fibrotic response. *The FASEB Journal*, 18: 816-827, 2004.
12. Ziyadeh, FN: Mediators of Diabetic Renal Disease: The Case for TGF- β as the Major Mediator. *J Am Soc Nephrol*, 15: S55-S57, 2004.
13. Mott, JD, Khalifah, RG, Nagase, H, Shield Iii, CF, Hudson, JK, Hudson, BG: Nonenzymatic glycation of type IV collagen and matrix metalloproteinase susceptibility. *Kidney Int*, 52: 1302-1312, 1997.
14. Zent, R, Yan, X, Su, Y, Hudson, BG, Borza, DB, Moeckel, GW, Qi, Z, Sado, Y, Breyer, MD, Voziyan, P, Pozzi, A: Glomerular injury is exacerbated in diabetic integrin [alpha]1-null mice. *Kidney Int*, 70: 460-470, 2006.
15. Pedchenko, VK, Chetyrkin, SV, Chuang, P, Ham, A-JL, Saleem, MA, Mathieson, PW, Hudson, BG, Voziyan, PA: Mechanism of Perturbation of Integrin-Mediated Cell-Matrix Interactions by Reactive Carbonyl Compounds and Its Implication for Pathogenesis of Diabetic Nephropathy. *Diabetes*, 54: 2952-2960, 2005.
16. Brownlee, M: The Pathobiology of Diabetic Complications: A Unifying Mechanism. *Diabetes*, 54: 1615-1625, 2005.
17. Alsaad, KO, Herzenberg, AM: Distinguishing diabetic nephropathy from other causes of glomerulosclerosis: an update. *Journal of Clinical Pathology*, 60: 18-26, 2007.
18. Williams, ME: New Potential Agents in Treating Diabetic Kidney Disease: The Fourth Act. *Drugs*, 66: 2287-2298, 2006.
19. Voziyan, PA, Hudson, BG: Pyridoxamine: The Many Virtues of a Maillard Reaction Inhibitor. *Annals of the New York Academy of Sciences*, 1043: 807-816, 2005.

20. Chetyrkin, S, Mathis, M, Hayes McDonald, W, Shackelford, X, Hudson, B, Voziyan, P: Pyridoxamine protects protein backbone from oxidative fragmentation. *Biochem Biophys Res Commun*, 411: 574-579, 2011.
21. Chetyrkin, SV, Mathis, ME, Ham, AJ, Hachey, DL, Hudson, BG, Voziyan, PA: Propagation of protein glycation damage involves modification of tryptophan residues via reactive oxygen species: inhibition by pyridoxamine. *Free Radic Biol Med*, 44: 1276-1285, 2008.
22. Onorato, JM, Jenkins, AJ, Thorpe, SR, Baynes, JW: Pyridoxamine, an Inhibitor of Advanced Glycation Reactions, Also Inhibits Advanced Lipoxidation Reactions: Mechanism of Action of Pyridoxamine. *Journal of Biological Chemistry*, 275: 21177-21184, 2000.
23. Voziyan, PA, Khalifah, RG, Thibaudeau, C, Yildiz, A, Jacob, J, Serianni, AS, Hudson, BG: Modification of Proteins In Vitro by Physiological Levels of Glucose: Pyridoxamine inhibits conversion of Amadori intermediate to advanced glycation end-products through binding of redox metal ions. *Journal of Biological Chemistry*, 278: 46616-46624, 2003.
24. Tanimoto, M, Gohda, T, Kaneko, S, Hagiwara, S, Murakoshi, M, Aoki, T, Yamada, K, Ito, T, Matsumoto, M, Horikoshi, S, Tomino, Y: Effect of pyridoxamine (K-163), an inhibitor of advanced glycation end products, on type 2 diabetic nephropathy in KK-A(y)/Ta mice. *Metabolism*, 56: 160-167, 2007.
25. Williams, ME, Bolton, WK, Khalifah, RG, Degenhardt, TP, Schotzinger, RJ, McGill, JB: Effects of Pyridoxamine in Combined Phase 2 Studies of Patients with Type 1 and Type 2 Diabetes and Overt Nephropathy. *American Journal of Nephrology*, 27: 605-614, 2007.
26. Zheng, F, Zeng, YJ, Plati, AR, Elliot, SJ, Berho, M, Potier, M, Striker, LJ, Striker, GE: Combined AGE inhibition and ACEi decreases the progression of established diabetic nephropathy in B6 db/db mice. *Kidney Int*, 70: 507-514, 2006.
27. Alderson, NL, Chachich, ME, Youssef, NN, Beattie, RJ, Nachtigal, M, Thorpe, SR, Baynes, JW: The AGE inhibitor pyridoxamine inhibits lipemia and development of renal and vascular disease in Zucker obese rats. *Kidney Int*, 63: 2123-2133, 2003.

28. Degenhardt, TP, Alderson, NL, Arrington, DD, Beattie, RJ, Basgen, JM, Steffes, MW, Thorpe, SR, Baynes, JW: Pyridoxamine inhibits early renal disease and dyslipidemia in the streptozotocin-diabetic rat. *Kidney Int*, 61: 939-950, 2002.
29. Lewis, EJ, Greene, T, Spitalewiz, S, Blumenthal, S, Berl, T, Hunsicker, LG, Pohl, MA, Rohde, RD, Raz, I, Yerushalmy, Y, Yagil, Y, Herskovits, T, Atkins, RC, Reutens, AT, Packham, DK, Lewis, JB, Group, ftCS: Pyridorin in Type 2 Diabetic Nephropathy. *J Am Soc Nephrol*, 23: 131-136, 2012.
30. Haraldsson, B, Nyström, J, Deen, WM: Properties of the Glomerular Barrier and Mechanisms of Proteinuria. *Physiological Reviews*, 88: 451-487, 2008.
31. Parving, H-H, Smidt, U, Andersen, A, Svendsen, P: Early Aggressive Antihypertensive Treatment Reduces Rate of Decline In Kidney Function In Diabetic Nephropathy *The Lancet*, 321: 1175-1179, 1983.
32. Parving, H-H, Lehnert, H, Bröchner-Mortensen, J, Gomis, R, Andersen, S, Arner, P: The Effect of Irbesartan on the Development of Diabetic Nephropathy in Patients with Type 2 Diabetes. *New England Journal of Medicine*, 345: 870-878, 2001.
33. Lewis, EJ, Hunsicker, LG, Bain, RP, Rohde, RD: The Effect of Angiotensin-Converting-Enzyme Inhibition on Diabetic Nephropathy. *New England Journal of Medicine*, 329: 1456-1462, 1993.
34. Viberti, GC, Jarrett, RJ, Mahmud, U, Hill, RD, Argyropoulos, A, Keen, H: Microalbuminuria as a Predictor of Clinical Nephropathy in Insulin-dependent Diabetes Mellitus. *The Lancet*, 319: 1430-1432, 1982.
35. Satoskar, AA, Shapiro, JP, Bott, CN, Song, H, Nadasdy, GM, Brodsky, SV, Hebert, LA, Birmingham, DJ, Nadasdy, T, Freitas, MA, Rovin, BH: Characterization of glomerular diseases using proteomic analysis of laser capture microdissected glomeruli. *Mod Pathol*, 25: 709-721, 2012.
36. Mauer, SM, Steffes, MW, Ellis, EN, Sutherland, DER, Brown, DM, Goetz, FC: roStructural-Functional Relationships in Diabetic Nephropathy. *J Clin Invest*, 74: 1143-1155, 1984.
37. Alpers, CE, Hudkins, KL: Mouse models of diabetic nephropathy. *Curr Opin Nephrol Hypertens*, 20: 278-284, 2011.

38. Zhao, HJ, Wang, S, Cheng, H, Zhang, M-z, Takahashi, T, Fogo, AB, Breyer, MD, Harris, RC: Endothelial Nitric Oxide Synthase Deficiency Produces Accelerated Nephropathy in Diabetic Mice. *J Am Soc Nephrol*, 17: 2664-2669, 2006.
39. Mohan, S, Reddick, RL, Musi, N, Horn, DA, Yan, B, Prihoda, TJ, Natarajan, M, Abboud-Werner, SL: Diabetic eNOS knockout mice develop distinct macro- and microvascular complications. *Lab Invest*, 88: 515-528, 2008.
40. Tanaka, K, Waki, H, Ido, Y, Akita, S, Yoshida, Y, Yoshida, T, Matsuo, T: Protein and polymer analyses up to m/z 100 000 by laser ionization time-of-flight mass spectrometry. *Rapid Communications in Mass Spectrometry*, 2: 151-153, 1988.
41. Karas, M, Bachmann, D, Bahr, U, Hillenkamp, F: Matrix-assisted ultraviolet laser desorption of non-volatile compounds. *International Journal of Mass Spectrometry and Ion Processes*, 78: 53-68, 1987.
42. Karas, M, Hillenkamp, F: Laser desorption ionization of proteins with molecular masses exceeding 10,000 daltons. *Analytical Chemistry*, 60: 2299-2301, 1988.
43. Fenn, J, Mann, M, Meng, C, Wong, S, Whitehouse, C: Electrospray ionization for mass spectrometry of large biomolecules. *Science*, 246: 64-71, 1989.
44. Wiley, WC, McLaren, IH: Time-of-Flight Mass Spectrometer with Improved Resolution. *Review of Scientific Instruments*, 26: 1150-1157, 1955.
45. Vestal, ML, Juhasz, P, Martin, SA: Delayed extraction matrix-assisted laser desorption time-of-flight mass spectrometry. *Rapid Communications in Mass Spectrometry*, 9: 1044-1050, 1995.
46. Marshall, AG, Hendrickson, CL, Jackson, GS: Fourier transform ion cyclotron resonance mass spectrometry: A primer. *Mass Spectrometry Reviews*, 17: 1-35, 1998.
47. Marshall, AG, Hendrickson, CL: Fourier transform ion cyclotron resonance detection: principles and experimental configurations. *International Journal of Mass Spectrometry*, 215: 59-75, 2002.
48. Amster, IJ: Fourier Transform Mass Spectrometry. *Journal of Mass Spectrometry*, 31: 1325-1337, 1996.

49. Colliver, TL, Brummel, CL, Pacholski, ML, Swanek, FD, Ewing, AG, Winograd, N: Atomic and Molecular Imaging at the Single-Cell Level with TOF-SIMS. *Analytical Chemistry*, 69: 2225-2231, 1997.
50. Gillen, G, Bennett, J, Tarlov, MJ, Burgess, DRF: Molecular Imaging Secondary Ion Mass Spectrometry for the Characterization of Patterned Self-Assembled Monolayers on Silver and Gold. *Analytical Chemistry*, 66: 2170-2174, 1994.
51. Hillenkamp, F, Unsöld, E, Kaufmann, R, Nitsche, R: A high-sensitivity laser microprobe mass analyzer. *Appl Phys*, 8: 341-348, 1975.
52. Spengler, B, Hubert, M: Scanning microprobe matrix-assisted laser desorption ionization (SMALDI) mass spectrometry: Instrumentation for sub-micrometer resolved LDI and MALDI surface analysis. *Journal of the American Society for Mass Spectrometry*, 13: 735-748, 2002.
53. Wilk, ZA, Hercules, DM: Organic and elemental ion mapping using laser mass spectrometry. *Analytical Chemistry*, 59: 1819-1825, 1987.
54. Zavalin, A, Todd, EM, Rawhouser, PD, Yang, J, Norris, JL, Caprioli, RM: Direct imaging of single cells and tissue at sub-cellular spatial resolution using transmission geometry MALDI MS. *Journal of Mass Spectrometry*, 47: 1473-1481, 2012.
55. McDonnell, LA, Heeren, RMA: Imaging mass spectrometry. *Mass Spectrometry Reviews*, 26: 606-643, 2007.
56. Chaurand, P, Norris, JL, Cornett, DS, Mobley, JA, Caprioli, RM: New Developments in Profiling and Imaging of Proteins from Tissue Sections by MALDI Mass Spectrometry. *Journal of Proteome Research*, 5: 2889-2900, 2006.
57. Seeley, EH, Schwamborn, K, Caprioli, RM: Imaging of Intact Tissue Sections: Moving beyond the Microscope. *Journal of Biological Chemistry*, 286: 25459-25466, 2011.
58. Cornett, DS, Reyzer, ML, Chaurand, P, Caprioli, RM: MALDI imaging mass spectrometry: molecular snapshots of biochemical systems. *Nat Meth*, 4: 828-833, 2007.

59. Caprioli, RM, Farmer, TB, Gile, J: Molecular Imaging of Biological Samples: Localization of Peptides and Proteins Using MALDI-TOF MS. *Analytical Chemistry*, 69: 4751-4760, 1997.
60. Chaurand, P, Caprioli, RM: Direct profiling and imaging of peptides and proteins from mammalian cells and tissue sections by mass spectrometry. *Electrophoresis*, 23: 3125-3135, 2002.
61. Hankin, JA, Barkley, RM, Murphy, RC: Sublimation as a Method of Matrix Application for Mass Spectrometric Imaging. *Journal of the American Society for Mass Spectrometry*, 18: 1646-1652, 2007.
62. Puolitaival, SM, Burnum, KE, Cornett, DS, Caprioli, RM: Solvent-Free Matrix Dry-Coating for MALDI Imaging of Phospholipids. *Journal of the American Society for Mass Spectrometry*, 19: 882-886, 2008.
63. Khatib-Shahidi, S, Andersson, M, Herman, JL, Gillespie, TA, Caprioli, RM: Direct Molecular Analysis of Whole-Body Animal Tissue Sections by Imaging MALDI Mass Spectrometry. *Analytical Chemistry*, 78: 6448-6456, 2006.
64. Groseclose, MR, Massion, PP, Chaurand, P, Caprioli, RM: High-throughput proteomic analysis of formalin-fixed paraffin-embedded tissue microarrays using MALDI imaging mass spectrometry. *PROTEOMICS*, 8: 3715-3724, 2008.
65. Lazova, R, Seeley, EH, Keenan, M, Gueorguieva, R, Caprioli, RM: Imaging Mass Spectrometry—A New and Promising Method to Differentiate Spitz Nevi From Spitzoid Malignant Melanomas. *The American Journal of Dermatopathology*, 34: 82-90 10.1097/DAD.1090b1013e31823df31821e31822, 2012.
66. Cornett, DS, Mobley, JA, Dias, EC, Andersson, M, Arteaga, CL, Sanders, ME, Caprioli, RM: A Novel Histology-directed Strategy for MALDI-MS Tissue Profiling That Improves Throughput and Cellular Specificity in Human Breast Cancer. *Molecular & Cellular Proteomics*, 5: 1975-1983, 2006.
67. Bowlus, CL, Seeley, EH, Roder, J, Grigorieva, J, Roder, H, Caprioli, RM, Gershwin, M: In situ mass spectrometry of autoimmune liver diseases. *Cell Mol Immunol*, 8: 237-242, 2011.
68. Römpp, A, Guenther, S, Takats, Z, Spengler, B: Mass spectrometry imaging with high resolution in mass and space (HR2 MSI) for reliable investigation of drug

- compound distributions on the cellular level. *Analytical and Bioanalytical Chemistry*, 401: 65-73, 2011.
69. Ruh, H, Salonikios, T, Fuchser, J, Schwartz, M, Sticht, C, Hochheim, C, Wurnitzer, B, Gretz, N, Hopf, C: MALDI imaging MS reveals candidate lipid markers of polycystic kidney disease. *Journal of Lipid Research*, 2013.
70. Meistermann, Hln, Norris, JL, Aerni, H-R, Cornett, DS, Friedlein, A, Erskine, AR, Augustin, Al, De Vera Mudry, MC, Ruepp, S, Suter, L, Langen, H, Caprioli, RM, Ducret, A: Biomarker Discovery by Imaging Mass Spectrometry. *Molecular & Cellular Proteomics*, 5: 1876-1886, 2006.
71. Guenther, S, Römpf, A, Kummer, W, Spengler, B: AP-MALDI Imaging of neuropeptides in mouse pituitary gland with 5 [μ]m spatial resolution and high mass accuracy. *International Journal of Mass Spectrometry*, In Press, Accepted Manuscript.
72. Lagarrigue, M, Becker, M, Lavigne, R, Deininger, S-O, Walch, A, Aubry, F, Suckau, D, Pineau, C: Revisiting rat spermatogenesis with MALDI imaging at 20 $\hat{\mu}$ m resolution. *Molecular & Cellular Proteomics*.
73. Chaurand, P, Schriver, KE, Caprioli, RM: Instrument design and characterization for high resolution MALDI-MS imaging of tissue sections. *Journal of Mass Spectrometry*, 42: 476-489, 2007.
74. Zavalin, A, Yang, J, Caprioli, R: Laser Beam Filtration for High Spatial Resolution MALDI Imaging Mass Spectrometry. *Journal of the American Society for Mass Spectrometry*, 24: 1153-1156, 2013.
75. Seeley, EH, Oppenheimer, SR, Mi, D, Chaurand, P, Caprioli, RM: Enhancement of Protein Sensitivity for MALDI Imaging Mass Spectrometry After Chemical Treatment of Tissue Sections. *Journal of the American Society for Mass Spectrometry*, 19: 1069-1077, 2008.
76. Angel, PM, Spraggins, JM, Baldwin, HS, Caprioli, R: Enhanced Sensitivity for High Spatial Resolution Lipid Analysis by Negative Ion Mode Matrix Assisted Laser Desorption Ionization Imaging Mass Spectrometry. *Analytical Chemistry*, 84: 1557-1564, 2012.

77. Spraggins, J, Caprioli, R: High-Speed MALDI-TOF Imaging Mass Spectrometry: Rapid Ion Image Acquisition and Considerations for Next Generation Instrumentation. *Journal of the American Society for Mass Spectrometry*, 22: 1022-1031, 2011.
78. Aerni, H-R, Cornett, DS, Caprioli, RM: Automated Acoustic Matrix Deposition for MALDI Sample Preparation. *Analytical Chemistry*, 78: 827-834, 2005.
79. Grove, K, Frappier, S, Caprioli, R: Matrix Pre-Coated MALDI MS Targets for Small Molecule Imaging in Tissues. *Journal of the American Society for Mass Spectrometry*, 22: 192-195, 2011.
80. Bouschen, W, Schulz, O, Eikel, D, Spengler, B: Matrix vapor deposition/recrystallization and dedicated spray preparation for high-resolution scanning microprobe matrix-assisted laser desorption/ionization imaging mass spectrometry (SMALDI-MS) of tissue and single cells. *Rapid Communications in Mass Spectrometry*, 24: 355-364.
81. Yang, J, Caprioli, RM: Matrix Sublimation/Recrystallization for Imaging Proteins by Mass Spectrometry at High Spatial Resolution. *Analytical Chemistry*, 83: 5728-5734, 2011.
82. Stoeckli, M, Chaurand, P, Hallahan, DE, Caprioli, RM: Imaging mass spectrometry: A new technology for the analysis of protein expression in mammalian tissues. *Nat Med*, 7: 493-496, 2001.
83. Seeley, EH, Caprioli, RM: Molecular imaging of proteins in tissues by mass spectrometry. *Proceedings of the National Academy of Sciences*, 105: 18126-18131, 2008.
84. Herring, KD, Oppenheimer, SR, Caprioli, RM: Direct Tissue Analysis by Matrix-Assisted Laser Desorption Ionization Mass Spectrometry: Application to Kidney Biology. *Seminars in Nephrology*, 27: 597-608, 2007.
85. Lalowski, M, Magni, F, Mainini, V, Monogioudi, E, Gotsopoulos, A, Soliymani, R, Chinello, C, Baumann, M: Imaging mass spectrometry: a new tool for kidney disease investigations. *Nephrology Dialysis Transplantation*, 2013.

86. Oppenheimer, SR, Mi, D, Sanders, ME, Caprioli, RM: Molecular Analysis of Tumor Margins by MALDI Mass Spectrometry in Renal Carcinoma. *Journal of Proteome Research*, 9: 2182-2190, 2010.
87. Marsching, C, Eckhardt, M, Gröne, H-J, Sandhoff, R, Hopf, C: Imaging of complex sulfatides SM3 and SB1a in mouse kidney using MALDI-TOF/TOF mass spectrometry. *Analytical and Bioanalytical Chemistry*, 401: 53-64, 2011.
88. Kaneko, Y, Obata, Y, Nishino, T, Takeya, H, Miyazaki, Y, Hayasaka, T, Setou, M, Furusu, A, Kohno, S: Imaging mass spectrometry analysis reveals an altered lipid distribution pattern in the tubular areas of hyper-IgA murine kidneys. *Experimental and Molecular Pathology*, 91: 614-621, 2011.
89. Xu, BJ, Shyr, Y, Liang, X, Ma, L-j, Donnert, EM, Roberts, JD, Zhang, X, Kon, V, Brown, NJ, Caprioli, RM, Fogo, AB: Proteomic Patterns and Prediction of Glomerulosclerosis and Its Mechanisms. *J Am Soc Nephrol*, 16: 2967-2975, 2005.
90. Schwartz, SA, Reyzer, ML, Caprioli, RM: Direct tissue analysis using matrix-assisted laser desorption/ionization mass spectrometry: practical aspects of sample preparation. *Journal of Mass Spectrometry*, 38: 699-708, 2003.
91. Lemaire, R, Desmons, A, Tabet, JC, Day, R, Salzert, M, Fournier, I: Direct Analysis and MALDI Imaging of Formalin-Fixed, Paraffin-Embedded Tissue Sections. *Journal of Proteome Research*, 6: 1295-1305, 2007.
92. Thomas, A, Charbonneau, JL, Fournaise, E, Chaurand, P: Sublimation of New Matrix Candidates for High Spatial Resolution Imaging Mass Spectrometry of Lipids: Enhanced Information in Both Positive and Negative Polarities after 1,5-Diaminonaphthalene Deposition. *Analytical Chemistry*, 84: 2048-2054, 2012.
93. Fuchs, B, Bischoff, A, Süß, R, Teuber, K, Schürenberg, M, Suckau, D, Schiller, J: Phosphatidylcholines and -ethanolamines can be easily mistaken in phospholipid mixtures: a negative ion MALDI-TOF MS study with 9-aminoacridine as matrix and egg yolk as selected example. *Analytical and Bioanalytical Chemistry*, 395: 2479-2487, 2009.
94. Dong, W, Shen, Q, Baibado, JT, Liang, Y, Wang, P, Huang, Y, Zhang, Z, Wang, Y, Cheung, H-Y: Phospholipid analyses by MALDI-TOF/TOF mass spectrometry using 1,5-diaminonaphthalene as matrix. *International Journal of Mass Spectrometry*, 343-344: 15-22, 2013.

95. Chaurand, P, Schwartz, SA, Billheimer, D, Xu, BJ, Crecelius, A, Caprioli, RM: Integrating Histology and Imaging Mass Spectrometry. *Analytical Chemistry*, 76: 1145-1155, 2004.
96. Groseclose, MR, Andersson, M, Hardesty, WM, Caprioli, RM: Identification of proteins directly from tissue: in situ tryptic digestions coupled with imaging mass spectrometry. *Journal of Mass Spectrometry*, 42: 254-262, 2007.
97. Norris, JL, Cornett, DS, Mobley, JA, Andersson, M, Seeley, EH, Chaurand, P, Caprioli, RM: Processing MALDI mass spectra to improve mass spectral direct tissue analysis. *International Journal of Mass Spectrometry*, 260: 212-221, 2007.
98. Rutledge, JC, Ng, KF, Aung, HH, Wilson, DW: Role of triglyceride-rich lipoproteins in diabetic nephropathy. *Nat Rev Nephrol*, 6: 361-370, 2010.
99. Balla, T: Phosphoinositides: tiny lipids with giant impact on cell regulation. *Physiol Rev*, 93: 1019-1137, 2013.
100. Kinnunen, PK, Kaarniranta, K, Mahalka, AK: Protein-oxidized phospholipid interactions in cellular signaling for cell death: from biophysics to clinical correlations. *Biochim Biophys Acta*, 1818: 2446-2455, 2012.
101. Weijers, RN: Lipid composition of cell membranes and its relevance in type 2 diabetes mellitus. *Curr Diabetes Rev*, 8: 390-400, 2012.
102. Galadari, S, Rahman, A, Pallichankandy, S, Galadari, A, Thayyullathil, F: Role of ceramide in diabetes mellitus: evidence and mechanisms. *Lipids Health Dis*, 12: 98, 2013.
103. Russo, SB, Ross, JS, Cowart, LA: Sphingolipids in obesity, type 2 diabetes, and metabolic disease. *Handb Exp Pharmacol*: 373-401, 2013.
104. Ramanadham, S, Hsu, F-F, Zhang, S, Bohrer, A, Ma, Z, Turk, J: Electrospray ionization mass spectrometric analyses of phospholipids from INS-1 insulinoma cells: comparison to pancreatic islets and effects of fatty acid supplementation on phospholipid composition and insulin secretion. *Biochimica et Biophysica Acta (BBA) - Molecular and Cell Biology of Lipids*, 1484: 251-266, 2000.

105. Hsu, FF, Bohrer, A, Wohltmann, M, Ramanadham, S, Ma, ZM, Yarasheski, K, Turk, J: Electrospray ionization mass spectrometric analyses of changes in tissue phospholipid molecular species during the evolution of hyperlipidemia and hyperglycemia in Zucker diabetic fatty rats. *Lipids*, 35: 839-854, 2000.
106. Zhao, HJ, Wang, S, Cheng, H, Zhang, MZ, Takahashi, T, Fogo, AB, Breyer, MD, Harris, RC: Endothelial nitric oxide synthase deficiency produces accelerated nephropathy in diabetic mice. *J Am Soc Nephrol*, 17: 2664-2669, 2006.
107. Voziyan, P, Brown, KL, Chetyrkin, S, Hudson, B: Site-specific AGE modifications in the extracellular matrix: a role for glyoxal in protein damage in diabetes. *Clin Chem Lab Med*, 52: 39-45, 2014.
108. Voziyan, PA, Khalifah, RG, Thibaudeau, C, Yildiz, A, Jacob, J, Serianni, AS, Hudson, BG: Modification of proteins in vitro by physiological levels of glucose: pyridoxamine inhibits conversion of Amadori intermediate to advanced glycation end-products through binding of redox metal ions. *J Biol Chem*, 278: 46616-46624, 2003.
109. Voziyan, PA, Metz, TO, Baynes, JW, Hudson, BG: A post-Amadori inhibitor pyridoxamine also inhibits chemical modification of proteins by scavenging carbonyl intermediates of carbohydrate and lipid degradation. *J Biol Chem*, 277: 3397-3403, 2002.
110. Voziyan, PA, Hudson, BG: Pyridoxamine as a multifunctional pharmaceutical: targeting pathogenic glycation and oxidative damage. *Cellular and Molecular Life Sciences*, 62: 1671-1681, 2005.
111. van Echten, G, Sandhoff, K: Ganglioside metabolism. Enzymology, Topology, and regulation. *J Biol Chem*, 268: 5341-5344, 1993.
112. Niimura, Y, Ishizuka, I: Isolation and identification of nine sulfated glycosphingolipids containing two unique sulfated gangliosides from the African green monkey kidney cells, Verots S3, and their possible metabolic pathways. *Glycobiology*, 16: 729-735, 2006.
113. Varki, NM, Varki, A: Diversity in cell surface sialic acid presentations: implications for biology and disease. *Lab Invest*, 87: 851-857, 2007.

114. Schauer, R: Sialic acids as regulators of molecular and cellular interactions. *Curr Opin Struct Biol*, 19: 507-514, 2009.
115. Malykh, YN, Schauer, R, Shaw, L: N-Glycolylneuraminic acid in human tumours. *Biochimie*, 83: 623-634, 2001.
116. Honke, K, Zhang, Y, Cheng, X, Kotani, N, Taniguchi, N: Biological roles of sulfoglycolipids and pathophysiology of their deficiency. *Glycoconj J*, 21: 59-62, 2004.
117. Niimura, Y, Moue, T, Takahashi, N, Nagai, K: Medium osmolarity-dependent biosynthesis of renal cellular sulfoglycolipids is mediated by the MAPK signaling pathway. *Biochim Biophys Acta*, 1801: 1155-1162, 2010.
118. Stettner, P, Bourgeois, S, Marsching, C, Traykova-Brauch, M, Porubsky, S, Nordstrom, V, Hopf, C, Kusters, R, Sandhoff, R, Wiegandt, H, Wagner, CA, Grone, HJ, Jennemann, R: Sulfatides are required for renal adaptation to chronic metabolic acidosis. *Proc Natl Acad Sci U S A*, 110: 9998-10003, 2013.
119. Rancoule, C, Pradere, JP, Gonzalez, J, Klein, J, Valet, P, Bascands, JL, Schanstra, JP, Saulnier-Blache, JS: Lysophosphatidic acid-1-receptor targeting agents for fibrosis. *Expert Opin Investig Drugs*, 20: 657-667, 2011.
120. Grzelczyk, A, Gendaszewska-Darmach, E: Novel bioactive glycerol-based lysophospholipids: new data -- new insight into their function. *Biochimie*, 95: 667-679, 2013.
121. Shoji, N, Nakagawa, K, Asai, A, Fujita, I, Hashiura, A, Nakajima, Y, Oikawa, S, Miyazawa, T: LC-MS/MS analysis of carboxymethylated and carboxyethylated phosphatidylethanolamines in human erythrocytes and blood plasma. *J Lipid Res*, 51: 2445-2453, 2010.
122. Sookwong, P, Nakagawa, K, Fujita, I, Shoji, N, Miyazawa, T: Amadori-glycated phosphatidylethanolamine, a potential marker for hyperglycemia, in streptozotocin-induced diabetic rats. *Lipids*, 46: 943-952, 2011.
123. Ravandi, A, Kuksis, A, Shaikh, NA: Glucosylated glycerophosphoethanolamines are the major LDL glycation products and increase LDL susceptibility to oxidation: evidence of their presence in atherosclerotic lesions. *Arterioscler Thromb Vasc Biol*, 20: 467-477, 2000.

124. Gorgas, K, Teigler, A, Komljenovic, D, Just, WW: The ether lipid-deficient mouse: tracking down plasmalogen functions. *Biochim Biophys Acta*, 1763: 1511-1526, 2006.
125. Zhang, M-Z, Wang, S, Yang, S, Yang, H, Fan, X, Takahashi, T, Harris, RC: Role of blood pressure and the renin-angiotensin system in development of diabetic nephropathy (DN) in eNOS^{-/-} db/db mice. *American Journal of Physiology - Renal Physiology*, 302: F433-F438, 2012.
126. Sugimoto, H, Grahovac, G, Zeisberg, M, Kalluri, R: Renal fibrosis and glomerulosclerosis in a new mouse model of diabetic nephropathy and its regression by bone morphogenic protein-7 and advanced glycation end product inhibitors. *Diabetes*, 56: 1825-1833, 2007.
127. Lewis, EJ, Greene, T, Spitalerwiz, S, Blumenthal, S, Berl, T, Hunsicker, LG, Pohl, MA, Rohde, RD, Raz, I, Yerushalmy, Y, Yagil, Y, Herskovits, T, Atkins, RC, Reutens, AT, Packham, DK, Lewis, JB: Pyridorin in type 2 diabetic nephropathy. *J Am Soc Nephrol*, 23: 131-136, 2012.
128. Masson, E, Troncy, L, Ruggiero, D, Wiernsperger, N, Lagarde, M, El Bawab, S: a-Series gangliosides mediate the effects of advanced glycation end products on pericyte and mesangial cell proliferation: a common mediator for retinal and renal microangiopathy? *Diabetes*, 54: 220-227, 2005.
129. Zador, IZ, Deshmukh, GD, Kunkel, R, Johnson, K, Radin, NS, Shayman, JA: A role for glycosphingolipid accumulation in the renal hypertrophy of streptozotocin-induced diabetes mellitus. *J Clin Invest*, 91: 797-803, 1993.
130. Liu, G, Han, F, Yang, Y, Xie, Y, Jiang, H, Mao, Y, Wang, H, Wang, M, Chen, R, Yang, J, Chen, J: Evaluation of sphingolipid metabolism in renal cortex of rats with streptozotocin-induced diabetes and the effects of rapamycin. *Nephrol Dial Transplant*, 26: 1493-1502, 2011.
131. Mwangi, DW, Bansal, DD: Evidence of free radical participation in N-glycolylneuraminic acid generation in liver of chicken treated with gallic acid. *Indian J Biochem Biophys*, 41: 20-28, 2004.
132. Tan, Y, Lim, YB, Altieri, KE, Seitzinger, SP, Turpin, BJ: Mechanisms leading to oligomers and SOA through aqueous photooxidation: insights from OH radical oxidation of acetic acid and methylglyoxal. *Atmos Chem Phys*, 12: 801-813, 2012.

133. Padler-Karavani, V, Yu, H, Cao, H, Chokhawala, H, Karp, F, Varki, N, Chen, X, Varki, A: Diversity in specificity, abundance, and composition of anti-Neu5Gc antibodies in normal humans: potential implications for disease. *Glycobiology*, 18: 818-830, 2008.
134. Nagai, K, Tadano-Aritomi, K, Niimura, Y, Ishizuka, I: Effect of nutritional substrate on sulfolipids metabolic turnover in isolated renal tubules from rat. *Proc Jpn Acad Ser B Phys Biol Sci*, 84: 24-29, 2008.
135. Ogawa, D, Shikata, K, Honke, K, Sato, S, Matsuda, M, Nagase, R, Tone, A, Okada, S, Usui, H, Wada, J, Miyasaka, M, Kawashima, H, Suzuki, Y, Suzuki, T, Taniguchi, N, Hirahara, Y, Tadano-Aritomi, K, Ishizuka, I, Tedder, TF, Makino, H: Cerebroside sulfotransferase deficiency ameliorates L-selectin-dependent monocyte infiltration in the kidney after ureteral obstruction. *J Biol Chem*, 279: 2085-2090, 2004.
136. Lundbaek, JA, Andersen, OS: Lysophospholipids modulate channel function by altering the mechanical properties of lipid bilayers. *J Gen Physiol*, 104: 645-673, 1994.
137. Ben-Zeev, G, Telias, M, Nussinovitch, I: Lysophospholipids modulate voltage-gated calcium channel currents in pituitary cells; effects of lipid stress. *Cell Calcium*, 47: 514-524, 2010.
138. Pradere, JP, Gonzalez, J, Klein, J, Valet, P, Gres, S, Salant, D, Bascands, JL, Saulnier-Blache, JS, Schanstra, JP: Lysophosphatidic acid and renal fibrosis. *Biochim Biophys Acta*, 1781: 582-587, 2008.
139. Rai, V, Toure, F, Chitayat, S, Pei, R, Song, F, Li, Q, Zhang, J, Rosario, R, Ramasamy, R, Chazin, WJ, Schmidt, AM: Lysophosphatidic acid targets vascular and oncogenic pathways via RAGE signaling. *J Exp Med*, 209: 2339-2350, 2012.
140. Tanji, N, Markowitz, GS, Fu, C, Kislinger, T, Taguchi, A, Pischetsrieder, M, Stern, D, Schmidt, AM, D'Agati, VD: Expression of advanced glycation end products and their cellular receptor RAGE in diabetic nephropathy and nondiabetic renal disease. *J Am Soc Nephrol*, 11: 1656-1666, 2000.
141. Sasagawa, T, Suzuki, K, Shiota, T, Kondo, T, Okita, M: The significance of plasma lysophospholipids in patients with renal failure on hemodialysis. *J Nutr Sci Vitaminol (Tokyo)*, 44: 809-818, 1998.

142. Pang, LQ, Liang, QL, Wang, YM, Ping, L, Luo, GA: Simultaneous determination and quantification of seven major phospholipid classes in human blood using normal-phase liquid chromatography coupled with electrospray mass spectrometry and the application in diabetes nephropathy. *J Chromatogr B Analyt Technol Biomed Life Sci*, 869: 118-125, 2008.
143. Bassa, BV, Noh, JW, Ganji, SH, Shin, MK, Roh, DD, Kamanna, VS: Lysophosphatidylcholine stimulates EGF receptor activation and mesangial cell proliferation: regulatory role of Src and PKC. *Biochim Biophys Acta*, 1771: 1364-1371, 2007.
144. Zhu, K, Baudhuin, LM, Hong, G, Williams, FS, Cristina, KL, Kabarowski, JH, Witte, ON, Xu, Y: Sphingosylphosphorylcholine and lysophosphatidylcholine are ligands for the G protein-coupled receptor GPR4. *J Biol Chem*, 276: 41325-41335, 2001.
145. Kabarowski, JH, Zhu, K, Le, LQ, Witte, ON, Xu, Y: Lysophosphatidylcholine as a ligand for the immunoregulatory receptor G2A. *Science*, 293: 702-705, 2001.
146. Levi, V, Villamil Giraldo, AM, Castello, PR, Rossi, JP, Gonzalez Flecha, FL: Effects of phosphatidylethanolamine glycation on lipid-protein interactions and membrane protein thermal stability. *Biochem J*, 416: 145-152, 2008.
147. Veiga da-Cunha, M, Jacquemin, P, Delpierre, G, Godfraind, C, Theate, I, Vertommen, D, Clotman, F, Lemaigre, F, Devuyst, O, Van Schaftingen, E: Increased protein glycation in fructosamine 3-kinase-deficient mice. *Biochem J*, 399: 257-264, 2006.
148. Chetyrkin, SV, Kim, D, Belmont, JM, Scheinman, JI, Hudson, BG, Voziyan, PA: Pyridoxamine lowers kidney crystals in experimental hyperoxaluria: A potential therapy for primary hyperoxaluria. *Kidney Int*, 67: 53-60, 2005.
149. Kanetsuna, Y, Takahashi, K, Nagata, M, Gannon, MA, Breyer, MD, Harris, RC, Takahashi, T: Deficiency of endothelial nitric-oxide synthase confers susceptibility to diabetic nephropathy in nephropathy-resistant inbred mice. *Am J Pathol*, 170: 1473-1484, 2007.
150. Grove, KJ, Voziyan, PA, Spraggins, JM, Wang, S, Pauksakon, P, Harris, RC, Hudson, BG, Caprioli, RM: Diabetic nephropathy induces alterations in the glomerular and tubule lipid profiles. *Journal of Lipid Research*, 55: 1375-1385, 2014.

151. Sharma, K, Lee, S, Han, S, Lee, S, Francos, B, McCue, P, Wassell, R, Shaw, MA, RamachandraRao, SP: Two-dimensional fluorescence difference gel electrophoresis analysis of the urine proteome in human diabetic nephropathy. *PROTEOMICS*, 5: 2648-2655, 2005.
152. Rao, PV, Lu, X, Standley, M, Pattee, P, Neelima, G, Girisesh, G, Dakshinamurthy, KV, Roberts, CT, Nagalla, SR: Proteomic Identification of Urinary Biomarkers of Diabetic Nephropathy. *Diabetes Care*, 30: 629-637, 2007.
153. Overgaard, A, Hansen, H, Lajer, M, Pedersen, L, Tarnow, L, Rossing, P, McGuire, J, Pociot, F: Plasma proteome analysis of patients with type 1 diabetes with diabetic nephropathy. *Proteome Science*, 8: 4, 2010.
154. Kim, H-J, Cho, E-H, Yoo, J-H, Kim, P-K, Shin, J-S, Kim, M-R, Kim, C-W: Proteome Analysis of Serum from Type 2 Diabetics with Nephropathy. *Journal of Proteome Research*, 6: 735-743, 2007.
155. Yoshida, Y, Miyamoto, M, Taguchi, I, Xu, B, Zhang, Y, Yaoita, E, Fujinaka, H, Yamamoto, T: Human kidney glomerulus proteome and biomarker discovery of kidney diseases. *PROTEOMICS – Clinical Applications*, 2: 420-427, 2008.
156. Thongboonkerd, V, Barati, MT, McLeish, KR, Benarafa, C, Remold-O'Donnell, E, Zheng, S, Rovin, BH, Pierce, WM, Epstein, PN, Klein, JB: Alterations in the Renal Elastin-Elastase System in Type 1 Diabetic Nephropathy Identified by Proteomic Analysis. *J Am Soc Nephrol*, 15: 650-662, 2004.
157. Liu, H, Sadygov, RG, Yates, JR: A Model for Random Sampling and Estimation of Relative Protein Abundance in Shotgun Proteomics. *Analytical Chemistry*, 76: 4193-4201, 2004.
158. Zhu, W, Smith, JW, Huang, C-M: Mass Spectrometry-Based Label-Free Quantitative Proteomics. *Journal of Biomedicine and Biotechnology*, 2010, 2010.
159. Sanai, T, Sobka, T, Johnson, T, El-Essawy, M, Muchaneta-Kubara, EC, Ben Gharbia, O, Oldroyd, S, El Nahas, AM: Expression of cytoskeletal proteins during the course of experimental diabetic nephropathy. *Diabetologia*, 43: 91-100, 2000.
160. Schena, FP, Gesualdo, L: Pathogenetic mechanisms of diabetic nephropathy. *J Am Soc Nephrol*, 16 Suppl 1: S30-33, 2005.

161. Oh, JH, Ha, H, Yu, MR, Lee, HB: Sequential effects of high glucose on mesangial cell transforming growth factor- β 1 and fibronectin synthesis. *Kidney Int*, 54: 1872-1878, 1998.
162. Ayo, SH, Radnik, RA, Glass, WF, 2nd, Garoni, JA, Rampt, ER, Appling, DR, Kreisberg, JI: Increased extracellular matrix synthesis and mRNA in mesangial cells grown in high-glucose medium. *Am J Physiol Renal Physiol*, 260: F185-191, 1991.
163. Lee, HB, Yu, M-R, Yang, Y, Jiang, Z, Ha, H: Reactive Oxygen Species-Regulated Signaling Pathways in Diabetic Nephropathy. *J Am Soc Nephrol*, 14: S241-S245, 2003.
164. Stauber, J, MacAleese, L, Franck, J, Claude, E, Snel, M, Kaletas, BK, Wiel, IMVD, Wisztorski, M, Fournier, I, Heeren, RMA: On-Tissue Protein Identification and Imaging by MALDI-Ion Mobility Mass Spectrometry. *Journal of the American Society for Mass Spectrometry*, 21: 338-347, 2010.
165. Grüner, BM, Hahne, H, Mazur, PK, Trajkovic-Arsic, M, Maier, S, Esposito, I, Kalideris, E, Michalski, CW, Kleeff, J, Rauser, S, Schmid, RM, Küster, B, Walch, A, Siveke, JT: MALDI Imaging Mass Spectrometry for *In Situ* Proteomic Analysis of Preneoplastic Lesions in Pancreatic Cancer. *PLoS ONE*, 7: e39424, 2012.
166. Ye, H, Mandal, R, Catherman, A, Thomas, PM, Kelleher, NL, Ikonomidou, C, Li, L: Top-Down Proteomics with Mass Spectrometry Imaging: A Pilot Study towards Discovery of Biomarkers for Neurodevelopmental Disorders. *PLoS ONE*, 9: e92831, 2014.
167. Janciauskiene, S: Conformational properties of serine proteinase inhibitors (serpins) confer multiple pathophysiological roles. *Biochimica et Biophysica Acta (BBA) - Molecular Basis of Disease*, 1535: 221-235, 2001.
168. Whisstock, JC, Skinner, R, Carrell, RW, Lesk, AM: Conformational changes in serpins: I. the native and cleaved conformations of α 1-antitrypsin. *Journal of Molecular Biology*, 295: 651-665, 2000.
169. Kwak, N-J, Wang, E-H, Heo, I-Y, Jin, D-C, Cha, J-H, Lee, K-H, Yang, C-W, Kang, C-S, Choi, Y-J: Proteomic analysis of alpha-1-antitrypsin in immunoglobulin A nephropathy. *PROTEOMICS – Clinical Applications*, 1: 420-428, 2007.

170. Navarro-Muñoz, M, Ibernón, M, Bonet, J, Pérez, V, Pastor, MC, Bayés, B, Casado-Vela, J, Navarro, M, Ara, J, Espinal, A, Fluvià, L, Serra, A, López, D, Romero, R: Uromodulin and α -1-Antitrypsin Urinary Peptide Analysis to Differentiate Glomerular Kidney Diseases. *Kidney and Blood Pressure Research*, 35: 314-325, 2012.
171. Buhimschi, IA, Zhao, G, Funai, EF, Harris, N, Sasson, IE, Bernstein, IM, Saade, GR, Buhimschi, CS: Proteomic profiling of urine identifies specific fragments of SERPINA1 and albumin as biomarkers of preeclampsia. *American Journal of Obstetrics and Gynecology*, 199: 551.e551-551.e516, 2008.
172. Aronoff, SL, Schnider, S, Smeltzer, J, Mackay, W, Tchou, P, Rushforth, N, Miller, M, Bennett, PH: Urinary Excretion and Renal Clearance of Specific Plasma Proteins in Diabetes of Short and Long Duration. *Diabetes*, 30: 656-663, 1981.
173. Candiano, G, Musante, L, Bruschi, M, Petretto, A, Santucci, L, Boccio, PD, Pavone, B, Perfumo, F, Urbani, A, Scolari, F, Ghiggeri, GM: Repetitive Fragmentation Products of Albumin and α 1-Antitrypsin in Glomerular Diseases Associated with Nephrotic Syndrome. *J Am Soc Nephrol*, 17: 3139-3148, 2006.
174. Speeckaert, MM, Speeckaert, R, Van De Voorde, L, Delanghe, JR: Immunochemically unreactive albumin in urine: fiction or reality? *Critical Reviews in Clinical Laboratory Sciences*, 48: 87-96, 2011.
175. Park, CH, Maack, T: Albumin absorption and catabolism by isolated perfused proximal convoluted tubules of the rabbit. *The Journal of Clinical Investigation*, 73: 767-777, 1984.
176. Hellin, JL, Bech-Serra, JJ, Moctezuma, EL, Chocron, S, Santin, S, Madrid, A, Vilalta, R, Canals, F, Torra, R, Meseguer, A, Nieto, JL: Very Low-Molecular-Mass Fragments of Albumin in the Plasma of Patients With Focal Segmental Glomerulosclerosis. *American Journal of Kidney Diseases*, 54: 871-880, 2009.
177. Greive, KA, Balazs, NDH, Comper, WD: Protein Fragments in Urine Have Been Considerably Underestimated by Various Protein Assays. *Clinical Chemistry*, 47: 1717-1719, 2001.
178. Comper, WD, Jerums, G, Osicka, TM: Differences in urinary albumin detected by four immunoassays and high-performance liquid chromatography. *Clinical Biochemistry*, 37: 105-111, 2004.

179. Kania, K, Byrnes, EA, Beilby, JP, Webb, SAR, Strong, KJ: Urinary proteases degrade albumin: implications for measurement of albuminuria in stored samples. *Annals of Clinical Biochemistry*, 47: 151-157, 2010.
180. Clavant, SP, Greive, KA, Nikolovski, J, Reeve, S, Smith, AI, Comper, WD: Albumin fragments in normal rat urine are derived from rapidly degraded filtered albumin. *Nephrology*, 8: 72-79, 2003.
181. Osicka, TM, Houlihan, CA, Chan, JG, Jerums, G, Comper, WD: Albuminuria in patients with type 1 diabetes is directly linked to changes in the lysosome-mediated degradation of albumin during renal passage. *Diabetes*, 49: 1579-1584, 2000.
182. Gudehithlu, KP, Pegoraro, AA, Dunea, G, Arruda, JAL, Singh, AK: Degradation of albumin by the renal proximal tubule cells and the subsequent fate of its fragments. *Kidney Int*, 65: 2113-2122, 2004.
183. Zeng, F, Miyazawa, T, Kloepfer, LA, Harris, RC: Deletion of ErbB4 accelerates polycystic kidney disease progression in cpk mice. *Kidney Int*, 2014.

CURRICULUM VITAE

Kerri Grove, Ph.D.

465 21st Avenue South • Nashville, TN 37215
(763) 218-9622
kerri.j.grove@vanderbilt.edu

EDUCATION

Ph.D. in Chemistry Nashville, TN
Vanderbilt University August 2014

Dissertation: “Imaging Mass Spectrometry for the Elucidation of Lipid and Protein Changes in Diabetic Nephropathy and Assessment of Drug Efficacy”

Advisor: Dr. Richard Caprioli

B.S. in Chemistry St. Paul, MN
Bethel University May 2007

• Cum Laude Honors, Deans List, Chemistry Department Student Award

B.S. in Biochemistry/Molecular Biology St. Paul, MN
Bethel University May 2007

RESEARCH EXPERIENCE

Graduate Research 2009-2014

- Developed techniques for high spatial resolution imaging mass spectrometry of tissues with a focus on the kidney microstructures of glomeruli and tubules
- Discovered unique lipid and protein classifiers in microstructures of the kidney that correlated with progression of renal disease by an *in situ* approach utilizing TOF and FTICR MS
- Elucidated disease related molecular modifications on biomolecules in affected organs that have potential to serve as early markers of disease
- Evaluated an investigational drug therapy to identify novel metabolomics markers and confirm efficacious molecular response to treatment

PROFESSIONAL SOCIETY MEMBERSHIP

- American Society of Mass Spectrometry, 2009-present

AWARDS AND FELLOWSHIPS

- Vanderbilt Institute of Chemical Biology Student Symposium Oral Presentation Award, 2013
- Hercules Fellowship, Vanderbilt University, 2008-2009

TEACHING EXPERIENCE

Workshop Leader, AIMS.2012 and AIMS.2013 (Advanced Imaging Mass Spectrometry Laboratory Course)

Vanderbilt University, Nashville, TN; March 26-29, 2012 and April 16-19, 2013

- Led hands-on workshop portions of an imaging mass spectrometry short course including tissue cryo-sectioning, MALDI sample preparation, and imaging data analysis

Volunteer, Aspirnaut™ Educational Program

Vanderbilt University, Nashville, TN; 2012-2013

- Taught science lessons to rural elementary and middle school students through videoconferencing

Teaching Assistant, General Chemistry

Vanderbilt University, Nashville, TN; 2008-2009

- Assisted in preparation and execution of laboratory section

SCIENTIFIC PRESENTATIONS

• **Kerri J. Grove**, “High Spatial Resolution Molecular Imaging for Efficacy of Drug Treatment in Diabetic Nephropathy” Vanderbilt Institute of Chemical Biology Student Symposium, August, 2013, (*Oral Presentation*)

• **Kerri J. Grove**, “Special Topics: Diabetic Nephropathy” Advanced Imaging Mass Spectrometry Course, Vanderbilt, April 2013, (*Oral presentation*)

• **Kerri J. Grove**, Raf Van de Plas, Jeffery M. Spraggins, Paul A. Voziyan, Raymond C. Harris, Billy G. Hudson, Richard M. Caprioli, “Discovery and Localization of Modified Lipids in Kidneys of Diabetic Mouse Model using Mass Difference Scanning and Imaging Mass Spectrometry” 61st ASMS Conference on Mass Spectrometry and Allied Topics, June 2013, (*Poster presentation*)

- **Kerri J. Grove**, Paul A. Voziyan, Jeffery M. Spraggins, Roberto M. Vanacore, Raymond C. Harris, Billy G. Hudson, Richard M. Caprioli, “Glomerular Alterations Induced by Diabetic Nephropathy Revealed Using High Spatial Resolution MALDI Imaging Mass Spectrometry” 60th ASMS Conference on Mass Spectrometry and Allied Topics, May 2012, (*Poster presentation*)
- **Kerri J. Grove**, Paul A. Voziyan, Roberto M. Vanacore, Billy G. Hudson, Richard M. Caprioli, “Analysis of Glomerular Proteins by High Spatial Resolution MALDI Imaging Mass Spectrometry” 59th ASMS Conference on Mass Spectrometry and Allied Topics, June 2011, (*Poster presentation*)
- **Kerri J. Grove**, Paul A. Voziyan, Roberto M. Vanacore, Raymond C. Harris, Billy G. Hudson, Richard M. Caprioli, “Analysis of Glomerular Proteins by High Spatial Resolution MALDI Imaging Mass Spectrometry” Gordon Research Conference, Collagen, July 2011, (*Poster presentation*)
- **Kerri J. Grove**, Richard M. Caprioli, “Matrix Pre-Coated Targets for MALDI Imaging Mass Spectrometry” 58th ASMS Conference on Mass Spectrometry and Allied Topics, May 2010, (*Poster presentation*)

PUBLICATIONS

- **Grove, K**, Voziyan, P, Spraggins, J, Wang, S, Pauksakon, P, Harris, R, Hudson, B, Caprioli, R. Diabetic nephropathy induces alterations in the glomerular and tubule lipid profiles. *Journal of Lipid Research*, 55: 1375-1385, 2014.
- **Grove, K**, Frappier, S, Caprioli, R: Matrix Pre-Coated MALDI MS Targets for Small Molecule Imaging in Tissues. *Journal of the American Society for Mass Spectrometry*, 22: 192-195, 2011.
- **Grove, K**, King, RA, Burger, U: Photo-rearrangement of N-substituted pyridinium and meta-alkoxy pyridinium ions. *Journal of Molecular Structure: THEOCHEM*, 807: 25-32, 2007.